Sliding Mode Control of Switched Reluctance Motors

by

Atsuhiko Sakurai

A thesis submitted in conformity with the requirements
for the degree of Master of Applied Science
Graduate Department of Electrical and Computer Engineering
University of Toronto

Abstract

Sliding Mode Control of Switched Reluctance Motors

Atsuhiko Sakurai

Master of Applied Science

Graduate Department of Electrical and Computer Engineering

University of Toronto

2001

The objective of this thesis is to design a simple nonlinear controller for stabilization of switched reluctance (SR) machines. The nonlinearities in the torque production of SR machines and the complicated model for the magnetization characteristics are the major problems in designing a simple controller that guarantees stability and robustness of SR machines. In this thesis, the nonlinear sliding mode control design method is employed to guarantee the stability of speed tracking control in SR machines. In addition, a control design method that utilizes minimal information on magnetization characteristics is developed. The resulting controller requires simple computations which are beneficial in practical implementations.

Acknowledgements

I wish to express my deepest gratitude to my supervisors Professor Bruce A. Francis and Professor Manfredi Maggiore for their guidance and helpful advice throughout the course of study. Their patient support and encouragement are gratefully appreciated.

I wish to thank my friends, specially Hideaki Ishii for his kind advice and encouragement, Luis Zubieta and Charles Lidstone for their helpful discussions, Suneil Sastri and Ewen MacDonald for their company and support.

Financial support in the form of Research Assistantships from Professor Francis and the University of Toronto is gratefully acknowledged.

Finally, this thesis is dedicated to my family, whose emotional and financial support have allowed me to come this far.

Contents

List of Figures

List of Tables

Chapter 1

Introduction

Switched Reluctance (SR) machines are relatively new additions to a group of well-established variable-speed electrical machines. The major difference that distinguishes them from other conventional drives is simple, low cost, and rugged constructions. The simplicity of the mechanism is the result of their torque production principle, so called *variable reluctance principle* (see, e.g., [22] and Chapter 2). SR machines produce torque without any permanent magnets and with no concentrated windings on their shaft. This unique torque production principle allows SR machines to have the benefits of reliability and capability of four-quadrant[1] operation in a wide speed range. Other advantages of SR machines are also known to be the high torque-to-inertia ratios and high torque-to-power ratios (see, e.g., [9]). These attractive features have led SR machines to be potential candidates for applications in industrial and commercial markets (see, e.g., [5, 20, 22]).

Despite the simple mechanism and attractive capabilities, SR machines have some limitations. Unlike other conventional electrical machines, they cannot operate directly from main AC or DC supply and require current-pulse signals for proper torque production. Hence, they require an electronic controller that regulates commutation[2] of coil excitations and the waveform of current signals. Another drawback of SR machines is that their dynamics are inherently nonlinear due to their magnetic char-

[1] Four-quadrant drive operates in forward and backward as a motor and a generator.

[2] Commutation is a process of turning on and off the excitation of concentrated windings.

acteristics depending on both the shaft angle and current magnitudes, and thus, in order to design controllers with desired stability properties, one has to resort to somewhat complicated nonlinear control tools. Furthermore, the nonlinearities cannot be neglected because in practice the machines are operated at high current levels (where saturation of core material occurs), so as to maximize their torque density[3].

Besides guaranteed stability, it is desirable for SR machine controllers to have features such as parameter insensitivity, quick precise dynamic responses, and rapid recovery from load disturbances. Traditionally, SR machines are controlled by the combination of a conventional PI controller and switching controllers. Although the traditional control scheme may work well in some situations, its design is based on heuristic rules that cannot guarantee a satisfactory performance under all conditions. This claim is substantiated by the observation, found, e.g., in [9, 15, 17], that the traditional control scheme is sensitive to variations in plant parameters and operating conditions. Hence, there have been demands for rigorous nonlinear control design methods for SR machines to meet the performance criteria.

1.1 Stabilization of Switched Reluctance Machines

The attractive characteristics of SR machines and the challenges involved in overcoming their limitations have motivated a large amount of research on SR machines in the past decade (see, e.g., [9]). In the following, we first introduce some of the relevant research areas found in the literature that we do not cover in this thesis. Then, the research results that have motivated this thesis are presented. Finally, the focus of this thesis is described.

1.1.1 Relevant Research

As explained earlier, SR machines operate in saturation to maximize their torque density, and thus the effect of the magnetization nonlinearities must be explicitly taken into account in the control design. This has motivated research in modeling the

[3]Torque density is the ratio of torque per unit volume.

magnetization characteristics. Several different models and methods for measuring inductance and flux-linkage in SR machines have been introduced (see, e.g., [4,17,23, 30,33,34]).

The commutation of SR machines is essential for their proper operation. Moreover, in a high speed operation, it is important to know the optimal turn-on and turn-off angles[4] to achieve the maximum performance in efficiency or output torque. This has motivated investigation in optimal commutation of SR machines (see, e.g., [1,13,14, 31]). In [1], a discrete set of commutation angles for different operating conditions has been reported. Optimal commutation strategies for average torque control have been introduced (see, e.g., [13,14]). Self-tuning control has been used in a commutation strategy to maximize the efficiency of SR machines (see, e.g., [31]).

Operating in saturation allows SR machines to achieve the maximum torque density, but it causes ripple in the waveform of output torque. This has been one of the drawbacks for applications such as high performance servo applications. Several researchers have developed torque-ripple minimization strategies (see, e.g., [16,28,29]). In [16], PWM current control has been studied for reducing torque-ripple. A simplified control method over a wide speed range has been developed (see, e.g., [28]). In [29], self-tuning control has been employed to minimize torque-ripple in the presence of parameter uncertainties.

1.1.2 Focus of the Research

As pointed out earlier, one of the major challenges in control of SR machines is designing stable controllers taking into account the system nonlinearities. The design of stabilizing and robust nonlinear controllers is one of the important problems on which researchers have focused. One of the earlier attempts was made by the use of nonlinear feedback linearizing control (see, e.g., [17,25,27,36]). Ilic'-Spong *et al.* [17] introduced for the the first time the application of feedback linearization to electric drives. They developed a nonlinear mathematical model based on experimentally measured data. A state feedback control algorithm was designed to compensate nonlinearities in the

[4]Turn-on and turn-off angles are the shaft angles at which commutation occurs.

system and to decouple the effect of current in torque production. Simulation results reported in [17,27] show robustness of the controller. References [25,36] report control algorithms similar to [17]. Specifically, in [36], simulation results using feedback linearizing control are compared against the traditional control scheme. The comparison shows that the feedback linearizing controller has a superior performance. It must be said, however, that the traditional controller does not seem to be tuned optimally at the operating condition. One of the drawbacks of feedback linearizing control is the high computational requirement. Another disadvantage of this control method is that it requires full knowledge of the magnetization characteristics.

Another advanced nonlinear control scheme developed in the recent years is nonlinear sliding mode control (see, e.g., [2, 18, 21, 35]). Sliding mode control has been applied to electrical machines because its switching control structure is suitable for electronic power circuits. Reference [2] applied sliding mode control to SR machines for the first time. Although the control design procedure does not follow the standard approach, the resulting controller in simulation shows that the controller is robust to parameter variations and load disturbances. The designed controller, however, does not take saturation into account. The same authors reported analytical study on operation in the saturated region (see [3]), but it appears that they have not yet attempted to design a sliding mode controller taking saturation into account. Reference [18] reported a similar control scheme to [2] with some improvements in the feedback loop, but it lacks in a theoretical analysis. Filicori *et al.* [10] have developed a unique way of formulating the torque equation which allows flux-linkage as a state variable and takes saturation into account. They designed a prototype controller using sliding mode control for a special type of SR machine, called variable reluctance motor for the purpose of direct drive motor (see [21]). Simulation results show robustness and fast dynamic response of the controller. In [35], a sliding mode controller for saturated SR machines have been designed, and its performance was compared to the traditional control scheme. Simulation results show superior performance of the sliding mode controller, but the controller requires extensive calculations due to the complicated magnetization model.

Although the advanced nonlinear control strategies provide better performance

compared to the traditional controller, the authors in [15] point out that such controllers are complicated and require an accurate dynamic model of the machine. A relatively simple and easily implementable control method is needed by industrial design engineers.

From the literature introduced above, we conclude that there is a need for simple nonlinear controllers that require minimum knowledge of magnetization characteristics and minimum amount of computations and yet guarantee the stability and robustness of SR machines. This thesis studies a sliding mode control design method which differs from previous works in that it focuses on theoretical design steps to guarantee the stability of SR machine with less knowledge of saturation characteristics and a small amount of computations. The objectives of this thesis are as follows:

1. To design a sliding mode controller rigorously by theoretical design steps
2. To use minimum information of system model and still guarantee the stability
3. To employ simple calculations for easy implementation

1.2 Organization of the Thesis

In Chapter 2, we first introduce the mechanical structure and electrical circuit of a typical SR machine and describe the basic principle of its operation. The variable reluctance principle is introduced, and various types of SR machines are presented.

Chapter 3 shows the derivation of dynamic models for mechanical and electrical subsystems. The formulation of the torque equation is explained at length, and both unsaturated and saturated cases are shown. A magnetization characteristic model is taken from [4] for simulation studies in the later chapters. We end the chapter with a set of self-contained mathematical state equations for an SR machine.

In Chapter 4, we describe the traditional control scheme of SR machines for a speed tracking problem. Two operating modes are introduced for low and high speed operations, and commutation strategies are described. At the end, a traditional controller is designed by a purely heuristic approach and tested in simulations for low speed operation. A commutation scheme is taken from [1].

Chapter 5 introduces a theoretical design method for sliding mode control. We design a controller based on the rigorous design steps to guarantee the stability of SR machines. The proof of stability is based on one strong assumption that is made intuitively. The designed controller is successfully tested in simulations and compared to the results from Chapter 4.

The thesis focuses on forward motion for motoring operation as one of the four-quadrants of operation. A similar approach can be extended to backward motion and generating operation.

Chapter 2

Switched Reluctance Machines and their Operation

In this chapter, we first introduce the mechanical structures of typical SR machines. Then, the electromechanical coupling in an SR machine, i.e., the principle of torque production, is described. Finally, the basic characteristics of electrical hardware used for SR machines are introduced.

2.1 Mechanical Structure

An SR machine is a brushless drive, that is, it operates without any mechanical commutation components. It has a doubly salient geometry. A cross-section of a typical 8/6 SR machine (having 8 stator poles and 6 rotor poles) is shown in Figure 2.1. A stator is a stationary component that has excitation windings around its poles. The windings are connected in diametrically opposite pairs in either series or parallel, inducing additive magnetic flux in order to form phases. The windings for each phase are independently connected to a remote switching circuit for its commutation.

The other salient component, called a rotor, rotates about the axis of the motor. It can be external but is usually situated inside the stator. The stator and rotor are assembled from steel laminations of the same grade and thickness and do not contain any permanent magnets. Unlike induction machines, there are no concentrated

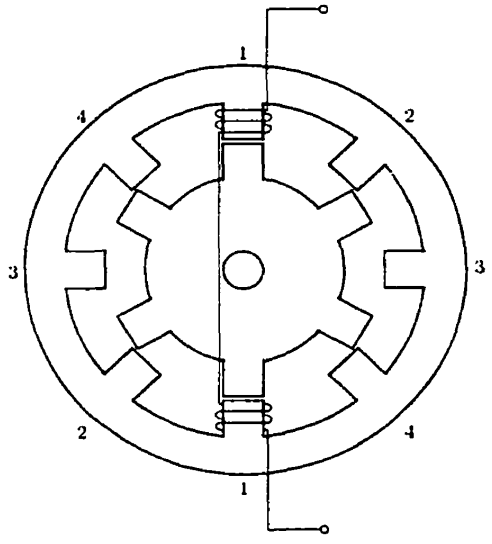

Figure 2.1: 8/6 SR machine cross-section (Windings for only one phase are shown.)

windings on the rotor of an SR machine because its torque production is based on a variable reluctance principle, which is illustrated in the next section.

There is a variety of motor configurations with different shapes of stator and rotor, as well as different numbers of poles and phases. Two main classifications of SR machines are regular and irregular machines (see [22]). The cross-sections of regular and irregular SR machines are shown in Figure 2.2. In a regular machine, the stator and rotor poles are symmetrical about the center lines, ℓ_s and ℓ_r, respectively shown in the figure. They are also equally spaced around the stator and rotor, respectively. An irregular machine is one that is not regular. Typically, an irregular machine is designed to accommodate special needs, such as the capability of starting rotation from any initial rotor position. Different pole-arc angles of the stator and rotor poles are chosen to meet desired machine performance. For applications that require high torque in low speed operation, such as robotic arms, a specific type of SR machine called variable reluctance (VR) motor is often employed. A VR motor has multiple teeth on the rotor poles and is capable of producing high torque (see, e.g., [17,22,27]).

The number of phases and the basic stroke angle are also important factors in choosing a suitable machine for each application. They are determined by the number

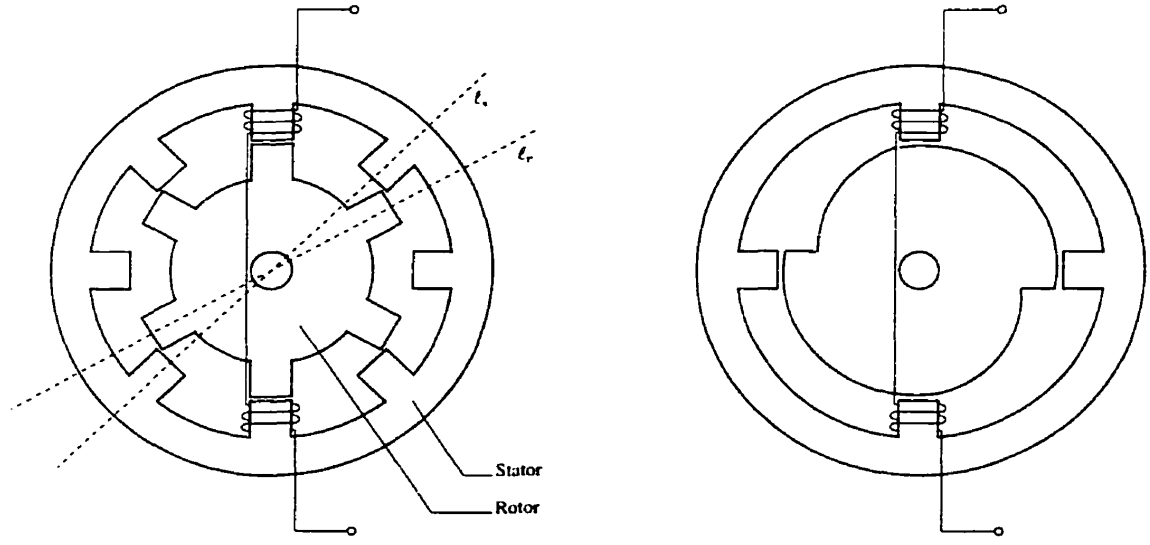

(a) A regular SR machine

(b) An irregular SR machine

Figure 2.2: Cross-sections of regular and irregular machines

of stator and rotor poles. For example, an 8/6 SR machine will have four phases and a basic stroke angle of 15 degrees, whereas a 4/2 machine will have two phases and a basic stroke angle of 90 degrees. In general, the number of phases, m, and the stroke angle, ϵ, can be expressed as a function of the number of stator and rotor poles,

$$m = \frac{N_s}{2}, \qquad \epsilon = \frac{2\pi}{mN_r},$$

where N_s and N_r are the numbers of stator and rotor poles, respectively, and mN_r is the number of strokes per revolution.

The benefit of an SR machine with fewer phases is that it requires simpler commutation control and fewer electrical components. On the other hand, an SR machine with more phases has a smaller stroke angle and, consequently, its torque output is smoother. In general, one-phase machines require assists for initial rotation in motoring operation, and two-phase machines require non-symmetric rotor poles. Machines with three or more phases with symmetric geometry can start motion from any initial rotor position. In many applications, three or four-phase machines are preferred

because of their overall simplicity and cost. In this research, a regular 8/6 four-phase SR machine is studied as a typical example.

2.2 Principle of Torque Production

Like many other electrical machines, an SR machine is an energy converter that takes electrical energy and produces mechanical energy in motoring operation, and vice versa in generating operation. The energy is stored in the magnetic field created by the phase windings and is exchanged between the electrical and the mechanical subsystems. In the following, the process of torque production in an SR machine is described.

When a phase is excited by applying a voltage across its concentrated coil, the current in the coil creates a magnetic flux through its stator poles. The magnetic flux flows through the pair of nearest rotor poles, travels in the rotor and stator steel, and closes a magnetic circuit, as shown in Figure 2.3. In a magnetic circuit, there

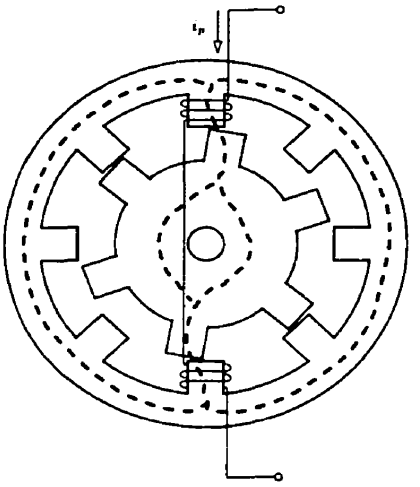

Figure 2.3: Magnetic circuit in an SR machine

exists magnetic reluctance. It is analogous to resistance in an electrical circuit and depends on the magnetic permeability of the material that the flux flows through. In the case of an SR machine, the reluctance in the air gap between the stator and

rotor poles is very large compared to that in steel. Consequently, the total reluctance of the magnetic circuit can be well approximated by the reluctance of the air gap. Because of the doubly salient geometry of an SR machine, the distance between the stator and rotor poles changes as the rotor rotates, and hence the reluctance of a flux path varies as shown in Figure 2.4.

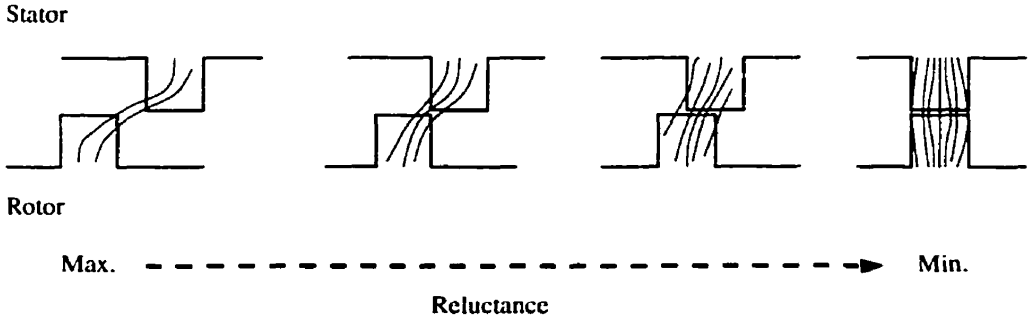

Figure 2.4: Variation of reluctance with respect to rotor position

There are two special rotor positions in SR machine dynamics, the aligned position and the unaligned position, shown in Figure 2.5. When any pair of rotor poles is exactly aligned with the stator poles of a phase, that phase is said to be in the aligned position. A phase is in the unaligned position when the interpolar axis of the rotor (axis ℓ in Figure 2.5) is aligned with the stator poles of the phase. The reluctance of the flux path is at its minimum in the aligned position and is at its maximum in the unaligned position.

The variable reluctance principle is the tendency of the rotor to align itself to the minimum reluctance position. When a phase is excited, the pair of nearest rotor poles (part of the magnetic circuit) are attracted to align themselves to the excited stator poles. Thus, torque is produced. This principle is different from the magnetic interaction occurring in other electrical machines, such as permanent magnet motors and induction motors. The torque production in these other types of motor is based on the attraction between the North and South magnetic poles of permanent or electrically induced magnets. Notice that the rotor poles of an SR machine do not require the existence of magnetic poles to produce torque. Interestingly enough, the radial magnetic attraction that operates an SR machine can become ten times larger

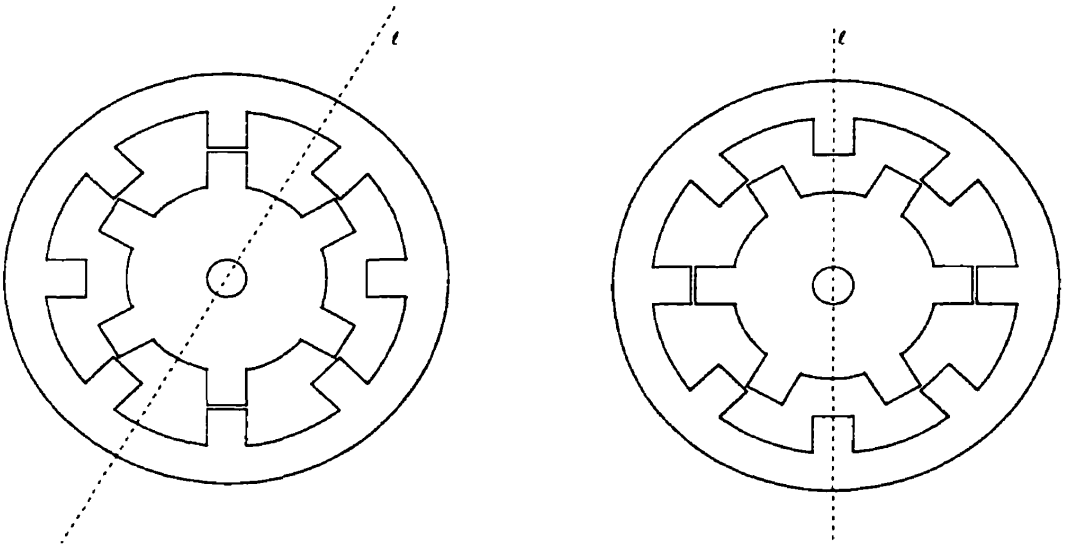

(a) Aligned position (b) Unaligned position

Figure 2.5: Aligned and unaligned positions

than the circumference forces produced by an induction machine (see, e.g., [9]).

In the aligned position shown in Figure 2.5 there is no torque produced, even when the phase is energized, because the reluctance of the flux path is at its minimum. Hence, it is a stable equilibrium position. There is also no torque produced in the unaligned position because the stator pole is exactly in the middle of two adjacent rotor poles. However, as soon as the rotor is displaced to either side of the unaligned position, there appears a torque that displaces it even further and attracts it towards the next aligned position. Hence, the unaligned position is an unstable equilibrium position. Consequently, torque is produced in the direction from any unaligned position to the next aligned position. Since the rotor poles are identical around the rotor, the torque production is periodic. One period from an unaligned position to the next unaligned position is called the *rotor pole-pitch*, τ, in radians and given by

$$\tau = \frac{2\pi}{N_r}.$$

The rotor pole-pitch of an 8/6 SR machine is $\frac{\pi}{3}$ (60°), and the *maximum torque zone*,

where positive torque can be produced in one period, is $\frac{\pi}{6}$ (30°). By successfully exciting the phases in sequence, a continuous torque is produced. Unlike other electrical machines, the direction of rotation in an SR machine does not depend on the direction of magnetic flux and, hence, does not depend on the direction of phase current. This unipolar characteristic of phase current allows simple design of electrical circuits, described in the next section.

2.3 Electrical Hardware

SR machines utilize power converter switching circuits for the commutation of phase excitation. The most common configuration of a switching circuit is shown in Figure 2.6. In general, a switching circuit for an SR machine is simple because of the unipo-

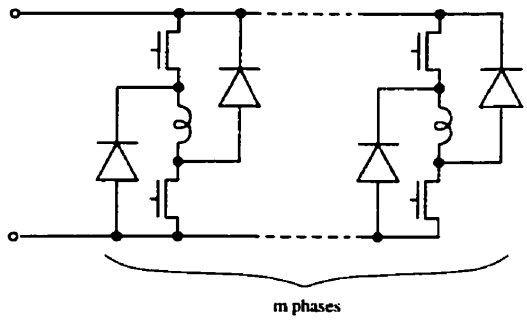

Figure 2.6: Typical configuration of power converter

lar (not alternating) characteristic of its flux-linkage and phase current. Since the direction of rotation does not depend on the signs of flux-linkage and phase current, a switching circuit of an SR machine is designed so that the current in the excitation coil flows only in one direction. In the following, we illustrate the main requirements that a switching circuit for an SR machine must satisfy.

SR machines cannot operate directly from an AC or DC mains voltage supply because inputs to their phase windings must be current pulses. A power converter must supply unipolar current pulses from a DC voltage source, precisely at desired rotor positions. It must also regulate the magnitude and even waveform of the current in order to satisfy the requirements of torque and speed control and ensure safe

operation of the motor and the power transistors. Finally, it must be able to supply pulses of reverse voltage for defluxing, i.e., forcing the phase current to zero in order to avoid reverse torque at certain rotor positions.

The desirable type of power converter has separate switches for each phase so that all phases are virtually independent of each other. The switching circuit considered in this research has the configuration in Figure 2.6. The excitation coil in each phase is connected to one common DC voltage source (or a rectified AC supply) through a transistor switch on each end. The circuit has two freewheeling diodes to provide the unipolar characteristic of phase current. Figure 2.7 shows the current flow in the switching circuit for one phase under different switching conditions. When both

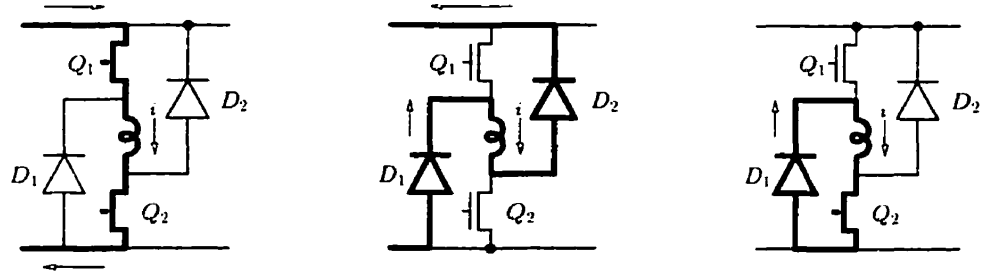

(a) Q_1 & Q_2 on (b) D_1 & D_2 on (c) Q_2 & D_2 on

Figure 2.7: Current dynamics in a switching circuit

switches Q_1 and Q_2 are turned on (Figure 2.7(a)), a constant voltage is applied to the excitation coil, and the current starts to increase. The energy is stored in the magnetic field and converted to mechanical energy. When both switches are turned off (Figure 2.7(b)), the freewheeling diodes D_1 and D_2 allow the existing current in the coil to keep flowing in the same direction. However, the reverse voltage applied to the excitation coil forces the current to decrease. The unused energy in the magnetic field is sent back to the voltage supply as seen in the direction of the current. When only one switch Q_2 is turned on (Figure 2.7(c)), the stored energy is dissipated by the phase resistance and the back emf developed in the coil, and thus, the phase current slowly decreases. If the initial current is zero in Figure 2.7(c), then the current will remain zero because there is no voltage applied across the coil. The switches are turned on and off to control a desired current level for each phase.

Chapter 3

Modeling

In order to analyze the dynamics of an SR machine and to design its controller, a mathematical model of the system must be derived. In this chapter, a mathematical model of the mechanical subsystem is first derived based on physical laws. Next, the torque equation is formulated for one rotor pole-pitch. Finally, the dynamic model for a typical switching circuit is derived. At the end of the chapter, a set of self-contained mathematical equations describing the overall dynamics of an SR machine is presented. General references for this chapter are [6, 22].

3.1 Mechanical Dynamics

A simplified physical model of an SR machine is shown in Figure 3.1. The variables

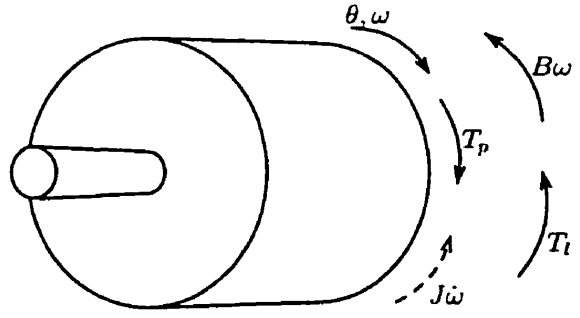

Figure 3.1: Free-body diagram of mechanical subsystem

in this rotational system are

- θ, angular displacement in radians (rad)
- ω, angular velocity in radians per second (rad/s)
- T_p, torque in phase p in Newton-meters (Nm)

all of which are functions of time. Angular displacement is measured from a reference position. Phase torque is the torque produced by one phase, and torque production is identical in all phases. The total instantaneous torque produced by a machine is the sum of the torques produced in each phase, i.e.,

$$T_{total} = \sum_{p=1}^{m} T_p, \tag{3.1}$$

where m is the total number of phases.

Consider the setup in Figure 3.1. The rotating mass of inertia J is subjected to the phase torque T_p and a load torque T_l. Letting B denote the rotational friction coefficient, we have from Newton's second law

$$J\dot{\omega} = -B\omega + \sum_{p=1}^{m} T_p - T_l. \tag{3.2}$$

We thus arrive at the state model

$$\begin{aligned} \dot{\theta} &= \omega \\ \dot{\omega} &= \frac{1}{J}\left(\sum_{p=1}^{m} T_p - B\omega - T_l\right). \end{aligned} \tag{3.3}$$

3.2 Torque Equation

In order to model instantaneous torque produced in one phase, the exchange of energy in the magnetic field must be studied. Magnetic characteristics of an SR machine are determined by its core material, geometry, and excitation coils. We start this section by introducing flux-linkage and phase inductance, which are the major variables in magnetic characteristics considered in modeling a torque equation.

3.2.1 Magnetic Characteristics

The total flux in the stator pole is called flux-linkage, Ψ, which varies with rotor position and phase current; thus we write $\Psi(\theta, i)$. It increases as the rotor pole starts to overlap with the stator pole and approaches the aligned position. Larger magnetic flux-linkage is created as the phase current is increased. At low current levels, flux-linkage is approximately a linear function of phase current. However, beyond a certain level of current, magnetic saturation occurs in the material, thus yielding a nonlinear relationship between flux-linkage and phase current. This critical current level is called the *saturation current.* The characteristic curve of the flux-linkage of one phase with respect to the phase current is called the *magnetization curve.* The magnetization curves for different rotor angles from unaligned to aligned position are shown in Figure 3.2. The curve C_u at the bottom is the flux curve in the

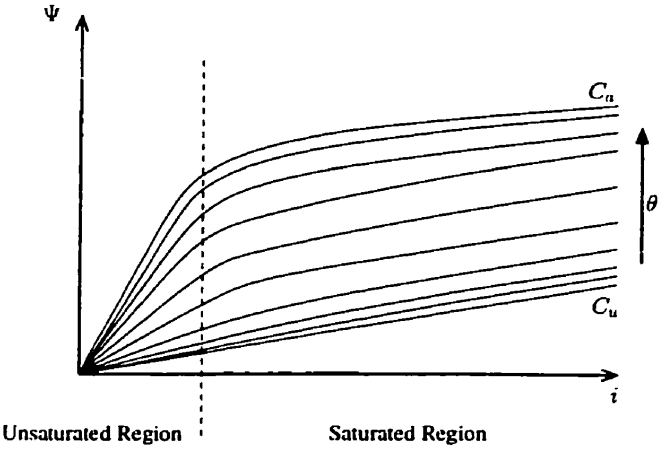

Figure 3.2: Magnetization curve

unaligned position, while C_a at the top is the flux curve in the aligned position. As one can see, the flux path is more susceptible to saturation in the aligned position.

Inductance of an unsaturable inductor is defined as $L = \frac{\Psi}{i}$. Unlike the constant inductance of typical solenoids, phase inductance of an SR machine varies with its rotor position and phase current. Below the saturation current, however, the inductance is a function only of rotor position because the flux-linkage is approximately a

linear function of current, i.e.,

$$\Psi(\theta, i) = L(\theta)i \qquad \text{(unsaturated)}. \tag{3.4}$$

The inductance in the unsaturated region is inversely proportional to the magnetic reluctance, and it achieves a maximum in the aligned position and a minimum in the unaligned position. In the saturated region, because the flux-linkage is a nonlinear function of the phase current, a new expression of inductance, called *incremental inductance*, is given by

$$l(\theta, i) = \frac{\partial \Psi(\theta, i)}{\partial i}. \tag{3.5}$$

In Figure 3.2, one can think of the incremental inductance, $l(\theta, i)$, as the slope of the magnetization curve when θ is held constant. The incremental inductance in the saturated region does not vary as much as the inductance in the unsaturated region when the rotor rotates from the unaligned position to the aligned position under a constant current. Figure 3.3 shows phase inductance in both cases as a function of rotor position.

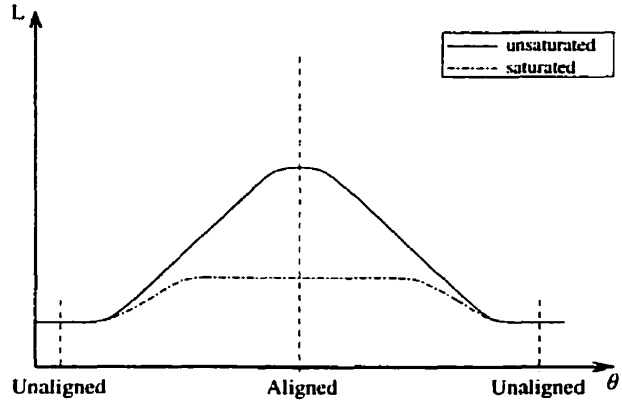

Figure 3.3: Variation of phase inductance with respect to rotor position

It is also important to note that when adjacent phases are excited at the same time, there exists a coupled inductance called mutual-inductance. Hence, in general, phase inductance of an SR machine is the sum of self-inductance and mutual-inductance. However, mutual-inductance is neglected in this research because it is typically very small compared to self-inductance.

3.2.2 Derivation of Torque Equation

The torque produced during motoring operation is the torque required to rotate the rotor. The instantaneous torque can be viewed as the mechanical work done by the motor resulting in a displacement of the rotor angle. The most general expression for torque produced by one phase at any rotor position is given by

$$T(\theta, i) = \frac{\partial W_c(\theta, i)}{\partial \theta}, \tag{3.6}$$

where W_c is referred to as the *coenergy*. In the first approximation, the coenergy can be thought of as the amount of mechanical energy converted from the electrical energy. Assuming that a constant current, i_1, is applied during the rotation from $\theta = 0$ to $\theta = \theta_1$, the coenergy is the area below the magnetization curve, shown in Figure 3.4. The shaded area, W_f, is the energy stored in the magnetic field, and the

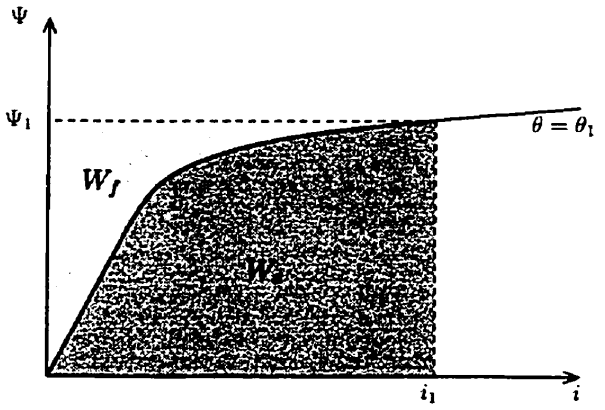

Figure 3.4: Coenergy and stored field energy

rectangular area, $\Psi_1 \times i_1$, is the total input energy. The coenergy can be expressed as the definite integral

$$W_c(\theta_1, i_1) = \int_0^{i_1} \Psi(\theta_1, i) di. \tag{3.7}$$

Since the magnetization curve changes as the rotor rotates, the instantaneous torque can be visualized graphically in Figure 3.5. Here, ΔW_m is the mechanical work done at a constant current as the rotor moves through an infinitesimal displacement,

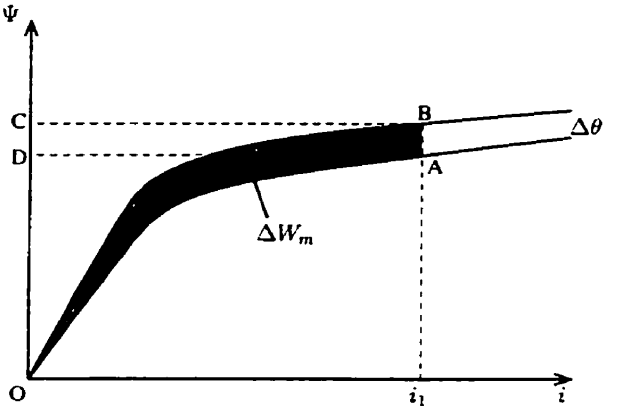

Figure 3.5: Change in coenergy

$\Delta\theta$. Therefore, the instantaneous torque is $\frac{\Delta W_m}{\Delta\theta}$. During such a displacement, there are exchanges of energy among the coenergy, the stored field energy, and the power supply. The constraint of constant current ensures that, during the displacement, the mechanical work done is exactly equal to the change in coenergy, as shown in the following (see [22]).

The energy exchanged with the power supply during the displacement from A to B in Figure 3.5 is given by the change of total input energy corresponding to the displacement $\Delta\theta$, that is,

$$\Delta W_{\text{total}} = ABCD, \tag{3.8}$$

where $ABCD$ denotes the area delimited by the vertices, A, B, C, and D. The change in stored field energy is

$$\Delta W_f = OBC - OAD, \tag{3.9}$$

where, e.g., OBC denotes the area delimited by the curve OB and the vertex C.

Finally, the mechanical work done is

$$\begin{aligned} \Delta W_m &= T\Delta\theta \\ &= \Delta W_{\text{total}} - \Delta W_f \\ &= ABCD - (OBC - OAD) \\ &= (ABCD + OAD) - OBC \\ &= OAB. \end{aligned} \tag{3.10}$$

Thus, noting that OAB is also the change in coenergy, we conclude that the mechanical work done is exactly equal to the change in coenergy.

In the unsaturated region, the instantaneous torque is easily derived because the coenergy is always equal to the stored field energy, as shown in Figure 3.6. Since the

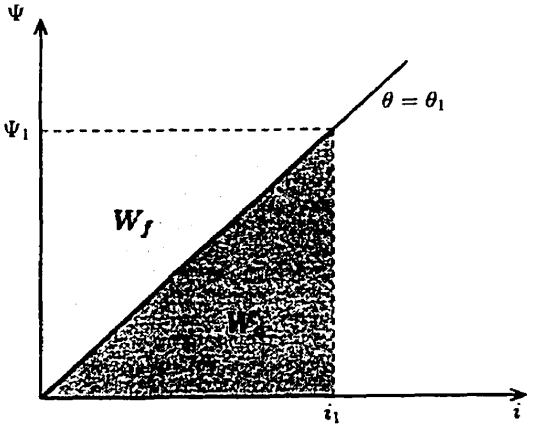

Figure 3.6: Coenergy in the unsaturated region

flux-linkage in the unsaturated region is a linear function of phase current, as shown in (3.4), the coenergy is found by substituting (3.4) into (3.7):

$$\begin{aligned} W_c(\theta, i) &= \int_0^i \Psi(\theta, i^*)di^* \\ &= \int_0^i L(\theta)i^* di^* \\ &= \frac{1}{2}L(\theta)i^2. \end{aligned} \tag{3.11}$$

Substituting (3.11) into (3.6) gives the instantaneous torque in the unsaturated region as

$$\begin{aligned} T(\theta, i) &= \frac{\partial W_c(\theta, i)}{\partial \theta} \\ &= \frac{\partial}{\partial \theta}\left(\frac{1}{2}L(\theta)i^2\right) \\ &= \frac{1}{2}i^2\frac{dL(\theta)}{d\theta}. \end{aligned} \tag{3.12}$$

Figure 3.7 shows the basis of torque production in the unsaturated region with an idealized linear variation of phase inductance over one rotor pole-pitch. The aligned

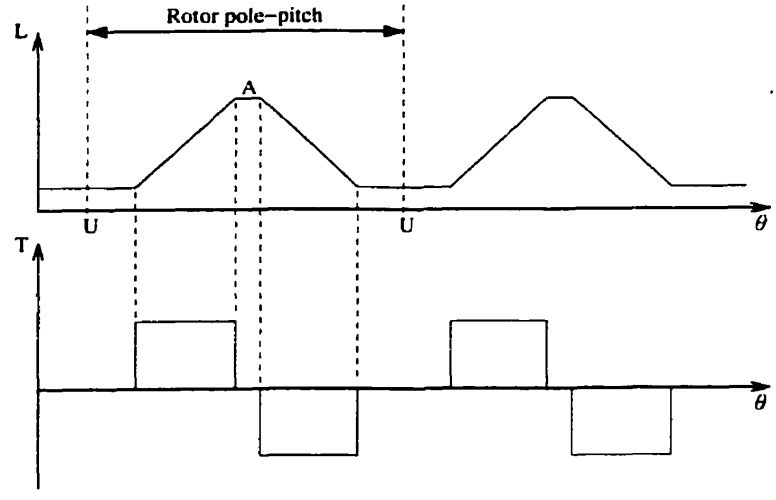

Figure 3.7: Torque production in the unsaturated region

and unaligned positions are denoted by A and U, respectively. As the stator and rotor poles start to overlap, the inductance increases from the unaligned value, L_{min}, eventually reaching the fully aligned value, L_{max}. In the figure, the torque is shown for a constant current in one phase. Notice that the sign of the torque depends on the sign of the change in inductance with respect to the rotor angle, i.e., $\frac{dL(\theta)}{d\theta}$. Therefore, in order to produce only positive torque, the phase windings must be energized only during the rising inductance period. Hence, this period is called the *effective torque zone* and is approximated to the lesser pole-arc of the overlapping stator and rotor poles.

For the continuous torque production with all the phases in an 8/6 SR machine, consider Figure 3.8. We number stator poles as shown, in a clockwise fashion. Let θ

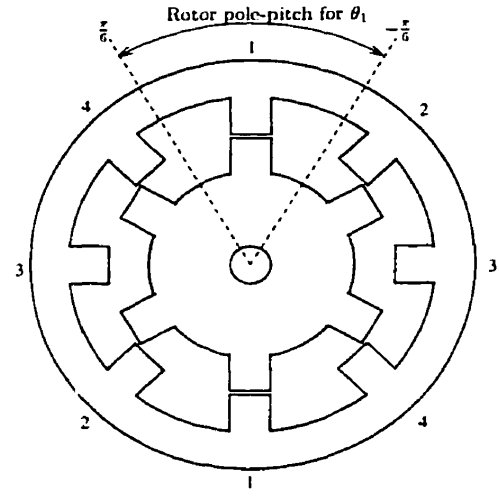

Figure 3.8: Phases and their range

denote the rotor angle, reference value being when a reference rotor pole is vertically up. The range of θ is $(-\infty, \infty)$. In addition, we have four phase angles, θ_p $(p = 1, \ldots, 4)$. The range of these angles is $[-\frac{\pi}{6}, \frac{\pi}{6})$. These angles denote distances between stator and rotor poles, as follows. The first angle, θ_1, denotes the distance from stator pole 1 to the nearest rotor pole. That is, the graph of θ_1 as a function of θ is as follows:

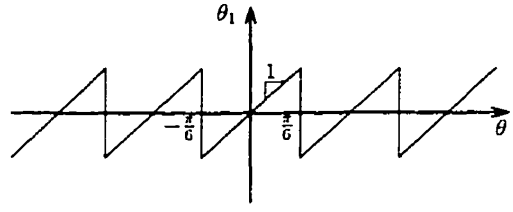

Figure 3.9: Phase angle θ_1 as a function of θ ranging from $-\frac{\pi}{6}$ to $\frac{\pi}{6}$

Likewise, θ_2 is the distance from stator pole 2 to the nearest rotor pole. The graph of θ_2 as a function of θ is the previous graph shifted to the right by $\frac{\pi}{12}$, that is,

$$\theta_2(\theta) = \theta_1(\theta - \frac{\pi}{12}). \tag{3.13}$$

And so on for θ_3 and θ_4.

The relationships between θ and the phase angles are shown in Figure 3.10. The

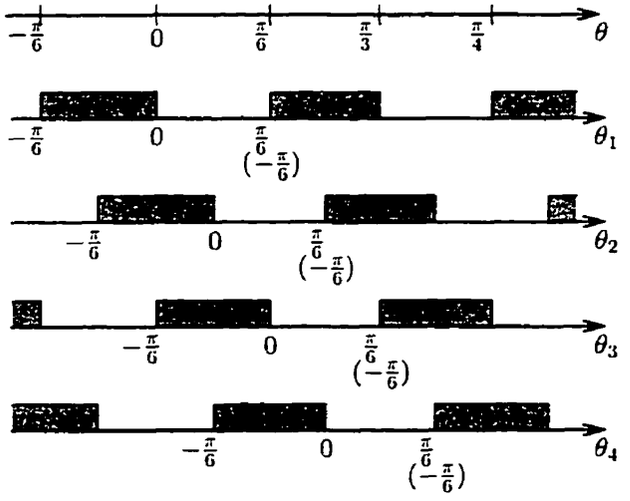

Figure 3.10: Relationships between θ and θ_p

shaded area represents the phase excitation period for producing positive torque in each phase. The process is controlled by switching the supply voltage on at the *turn-on angle*, θ_{on}, and switching off at the *turn-off angle*, θ_{off}. In general, the turn-on and turn-off angles are chosen to maximize the performance of an SR machine, such as efficiency and torque density. However, the most important principle in choosing θ_{on} and θ_{off} is to produce always nonzero torque. Notice that the effective torque zone in one phase overlaps with adjacent phases. Hence, by choosing proper θ_{on} and θ_{off}, continuous torque is produced. The control aspect of turn-on and turn-off angles is described in the next chapter in detail.

The operation in the saturated region is similar to that in the unsaturated region except that the output torque is larger and has a distorted shape. The purpose of operating an SR machine in the saturated region is to increase the torque density, i.e., torque per unit volume. As the phase current is increased to the saturated region, the coenergy takes up a larger portion of the total input energy. Hence, with the same size of machine, larger torque can be produced. Because the torque density of unsaturable machines is very low, they are not of practical interest.

3.2.3 Curve-fit Equation

Since it is too complicated to model the exact magnetization curves from the geometry of an SR machine, the values of flux-linkage are usually measured experimentally for various rotor positions and current levels. Then, the data are used in a controller design by utilizing a look-up table or by curve-fitting with an equation (see e.g., [4, 30, 34]).

For our simulation study, a Fourier series approximation was taken from [4] as a detailed mathematical expression for the magnetization curves of a regular SR machine. The mathematical expression for flux-linkage is given by

$$\Psi(\theta, i) = \sum_{n=1}^{M} c_{0n} \left[\frac{1}{1 + e^{c_{1n}\theta - c_{2n}}} + \frac{1}{1 + e^{-c_{1n}\theta - c_{2n}}} - c_{3n} \right] \left[\frac{2}{1 + e^{-c_{4n} i}} - 1 \right], \qquad (3.14)$$

where M is the order of the Fourier series. The parameters c_{jn} are obtained by curve-fitting the measured flux-linkage data by use of the steepest descent method (see, e.g., [24]). The coefficients of the fifth-order series for a 4kW 8/6 four-phase SR machine were taken from [4] and are

$$[c_{jn}] = \begin{bmatrix} 0.6002 & 1.169 & 1.071 & 0.1723 & 0.1768 \\ 26.05 & 13.60 & 12.11 & 12.98 & 12.99 \\ 8.770 & 3.741 & 3.250 & 1.715 & 1.720 \\ 0.3306 & 1.144 & 1.274 & 1.378 & 1.381 \\ 0.05593 & 0.8016 & 0.9709 & 1.004 & 1.005 \end{bmatrix}$$

where $j = 0, \ldots, 4$ is the row parameter and $n = 1, \ldots, 5$ is the column parameter. The average error against the real data is 0.004025. A plot of the magnetization curves is shown in Figure 3.11.

The Fourier series above enjoys the following properties: (1) zero slope at the stator pole axis of symmetry, (2) symmetry about the stator pole axis, (3) integrability with respect to phase current, and (4) differentiability with respect to rotor angle and phase current. Property (1) ensures that the motor torque is zero in the aligned position. Property (2) provides symmetrical electromagnetic characteristics. Property (3) allows the coenergy to be formulated by integrating the Fourier series

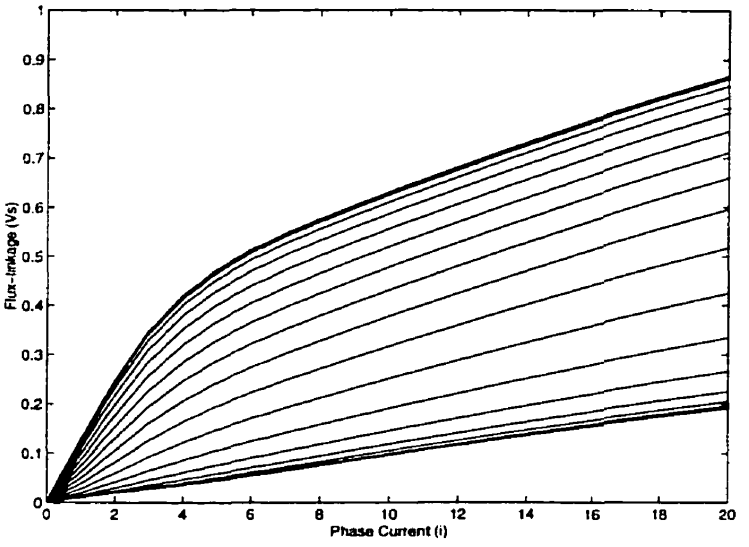

Figure 3.11: Magnetization curves of approximated flux-linkage model

with respect to the phase current. Property (4) ensures that a torque equation can be obtained by differentiating the coenergy equation with respect to the rotor angle. Property (4) also allows the derivation of electrical dynamic equations described in the next section.

From (3.7), the coenergy, W_c, is found by integrating (3.14) with respect to i, assuming $i \geq 0$,

$$\begin{aligned} W_c(\theta, i) &= \int_0^i \Psi(\theta, i^*) di^* \\ &= \sum_{n=1}^{M} c_{0n} \left[\frac{1}{1 + e^{c_{1n}\theta - c_{2n}}} + \frac{1}{1 + e^{-c_{1n}\theta - c_{2n}}} - c_{3n} \right] \left[\frac{2\ln(1 + e^{-c_{4n}i}) - 2\ln(2)}{c_{4n}} + i \right]. \end{aligned} \tag{3.15}$$

From (3.6), the instantaneous torque, T, is found by differentiating (3.15) with respect to θ, assuming $i \geq 0$,

$$\begin{aligned} T(\theta, i) &= \frac{\partial W_c(\theta, i)}{\partial \theta} \\ &= \sum_{n=1}^{M} c_{0n} \left[\frac{-c_{1n} e^{c_{1n}\theta - c_{2n}}}{(1 + e^{c_{1n}\theta - c_{2n}})^2} + \frac{c_{1n} e^{-c_{1n}\theta - c_{2n}}}{(1 + e^{-c_{1n}\theta - c_{2n}})^2} \right] \left[\frac{2\ln(1 + e^{-c_{4n}i}) - 2\ln(2)}{c_{4n}} + i \right]. \end{aligned} \tag{3.16}$$

3.3 Electrical Model

In this research, the voltage drops in transistor switches and freewheeling diodes are assumed to be very small compared to the magnitude of the voltage supply and the emf induced in the coils, and hence are neglected. The magnitude of the voltage supply stays the same during the machine operation. However, the sign of the voltage applied to the coil switches between positive and negative. The approximated circuit for one phase in an SR machine, shown in Figure 3.12, is an RL circuit with a coil resistance, a variable inductance, and a variable (positive/negative) voltage supply.

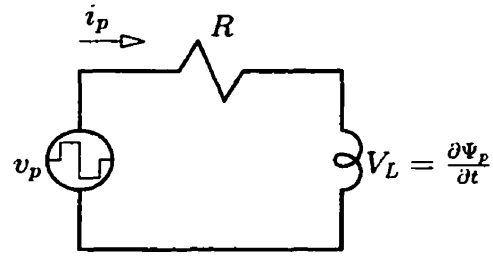

Figure 3.12: Simplified RL circuit

The dynamics of the RL circuit is governed by Kirchhoff's voltage law,

$$v - V_R - V_L = 0, \tag{3.17}$$

where v is the variable voltage supply, and V_R and V_L are the voltage across the coil resistance, R, and the induced emf across the excitation coil, respectively. From Ohm's law, the voltage drop across the coil resistance is given by

$$V_R = Ri. \tag{3.18}$$

The induced emf across the excitation coil is described by Faraday's law,

$$V_L = \frac{d\Psi}{dt}. \tag{3.19}$$

Since the flux-linkage is a function of rotor angle and phase current, the induced emf is expressed by applying the chain rule,

$$V_L = \frac{d\Psi}{dt} = \frac{\partial \Psi}{\partial i}\frac{di}{dt} + \frac{\partial \Psi}{\partial \theta}\frac{d\theta}{dt}. \tag{3.20}$$

where $\frac{\partial \Psi}{\partial i}$ and $\frac{\partial \Psi}{\partial \theta}$ are referred to as the incremental inductance and the back emf coefficient, respectively. Substituting (3.18) and (3.20) into (3.17) gives

$$v - Ri - \left(\frac{\partial \Psi}{\partial i} \frac{di}{dt} + \frac{\partial \Psi}{\partial \theta} \frac{d\theta}{dt} \right) = 0. \tag{3.21}$$

By solving (3.21) for $\frac{di}{dt}$ and substituting $\frac{d\theta}{dt} = \omega$, we obtain the dynamic equation of the electrical circuit,

$$\frac{di}{dt} = \left(\frac{\partial \Psi}{\partial i} \right)^{-1} \left(v - Ri - \frac{\partial \Psi}{\partial \theta} \omega \right). \tag{3.22}$$

Bringing in (3.14), we have

$$\frac{\partial \Psi(\theta, i)}{\partial i} = \sum_{n=1}^{M} c_{0n} \left[\frac{1}{1 + e^{c_{1n}\theta - c_{2n}}} + \frac{1}{1 + e^{-c_{1n}\theta - c_{2n}}} - c_{3n} \right] \left[\frac{2 c_{4n} e^{-c_{4n} i}}{(1 + e^{-c_{4n} i})^2} \right], \tag{3.23}$$

$$\frac{\partial \Psi(\theta, i)}{\partial \theta} = \sum_{n=1}^{M} c_{0n} \left[\frac{-c_{1n} e^{c_{1n}\theta - c_{2n}}}{(1 + e^{c_{1n}\theta - c_{2n}})^2} + \frac{c_{1n} e^{-c_{1n}\theta - c_{2n}}}{(1 + e^{-c_{1n}\theta - c_{2n}})^2} \right] \left[\frac{2}{1 + e^{-c_{4n} i}} - 1 \right]. \tag{3.24}$$

3.4 Final Mathematical Model

As a result of the discussion above, we obtain the following mathematical model describing the dynamics of the SR machine under consideration:

$$\begin{aligned} \dot{\theta} &= \omega, \\ \dot{\omega} &= \frac{1}{J} \left(\sum_{p=1}^{4} T_p(\theta_p, i_p) - B\omega - T_l \right), \\ \frac{di_p}{dt} &= \left(\frac{\partial \Psi_p(\theta_p, i_p)}{\partial i_p} \right)^{-1} \left(v_p - R i_p - \frac{\partial \Psi_p(\theta_p, i_p)}{\partial \theta_p} \omega \right), \quad p = 1, \ldots, 4. \end{aligned} \tag{3.25}$$

Here, θ, ω, θ_p, i_p, v_p, T_p, Ψ_p, J, B, R, and T_l are rotor position, rotor speed, phase angle, phase current, phase voltage, phase torque, phase flux-linkage, moment of inertia, friction coefficient, phase resistance, and load torque disturbance, respectively. The expression for T_p, $\frac{\partial \Psi_p}{\partial i_p}$, and $\frac{\partial \Psi_p}{\partial \theta_p}$ are as follows (Note that the coefficients taken

from [4] are for a 4kW 8/6 SR machine):

$$T_p(\theta_p, i_p) = \sum_{n=1}^{M} c_{0n} \left[\frac{-c_{1n} e^{c_{1n}\theta_p - c_{2n}}}{(1 + e^{c_{1n}\theta_p - c_{2n}})^2} + \frac{c_{1n} e^{-c_{1n}\theta_p - c_{2n}}}{(1 + e^{-c_{1n}\theta_p - c_{2n}})^2} \right] \left[\frac{2\ln(1 + e^{-c_{4n} i_p}) - 2\ln(2)}{c_{4n}} + i_p \right],$$

$$\frac{\partial \Psi_p(\theta_p, i_p)}{\partial i_p} = \sum_{n=1}^{M} c_{0n} \left[\frac{1}{1 + e^{c_{1n}\theta_p - c_{2n}}} + \frac{1}{1 + e^{-c_{1n}\theta_p - c_{2n}}} - c_{3n} \right] \left[\frac{2 c_{4n} e^{-c_{4n} i_p}}{(1 + e^{-c_{4n} i_p})^2} \right],$$

$$\frac{\partial \Psi_p(\theta_p, i_p)}{\partial \theta_p} = \sum_{n=1}^{M} c_{0n} \left[\frac{-c_{1n} e^{c_{1n}\theta_p - c_{2n}}}{(1 + e^{c_{1n}\theta_p - c_{2n}})^2} + \frac{c_{1n} e^{-c_{1n}\theta_p - c_{2n}}}{(1 + e^{-c_{1n}\theta_p - c_{2n}})^2} \right] \left[\frac{2}{1 + e^{-c_{4n} i_p}} - 1 \right].$$

Therefore, the form of the model is a state equation, $\dot{\underline{x}} = \underline{f}(\underline{x}, \underline{v})$, where the components of $\underline{x}$ are θ, ω, $i_1, \ldots, i_4$ and of $\underline{v}$ are $v_1, \ldots, v_4$.

Chapter 4

Control of Switched Reluctance Machines

The typical application of an SR machine is a variable-speed drive. In this chapter, we focus on the speed tracking control of an SR machine. Because the torque production of an SR machine depends on the timing of phase excitation and the magnitude of phase current, an SR machine employs electrical hardware suitable for the switching of excited phases and the control of desired current waveforms. In the following, we introduce the traditional feedback control algorithm of an SR machine, which operates in two different modes depending on the operating speed. The control of current waveforms and commutation angles is explained in detail. Next, the control objectives and constraints of this research are described. Finally, an SR machine controller is designed in the traditional control framework with the use of a PI controller, and the simulation results are presented. A useful reference for this chapter is found in [22].

4.1 Speed Tracking Control

In the previous chapter, we derived the state dynamic equations of an 8/6 four-phase SR machine. We can now construct the general block diagram of speed tracking feedback control for the SR machine as shown in Figure 4.1. The state model describes

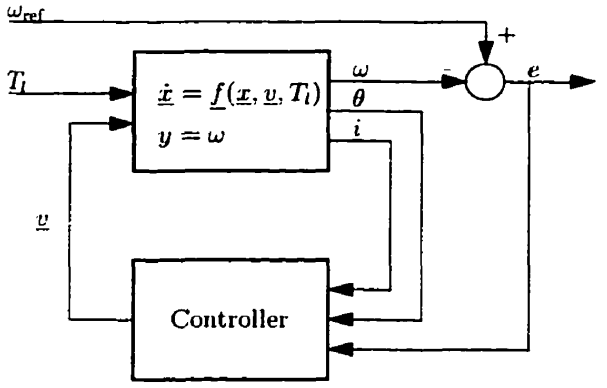

Figure 4.1: General block diagram of SR machine feedback control

the plant block, where the plant input is the phase voltage vector, $\underline{v} \in \mathbb{R}^4$, and the plant output y is the rotor speed ω. The load disturbance torque T_l is also added to the plant. We assume that the SR machine contains sensors to measure the rotor position θ and the phase currents, $\underline{i} \in \mathbb{R}^4$. The actual rotor speed ω is estimated by differentiating the rotor position with respect to time. The speed error, e, is obtained by subtracting the estimated rotor speed from the reference speed, ω_{ref}. In other words, the entire state of the system is available for feedback. The feedback controller takes θ, $\underline{i}$, and e as inputs and finds a phase voltage vector $\underline{v}$ such that the speed error approaches zero asymptotically. In the following, the traditional control algorithm of an SR machine is presented and discussed.

4.1.1 Feedback Loops

The traditional control algorithm of an SR machine consists of three feedback loops. This is based on the natural characteristics of torque production in an SR machine. Since the mechanical dynamics of an SR machine are governed by the total instantaneous torque, and the torque equation is a function of rotor position and phase current, the speed tracking in an SR machine can be achieved by controlling the timing of phase excitation and the current waveforms. The goal of the controller is to determine desirable turn-on angle θ_{on}, turn-off angle θ_{off}, and reference current waveform, i_{ref}, according to the speed error and to find phase voltage signals that control

the phase excitations as desired.

The commutation of phase excitation can be easily accomplished with the switching circuit described in Chapters 2 and 3. The phase angles are calculated from the rotor position in real time, and the transistor switches are turned on and off at the desired turn-on and -off angles. On the other hand, control of current waveforms is not as straightforward as the phase commutation. As the plant input is voltage signals (switched among positive, negative, and zero values), the phase current is drawn according to the phase resistance, back emf, and phase inductance, all of which vary as the rotor rotates. The back emf and phase inductance also vary with phase current because of magnetic saturation. Recall the current dynamic equation from (3.25),

$$\frac{di}{dt} = \left(\frac{\partial \Psi}{\partial i}\right)^{-1} \left(v - Ri - \frac{\partial \Psi}{\partial \theta}\omega\right). \tag{4.1}$$

Since the incremental inductance $\frac{\partial \Psi}{\partial i}$ is always positive, one can see that the current increases when the phase voltage v is greater than the sum of the voltage drop across the phase resistance, Ri, and the back emf, $\frac{\partial \Psi}{\partial \theta}\omega$, and it decreases when the phase voltage is less. With a relatively large DC voltage supply, it is therefore possible to regulate the dynamics of phase current by applying positive and negative phase voltages in the switching circuit. In practice, the sign of phase voltage is controlled by the use of hysteresis control. Thus, the traditional control system consists of three feedback loops:

i) The speed error feedback to determine θ_{on}, θ_{off}, and i_{ref},

ii) The phase current feedback to determine signs of phase voltage signals,

iii) The rotor position feedback to obtain phase angles θ_p for commutations.

The block diagram of the traditional control system is shown in Figure 4.2.

4.1.2 Operating Modes

There are two operating modes in the traditional control algorithm. This is because there is a limit in controlling the current dynamics by the phase voltage. As the

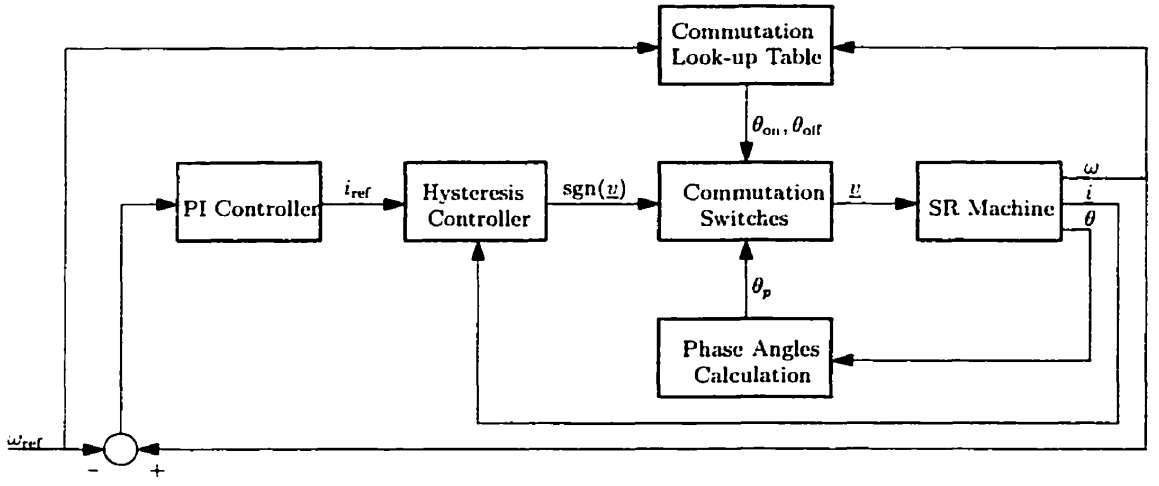

Figure 4.2: Block diagram of the traditional feedback control

rotor speed increases, the back emf in (4.1) increases, and therefore, beyond a certain speed, the back emf exceeds the magnitude of the DC voltage supply. Hence, in the low speed operation, the rotor speed is controlled by phase voltage signals shaping the current waveform. In the high speed operation, turn-on and turn-off angles are shifted to control the rotor speed.

The control strategy of the two operating modes can be also explained in the torque-speed relationship of an SR machine. A typical relationship between the total instantaneous torque T_{total} and the rotor speed ω is shown in Figure 4.3. The figure shows the maximum torque that can be produced at various speeds. Like other electrical machines, an SR machine has a constant rated output power, P_{rated}, and its output torque must be limited by setting

$$T_{\text{total}}\omega = P_{\text{rated}}. \tag{4.2}$$

The equation above shows that the torque is inversely proportional to the rotor speed. For the low speed operation, however, the maximum torque (and hence maximum current) must be limited to protect the electrical hardware of an SR machine. Thus, the torque characteristic from zero speed to the rated speed, ω_{rated}, is separated into two regions. The first region is where the torque is limited by the maximum current level, and the second region is where the torque is limited by the rated output power.

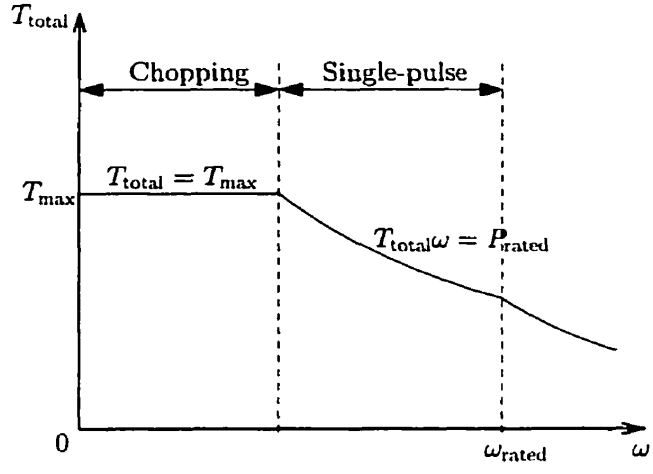

Figure 4.3: Torque - speed relationship

In the first region, the operation is called the *chopping mode* because the output torque is controlled by phase voltage signals chopping the current waveforms. The operation in the second region is called the *single-pulse mode* because the phase voltage is no longer capable of regulating the current dynamics, and hence phase current is a single pulse. Each operation mode is explained in the following.

4.1.3 Chopping Mode

In the chopping mode, a desired current waveform is first obtained. A reference current i_{ref} is formed in such a way that when the actual current is approximately equal to i_{ref}, the resulting rotor speed approaches the desired speed. In the traditional control of an SR machine, a PI controller is utilized to find i_{ref} from the speed error in the feedback control.

Assuming that a reference current is given in the feedback control, the actual phase current is regulated to follow i_{ref} by a phase voltage signal. Figure 4.4 shows the waveforms of idealized inductance, voltage signal, flux-linkage, and phase current obtained with a hysteresis-type current regulator. One rotor pole-pitch is shown, and the aligned and unaligned positions are denoted by A and U, respectively. In the hysteresis control, the power transistors are switched on and off according to

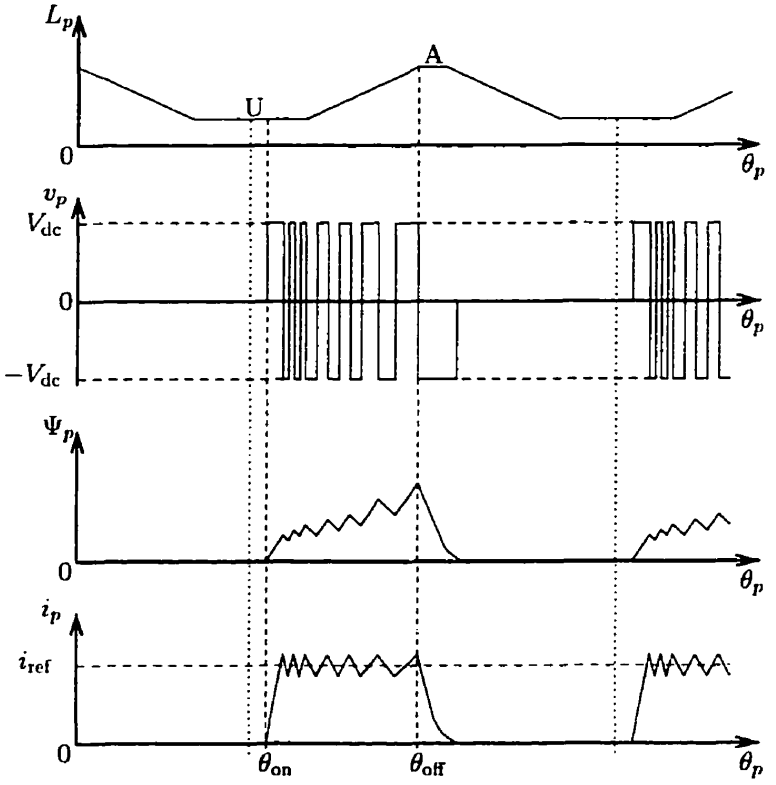

Figure 4.4: Waveforms in chopping mode

whether the current is greater or less than a reference current. The instantaneous phase current is measured using a wide-bandwidth current transducer and fed back to a summing junction. The current error is used directly to control the states of the power transistors. The result is the square pulses of phase voltage signal switching between positive and negative values during the rising inductance period.

The simple hysteresis controller maintains the current waveform around the reference current between an upper and a lower limit of the *hysteresis band.* The hysteresis bandwidth determines the switching frequency of voltage signals. The smaller the bandwidth, the faster the switching occurs. Because power transistors have a limit in switching frequency, the bandwidth is selected accordingly. As shown in (4.1), the phase inductance $\frac{\partial \Psi}{\partial i}$ also has a large influence on the dynamics of phase current and hence on the switching frequency. Since the phase inductance of an unsaturable SR machine increases linearly as the rotor approaches the aligned position, the rate of

change of current decreases, and therefore the switching frequency also decreases as shown in the figure.

In an unsaturable SR machine, the flux-linkage is a linear function of phase current, and therefore it behaves similarly as the phase inductance under an approximately constant current. It starts from zero at the unaligned position and increases almost linearly as the stator and rotor poles start to overlap. In motoring operation, the flux should ideally be reduced to zero before the poles begin to separate, otherwise the torque changes its sign and becomes a braking torque. Therefore, the phase voltage is reversed at the end of every phase excitation in order to force the phase current down to zero. In practice, it is allowed to have non-zero current extending beyond the aligned position as long as the positive torque gained at the end of the rising inductance period exceeds the braking torque produced in the beginning of the falling inductance period.

The waveforms under magnetic saturation are similar to those in Figure 4.4 except that the phase inductance does not increase very much as the rotor rotates from the unaligned position to the aligned position. Thus, the switching frequency does not decrease as much during the commutation of a saturated SR machine.

4.1.4 Single-pulse Mode

Figure 4.5 shows the waveforms of idealized inductance, voltage signal, flux-linkage, and phase current in the single-pulse mode. Since this operating mode is specifically applied in the high speed operation, the time period during which the rotor rotates for one rotor pole-pitch is much smaller than that in the chopping mode. As explained earlier, the phase voltage is no longer capable of chopping the current waveform because of a large back emf. Hence, the phase voltage is kept positive during the entire phase excitation period until defluxing occurs.

In Figure 4.5, the supply voltage is turned on well ahead of the overlapping of the stator and rotor poles in order to ensure that the phase current increases to an adequate level while the inductance is still low. The rising inductance generates a back emf which consumes an increasing proportion of the supply voltage, and hence

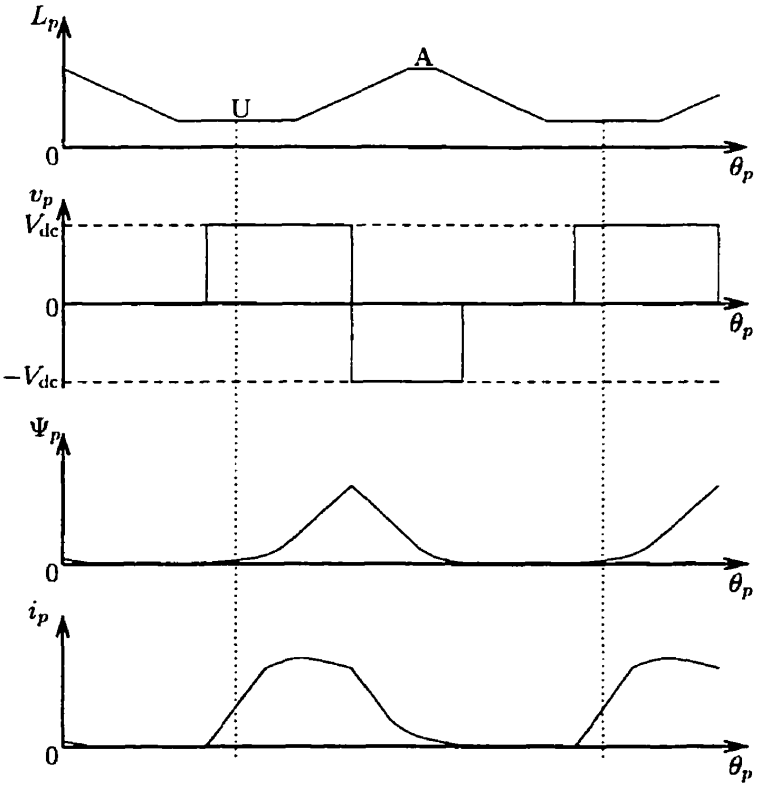

Figure 4.5: Waveforms in single-pulse mode

the rate of change of current decreases dramatically once the stator and rotor poles start to overlap. Since the back emf exceeds the supply voltage, the voltage applied to the phase windings is reversed, and hence current slowly decreases. In order to avoid a braking torque produced in the falling inductance period, the reverse voltage is applied prior to the aligned position for defluxing. At the point of commutation, there is a sharp increase in the rate of change of current.

At the aligned position, the back emf reverses so that, instead of augmenting the negative voltage applied to the terminal, the back emf tries to cancel it out. Thus, the rate of fall of current decreases. In this period, there is a danger that the back emf may exceed the supply voltage and cause the current to start increasing again. Therefore, in the single-pulse mode, the turn-off angle must be advanced as the speed increases.

4.1.5 Commutation Angles

As explained above, the commutation angles play an important role in the control of an SR machine. The basic principle of selecting turn-on and turn-off angles is to optimize the machine performance depending on the operating speed. In the traditional control, the commutation angles are shifted towards the unaligned position as the operating speed increases. Figure 4.6 shows the variation of turn-on and turn-off angles with rotor speed. From the initial speed, the commutation angles are

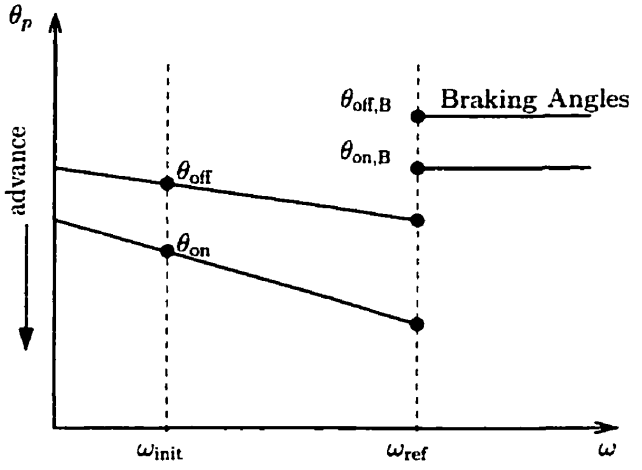

Figure 4.6: Variation of commutation angles with respect to rotor speed

advanced as the rotor speed approaches the reference speed. When the speed exceeds the reference speed, the commutation angles are switched to the braking angles.

In early research, the commutation strategy was developed for a discrete set of commutation angles for the purpose of reducing the cost of rotor position sensors (see, e.g., [1, 22]). In this strategy, the commutation angles are selected for four operation modes, *Normal*, *Boost*, *Long-dwell*, and *Brake*. The commutation angles in Normal Mode are selected for the low speed operation, and as the operating speed is increased, the commutation mode moves on to Boost and Long-dwell. Reference [1] studied a 6/4 three-phase SR machine and chose the commutation angles for each mode as shown in Table 4.1. In [1], the unaligned and aligned phase angles are 45° and 90°, respectively. The rotor pole-pitch of a 6/4 SR machine is 90°. The

Table 4.1: Discrete commutation angles for 6/4 SR machines in different operating speeds (unaligned position: 45°, aligned position: 90°)

	Turn-on	Turn-off
Normal	52.5°	82.5°
Boost	37.5°	67.5°
Long-dwell	37.5°	82.5°
Brake	82.5°	112.5°

commutation signals for a 6/4 SR machine with an idealized induction waveform are shown in Figure 4.7. In the Normal Mode, the turn-on angle is chosen right before the

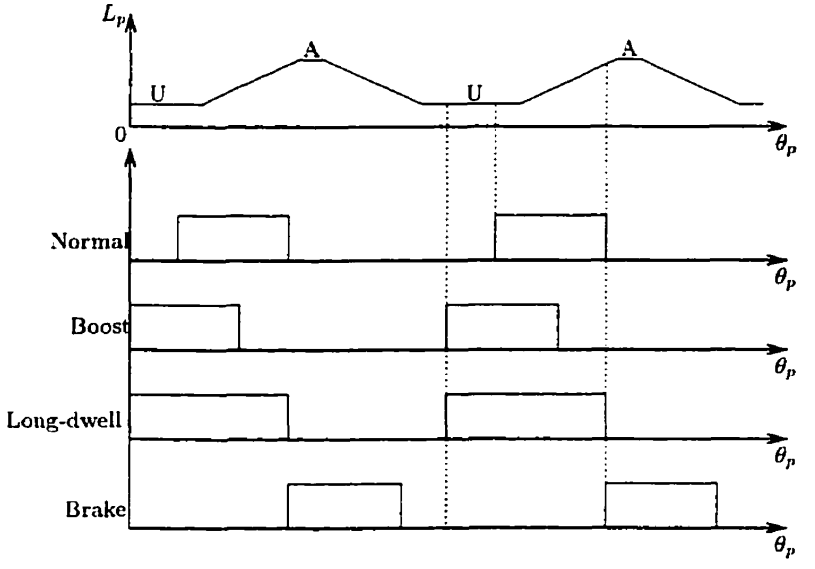

Figure 4.7: Commutation signals in four modes of operating speeds

effective torque zone while the turn-on angle in the Boost Mode is chosen well ahead of the overlapping of stator and rotor poles. The phase excitation in the Normal Mode is turned off just before the aligned position, while the phase excitation in the Boost Mode is turned off soon after the overlapping of stator and rotor poles. The Long-dwell Mode is a combination of the two modes, and research shows that it provides the highest torque. The price for this high torque, however, is a high phase current. Brake Mode is used in the traditional control under the assumption that some rotational friction is present. In the Brake Mode, exciting the phase windings in the falling inductance period produces negative torque. With proper combination

of these four operation modes, a wide range of operating speeds can be achieved.

In recent research, more precise commutation strategies are studied to achieve optimal performance of SR machines (see, e.g., [13, 14]). The performance indices considered in the research are efficiency, measured by torque per ampere, and torque density, measured by torque per unit volume. In the new algorithms, the turn-on and turn-off angles are calculated either off-line or in real time to provide a continuous set of commutation angles. With the detailed knowledge of individual machine characteristics, the measures of efficiency and torque density can be expressed as functions of the commutation angles and the operating speed. Reference [14] shows that the turn-on angle is selected to maximize the efficiency, and the turn-off angle is chosen to maximize the output torque. Reference [31] presents self-tuning control to maximize the efficiency even in the presence of parameter uncertainty.

4.2 Design of SR Machine Controller

In this section, a speed tracking controller for an 8/6 SR machine is designed in the traditional control framework. First, the control objectives and constraints in this research are described. Then, a PI controller is designed to find the reference current in the chopping mode. The controller is tested in the simulations with Matlab/Simulink, and the simulation results are presented at the end.

4.2.1 Control Objectives and Constraints

The control objectives in this research are as follows:

- Stability of the feedback system.
- Small steady state error in speed tracking control.
- Robustness in the presence of disturbance load torque.

This research is restricted to the low speed operation of an SR machine. Therefore, we design a controller for the chopping mode. For simplicity, we use a fixed set of commutation angles used in the Normal Mode.

The turn-on and turn-off angles for the 8/6 SR machine in the Normal Mode are calculated from the commutation angles for the 6/4 SR machine. Assuming that the pole-arc angle and interpolar angle of the stator in a regular SR machine are approximately the same, we can calculate the pole-arc angle of the stator in the 6/4 SR machine by dividing 360° by 12, that is, 30°. Figure 4.8(a) shows that the turn-on angle of the 6/4 SR machine (52.5°) is exactly at the center of the unaligned position (45°) and the beginning of the overlapping period between the stator and rotor poles (60°). The turn-on angle is 7.5° before the effective torque zone. Notice

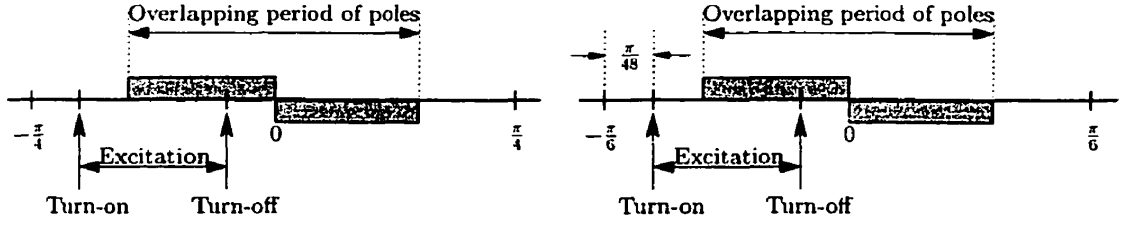

(a) Commutation angles for 6/4 SR machine in Normal Mode

(b) Commutation angles for 8/6 SR machine in Normal Mode

Figure 4.8: The commutation angles for 6/4 and 8/6 SR machines in Normal Mode

that the turn-off angle of the Normal Mode (82.5°) is 7.5° before the aligned position (90°). Likewise, we find that the pole-arc angle of the stator in the 8/6 SR machine is 22.5° (dividing 360° by 16) or $\frac{\pi}{8}$. Hence, the beginning of the overlapping period is −22.5° as shown in Figure 4.8(b). The turn-on angle is chosen to be the center of the unaligned position (−30°) and the beginning of the overlapping period (−22.5°), that is, −26.25° (or $-\frac{\pi}{6} + \frac{\pi}{48}$). The turn-off angle is chosen to be −3.75° (or $-\frac{\pi}{48}$). The turn-on and turn-off angles for the 8/6 SR machine are summarized in Table 4.2.

Table 4.2: Commutation angles for 8/6 SR machine in Normal and Brake Modes

	Turn-on	Turn-off
Normal	-26.25°	-3.75°
Brake	-3.75°	18.75°

4.2.2 PI Controller

As mentioned in the previous section, a PI controller is utilized in the traditional control of an SR machine. Since mechanical dynamics of electrical machines are relatively slow due to moment of inertia, a conventional PI controller is often sufficient to provide reasonable dynamic responses. However, since the state equations of an SR machine are highly nonlinear, conventional pole-placement method for the linearized model at one operating point is not suitable in designing the PI gains. In this research, a PI controller is designed based on our intuitions on SR machine operation and a trial and error method at the operating speeds in question.

As explained in Chapters 2 and 3, the basic principle of SR machine operation is to energize the phase windings while the rotor is approaching the aligned position in acceleration, and while moving away from the aligned position in braking. By assuming that the commutation angles are properly chosen, the magnitude of the phase current is varied to control the output torque, which directly controls the mechanical dynamics.

In feedback control, the speed error can be used to control the magnitude of the reference current. The larger the reference current, the larger the actual current, and hence the larger the output torque. When the total instantaneous torque is larger than the sum of the rotational friction and the disturbance torque, the rotational speed can be controlled. Thus, a PI controller is designed in such a way that it provides a sufficiently large reference current in the presence of large speed error. The integral part guarantees zero steady state error. Consider the standard expression of a PI controller,

$$i_{\text{ref}}(t) = K_p e(t) + K_i \int_0^t e(\tau) d\tau, \tag{4.3}$$

where K_p and K_i are the *proportional* and *integral gains*, respectively. This expression can be rewritten in the following expression (see, e.g., [12]):

$$i_{\text{ref}}(t) = K \left(e(t) + \frac{1}{T_i} \int_0^t e(\tau) d\tau \right). \tag{4.4}$$

Here, $K = K_p$ and $T_i = \frac{K}{K_i}$, where T_i is referred to as the *integral time*. In general, increasing K provides a faster rising time of the dynamic response of the plant.

However, large K may cause overshoot of the response and may also lead to instability. The integral time T_i is a parameter which determines the time that the PI controller takes to reduce the steady state error. The smaller the T_i, the faster the dynamic response settles to the reference value, but the larger the overshoot in the output response is. Several different combinations of gain and integral time are tested by trial and error in simulation.

4.3 Simulation Results

The traditional control algorithm was simulated in Matlab/Simulink with the state model derived for a regular 4kW 8/6 four-phase SR machine. Figure 4.9 shows the Simulink block diagram for the low speed operation. The plant blocks were built

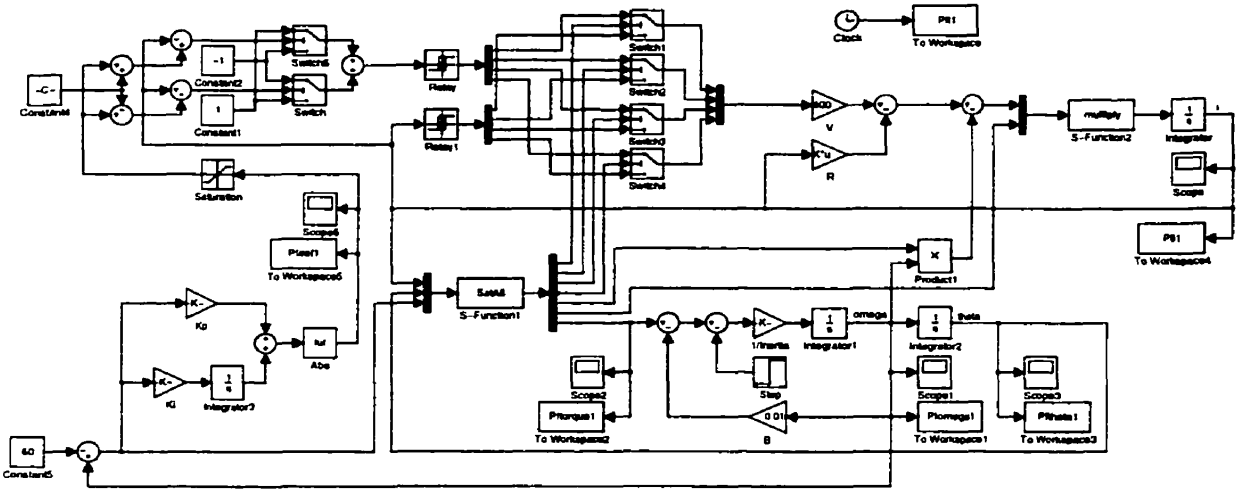

Figure 4.9: Simulink block diagram for the traditional control algorithm

according to the state model. The states θ, ω, and $\underline{i}$ are fed back to the controllers.

The control blocks consist of three parts, i.e., a PI controller, a hysteresis controller, and a commutation controller. The speed error e is obtained by subtracting ω from the reference speed ω_{ref}. The PI controller takes e as an input and produces a reference current signal i_{ref}. Since the direction of phase torque is controlled only by the commutation angles and the phase current is unipolar, the absolute value of

the PI controller output is taken for the reference current. Since the reference current is variable, the hysteresis controller is built to accommodate variable switch-on and -off points. The hysteresis controller works as a relay with memory. When the actual current hits the upper limit of the hysteresis band, the voltage signal is turned to $-V_{\rm dc}$, and when the current drops below the lower limit of the hysteresis band, the output signal is turned to $+V_{\rm dc}$. All the simulations were carried out with a fixed hysteresis bandwidth of ± 2 Amps. When the phase angle reaches the turn-off angle, the corresponding phase voltage is turned to negative until the current reaches zero and then turned off until the next commutation. An S-function block 'SatAll' (the interface block to Matlab codes) is used to calculate the phase angles and provides the switching blocks with commutation signals. The S-function block also calculates the incremental inductance, back emf coefficient, and instantaneous torque for each phase. The parameters have been taken from other literature for simulations and are given in Table 4.3.

Table 4.3: Parameters for the simulations in Matlab/Simulink.

Moment of inertia J	$0.001 kgm^2$
Rotational friction coefficient B	$0.01 Nms/rad$
Phase resistance R	1.0Ω
DC voltage source $V_{\rm dc}$	400 Volts
Hysteresis bandwidth	± 2 Amps

4.3.1 Resulting Waveforms

Simulations were run with different sets of PI gains. First, we present the waveforms of incremental inductance, voltage signal, flux-linkage, and phase current to show that the SR machine works as explained. Figure 4.10 shows the waveforms for one phase during acceleration. (The waveforms in Figure 4.10 are taken from one of the simulation results with a load disturbance torque $T_l = 10Nm$ for the purpose of illustration since its acceleration period is much longer than that of the nominal system.) It is clear that the waveform of incremental inductance is different from the idealized inductance shown earlier. While the rotor is approaching the aligned position denoted

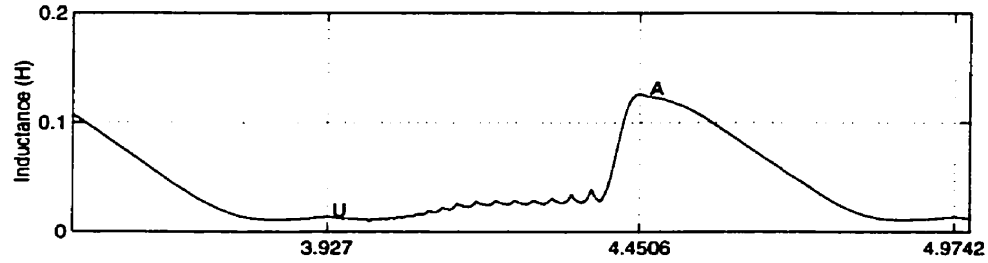

(a) Inductance

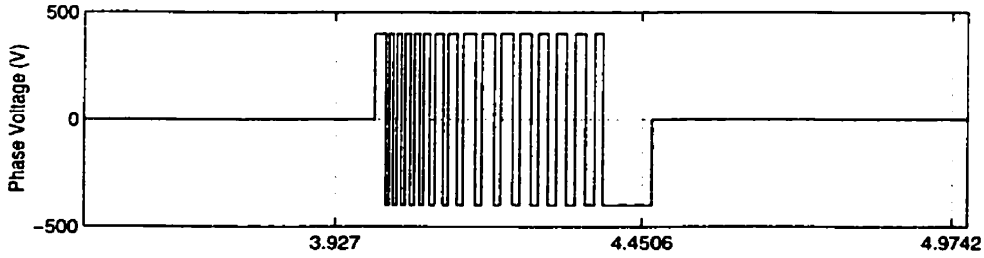

(b) Phase Voltage

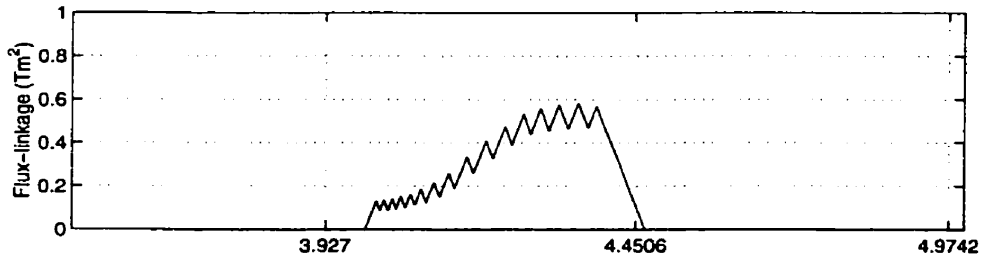

(c) Flux-linkage

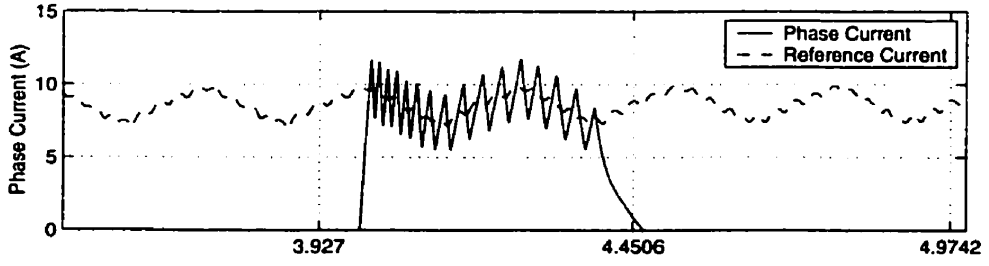

(d) Phase Current

Figure 4.10: Waveforms with respect to rotor angle θ for Chopping Mode in acceleration. A: aligned position, U: unaligned position.

as A, the phase current above the saturation current causes saturation in flux path. As a result, the inductance is low during this period. Once the phase current drops below the saturation current after the turn-off angle θ_{off}, the inductance exhibits a behavior similar to that of the idealized inductance.

As explained earlier, the phase voltage signal is generated by the hysteresis controller. According to the level of phase current with respect to the hysteresis band (reference current i_{ref} ± 2 Amps), the voltage switches between $\pm V_{\text{dc}}$. When the phase angle hits the turn-off angle θ_{off}, the voltage is turned negative until the phase current reaches zero. The slight increase in the inductance during the commutation period slows down the dynamics of phase current. Consequently, the switching frequency of voltage signal slightly decreases.

In the presence of phase current, the flux-linkage in saturation increases as the rotor approaches the aligned position. The flux-linkage and the phase current are regulated to zero outside the commutation period to avoid producing braking torque. The phase current is controlled by the voltage signal as described in the model of electrical subsystem. Figure 4.10(d) shows that the phase current is kept around the reference current by the voltage signal produced in the hysteresis controller. Notice that the reference current has oscillation. As mentioned earlier, torque ripples are caused by the torque production from each phase. This torque ripple reflects in the small oscillation in the speed dynamics. Figure 4.11 shows the speed response and the torque productions in four phases during the acceleration period. Because adjacent phase torques overlap, there are slight variations in torque magnitude over time. Consequently, the speed acceleration oscillates from phase to phase. Thus, oscillations in speed acceleration are transmitted to the reference current through the rotor speed feedback.

When the speed error is near zero at steady-state, because the commutation angles switch between the Normal Mode and the Brake Mode depending on the sign of e, both commutation modes may be present in one rotor pole-pitch. Figure 4.12 shows an example of such a situation. The waveform of inductance is close to that of idealized inductance because the phase current is below the saturation current, and hence the flux path is not saturated. Because the sign of speed error switches between

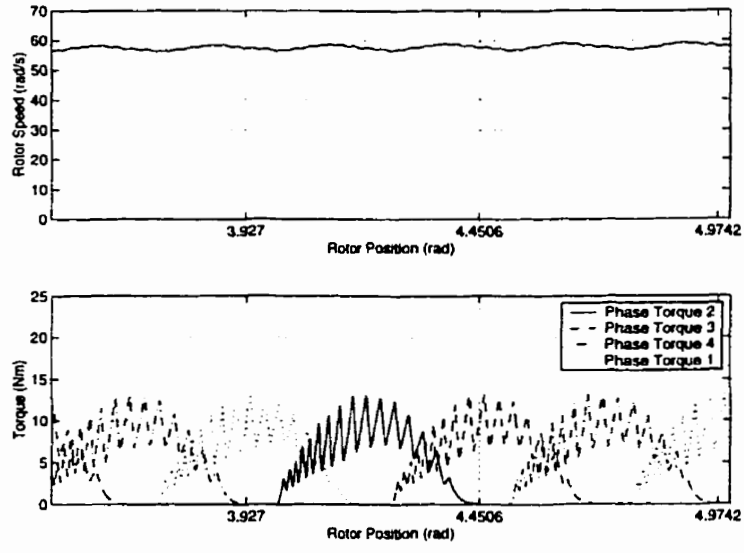

Figure 4.11: Speed response and torque waveforms in four phases in acceleration

positive and negative, the voltage signal is no longer controlled by the hysteresis controller. Instead, it is controlled by the commutation logic. Nevertheless, the phase current stays low and minimal current is applied to the mechanical subsystem to maintain the speed error near zero. In the following, the simulation results of speed tracking with various PI control gains are presented. Then, a set of gains is tuned to improve the performance of PI controller at a particular operating condition.

4.3.2 PI Gain Tuning

First, the variation of the proportional gain was tested with the nominal plant with no load disturbance. The machine inertia is set to $J = 0.001 kgm^2$. The initial conditions for the state variables are $\theta(0) = \theta_1(0) = 0$, $\omega(0) = 0$, and $i_p(0) = 0$ $(p = 1, \ldots, 4)$. Figure 4.13 shows the step response of the SR machine for the reference speed $\omega_{\text{ref}} = 60 rad/s$. The integral time was kept constant at $Ti = 0.06$ while the proportional gain was varied from 0.6 to 6.0. It is clear that increasing K allows shorter rising time but also causes undesired overshoots. The proportional gains in PI controller have an immediate effect on the reference current. The higher the gain K, the larger the output, and hence allowing phase current to increase larger.

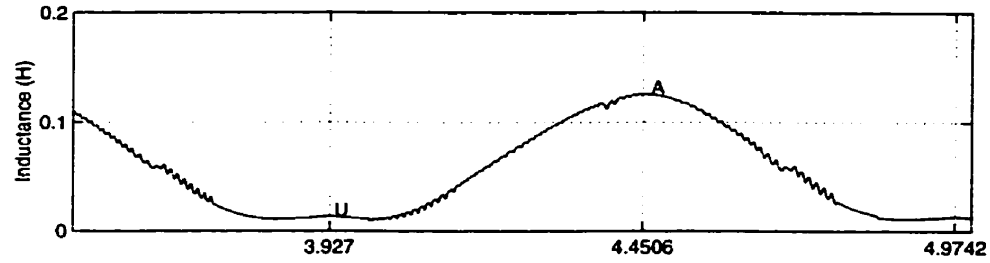

(a) Inductance

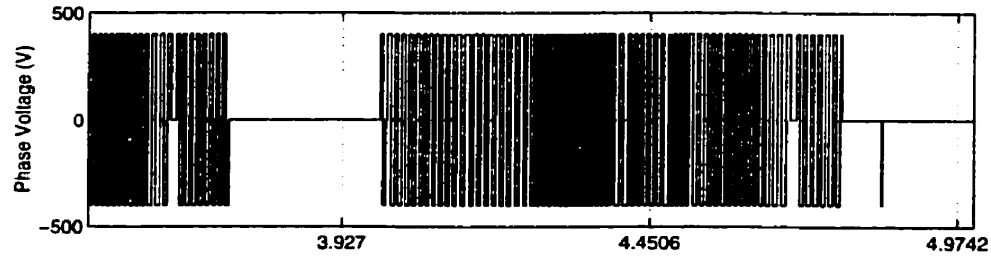

(b) Phase Voltage

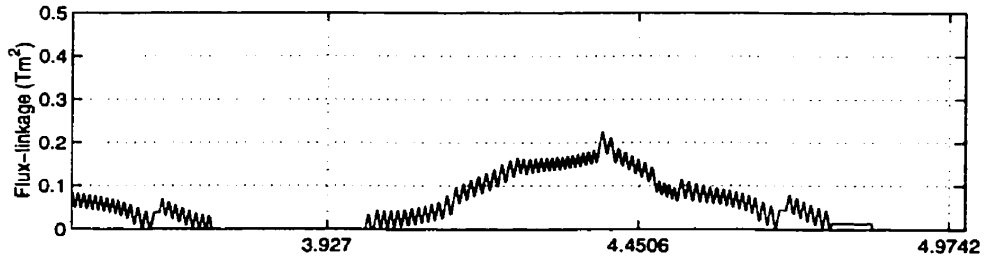

(c) Flux-linkage

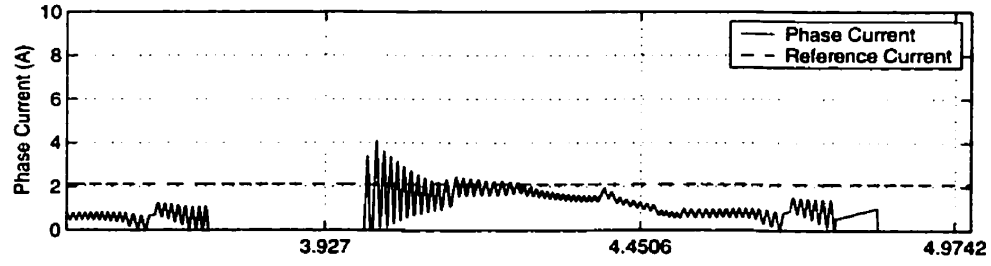

(d) Phase Current

Figure 4.12: Waveforms with respect to rotor angle θ for Chopping Mode at steady-state. A: aligned position, U: unaligned position.

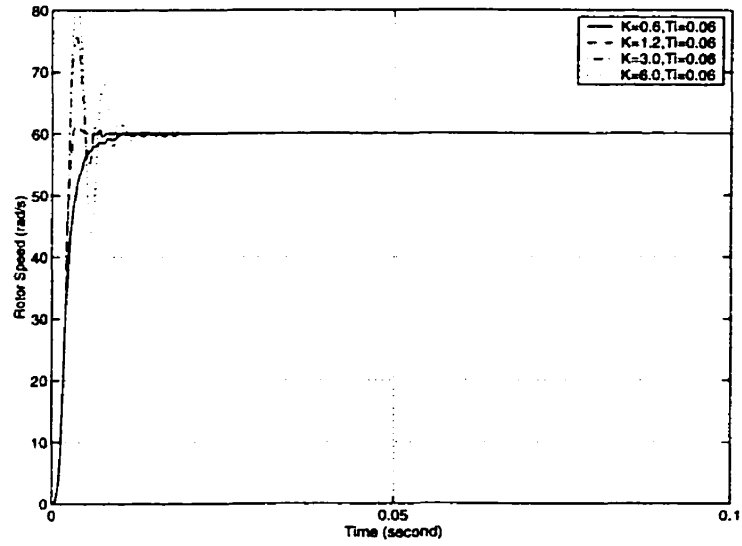

Figure 4.13: Speed responses for various proportional gains. Solid: $K = 0.6$, Dashed: $K = 1.2$, Dot-dashed: $K = 3.0$, and Dotted: $K = 6.0$

Figure 4.14 shows the reference current and the actual current in Phase 2 for $K = 6.0$ (We show only one phase current for clarity). The reader will notice two interesting features of the output response and phase current transient in Figure 4.14. First, when $K = 6.0$, the rotor speed exhibits a significant overshoot. Second, when the rotor speed is at steady-state, the actual phase current does not track the reference current. An intuitive explanation of these two phenomena in Figure 4.14 can be given as follows. The large reference current during transient ($0 \geq t \geq 0.01s$) causes the actual current to reach a value of 40A when the rotor speed reaches the reference speed of $60rad/s$. After that, because the commutation angles switch from Normal Mode to Brake Mode, the phase voltage is reversed and the phase current approaches zero rapidly. However, in the time it takes the current to drop from 40A to 0A, the energy stored in the circuit is released to the mechanical system generating a rotor speed increase and, thus, an overshoot.

On the other hand, the second phenomenon is caused by the fact that, when the rotor speed coincides with the reference speed, the set of turn-on and turn-off angles switches at very high frequency between Normal Mode and Brake Mode (see Figure 4.6), and hence the phase current cannot follow the reference current.

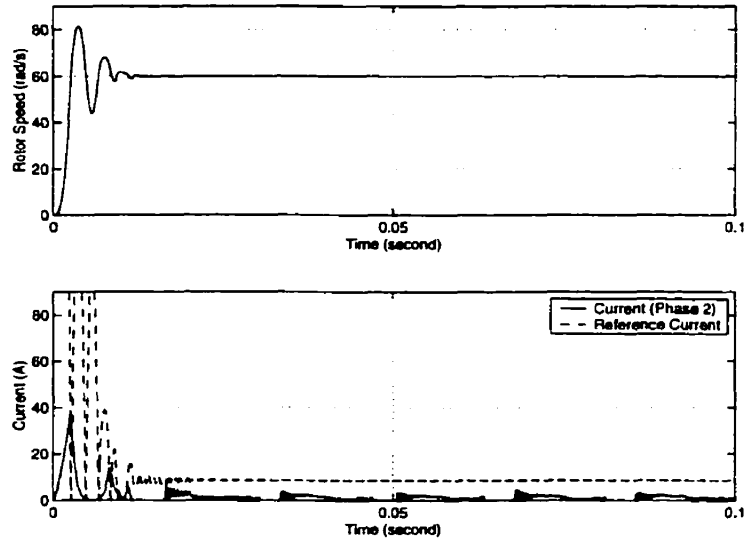

Figure 4.14: Speed response, phase current (Phase 2), and reference current signal for $K = 6.0$ and $Ti = 0.06$

Next, the variation of the integral time was tested. Figure 4.15 shows the step response for the same inertia and reference speed as in the simulation for various proportional gains ($J = 0.001kgm^2$, $\omega_{\text{ref}} = 60rad/s$). The proportional gain was kept constant at $K = 0.6$ while the integral time was varied from 1.5 to 0.0015. As one can see, the smaller the integral time, the faster the speed error approaches zero. However, too small integral time again causes undesired oscillations. When the integral time is further decreased, the integral gain increases to the point where it becomes the dominant component in PI controller. Figure 4.16 shows the reference current and the actual current in Phase 2 for $Ti = 0.0015$. In Figure 4.16, the similar features of the overshoots in output response and the dynamics of phase current can be explained as in the case of a large value of K in Figure 4.14. However, unlike the case of large proportional gain, the integrator in PI controller keeps the reference current high above the necessary current level even when the speed error converges to zero steady-state.

It is clear that one cannot indefinitely increase K and decrease T_i because there are two tradeoffs to decreasing the rising time of the speed response. One of the tradeoffs is that larger PI gains cause overshoot and oscillations. The other is that

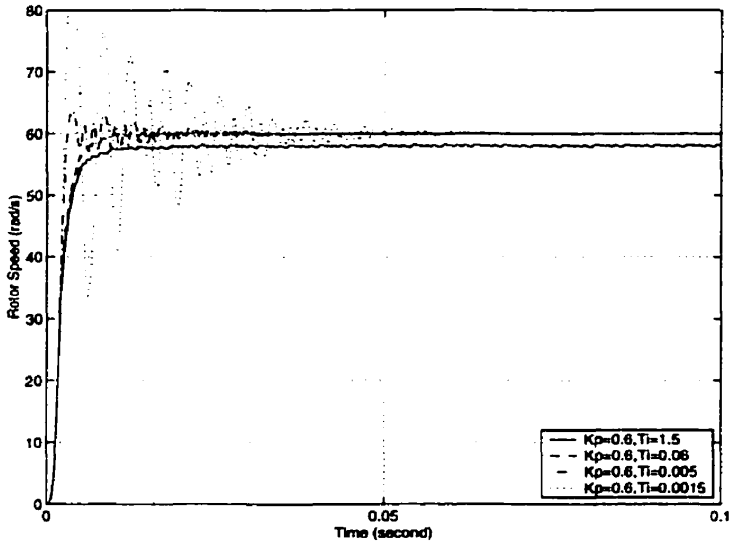

Figure 4.15: Speed responses for various integral time. Solid: $T_i = 1.5$, Dashed: $T_i = 0.06$, Dot-dashed: $T_i = 0.005$, and Dotted: $T_i = 0.0015$

having unnecessarily large reference current allows phase current to increase and hence allows energy-loss. Also, because the input to the mechanical subsystem is the phase current whose dynamic characteristics are limited by the magnitude of a DC voltage supply, the speed response also has a limit in its rate of change. Thus, the values of K and T_i can be tuned to optimize the performance of the SR machine for a given operating condition.

After trials with various combinations of PI gains for the operating speed, $\omega_{\text{ref}} = 60 rad/s$, a set of K and T_i was selected. Figure 4.17 shows the speed response and the phase current in Phase 2 with $K = 1.1$ and $T_i = 0.06$. Since the integral time is not as small as the one in Figure 4.16, the proportional gain is still the dominant part in the PI controller. Hence, the reference current comes down as the speed error decreases. At the steady state, nonzero phase current exists during the commutation periods for both Normal and Brake Modes in one rotor pole-pitch as explained earlier. The overall performance of the SR machine is clearly improved from the earlier trials. There is no overshoot in speed response, and the phase current stays low at the steady-state.

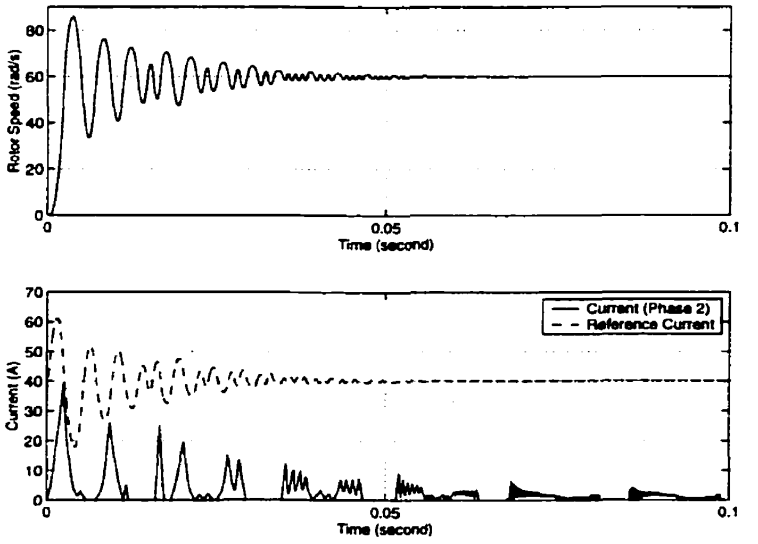

Figure 4.16: Speed response, phase current (Phase 2), and reference current signal for $K = 0.6$ and $T_i = 0.0015$

4.3.3 Performance under Various Operating Conditions

We now show the controller performance under different operating conditions. First, we present the performance of the traditional controller for different operating speeds. Figure 4.18 shows the speed responses for reference speeds $\omega_{\text{ref}} = 30$, 60, and $90 rad/s$ with the PI gains selected previously. The PI controller seems to work well without any overshoots nor oscillations. Notice that the initial rotor accelerations for the three different operating speeds are identical. This is because their phase current has not reached their initial reference current so that the phase voltage is applied to their phase windings for the entire time during this initial period. The current plots for $\omega_{\text{ref}} = 30$ and $90 rad/s$ are shown in Figure 4.19. Because it takes less time for the speed to reach $30 rad/s$ than $90 rad/s$, the reference current comes down earlier for the operating speed of $30 rad/s$. On the other hand, for the operating speed of $90 rad/s$, there is more time for the integrator to build up the reference current. Hence, the speed response deteriorates as the reference speed decreases.

Next, Figure 4.20 shows the simulation result with different machine inertia. The moment of inertia J is increased ten times to examine the speed response. As shown in the figure, the rising time of speed response increases as J increases. The effect of

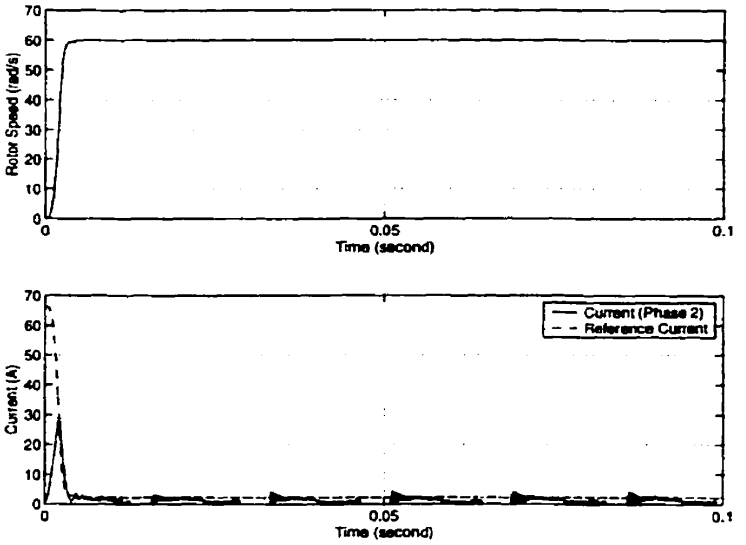

Figure 4.17: Speed response, phase current (Phase 2), and reference current signal for $K = 1.1$ and $T_i = 0.06$

increase in inertia is also shown by the mechanical dynamic equation in (3.25). The rotor acceleration $\dot{\omega}$ decreases as J increases.

Finally, the controller was tested in the presence of a load disturbance torque. Figure 4.21 shows the speed response of the SR machine with the addition of load torque $T_l = 10Nm$ at $t = 0.02s$ for the three different operating speeds. The traditional controller with the use of a PI controller demonstrates that the speed error eventually returns to zero. The integrator in PI control has the effect of keeping up the reference current to allow the actual current to produce enough torque to reject T_l as shown in Figure 4.22. Therefore, we conclude that the traditional controller with a PI control is robust against a load disturbance.

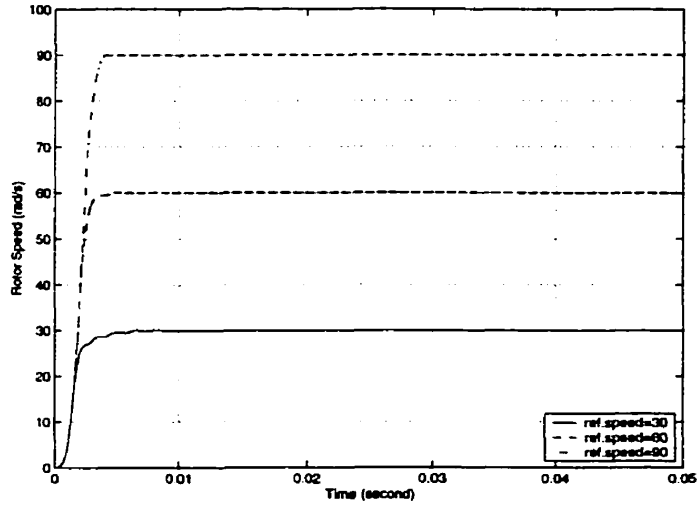

Figure 4.18: Speed responses for reference speeds $\omega_{\text{ref}} = 30$, 60, and $90 rad/s$. Solid: $\omega_{\text{ref}} = 30 rad/s$, Dashed: $\omega_{\text{ref}} = 60 rad/s$, and Dot-dashed: $\omega_{\text{ref}} = 90 rad/s$

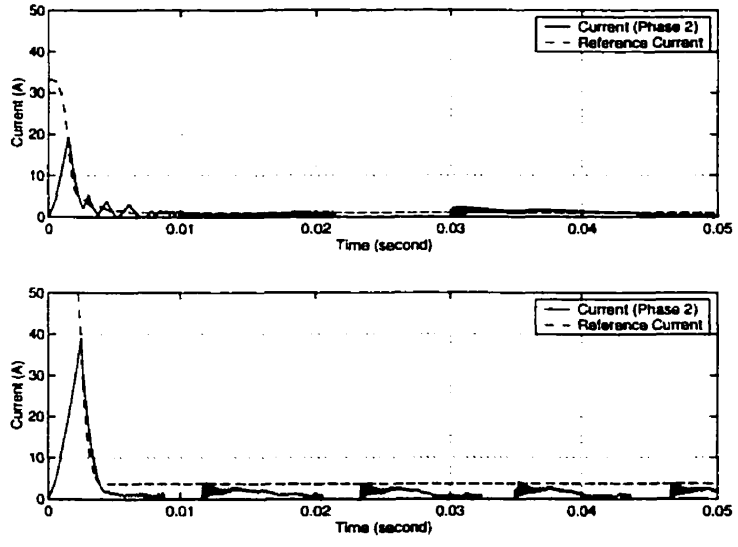

Figure 4.19: Phase current (Phase 2) and reference current signal for reference speeds $\omega_{\text{ref}} = 30$ and $90 rad/s$. Top: $\omega_{\text{ref}} = 30 rad/s$, Bottom: $\omega_{\text{ref}} = 90 rad/s$

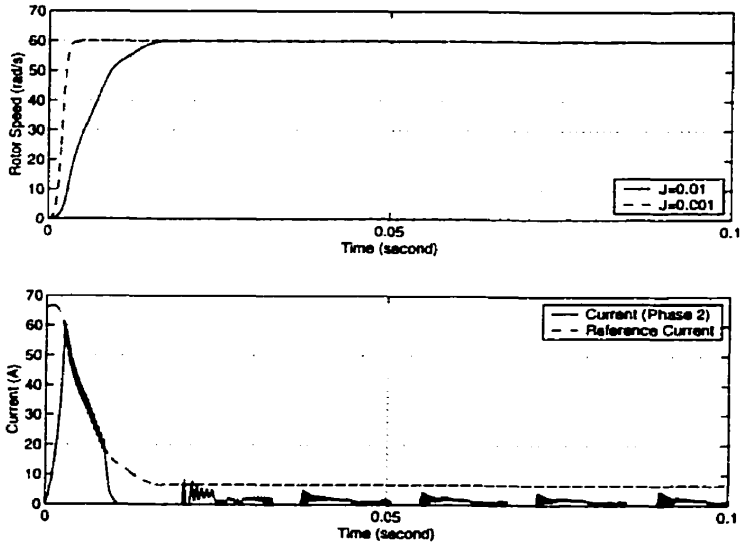

Figure 4.20: Speed responses, phase current (Phase 2), and reference current signal for $J = 0.01kgm^2$

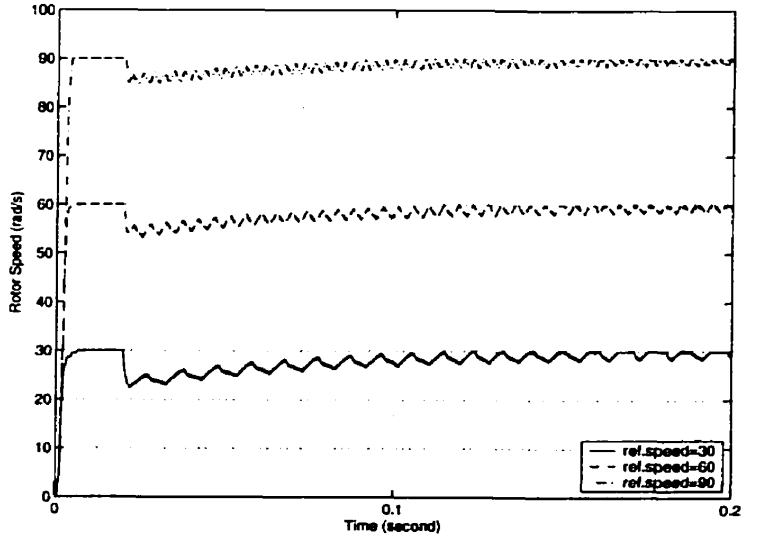

Figure 4.21: Speed responses with load disturbance $T_l = 10Nm$ added at $t = 0.02s$ (reference speeds $\omega_{\text{ref}} = 30$, 60, and $90rad/s$). Solid: $\omega_{\text{ref}} = 30rad/s$, Dashed: $\omega_{\text{ref}} = 60rad/s$, and Dot-dashed: $\omega_{\text{ref}} = 90rad/s$

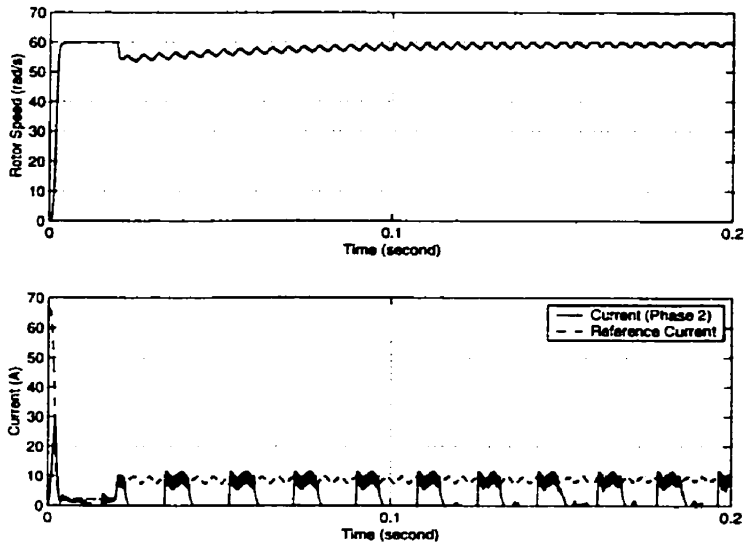

Figure 4.22: Speed response, phase current (Phase 2), and reference current signal for $\omega_{\text{ref}} = 60rad/s$, $T_l = 10Nm$

Chapter 5

Nonlinear Control

An SR machine has pronounced nonlinear characteristics in its torque production when it is operated in its saturated region. Although the PI controller designed in the previous chapter works quite well, it was designed solely by intuition about its characteristics and not by a proper control design method. Hence, its properties of stability and robustness are not guaranteed to hold under different operating conditions.

In order to solve this problem and cope with the significant degree of nonlinearity of the SR machine model, it is necessary to employ a nonlinear control design tool. Among several available techniques, the sliding mode control methodology (in short, SMC) appears to be quite appropriate since it is based on a high-speed switched feedback control and can be easily implemented with the switching circuit typical of an SR machine. An additional advantage of SMC is its robustness with respect to external disturbances and changes in system parameters (see, e.g., [19, 32]).

Recently, several researchers recognized the benefits of SMC and have developed SMC algorithms for SR machines (see, e.g., [2, 21, 35]). However, every algorithm developed with SMC appears either to ignore the magnetic saturation of the machine or to require knowledge of detailed magnetic characteristics of the machine and utilize extensive calculations. This research contributes with a new SMC algorithm that guarantees stability and requires simple calculations with less information on the magnetic characteristics of an SR machine. In the following, the basic theory of SMC is first described. Then, the design of the new SMC algorithm for an SR machine

is explained. Finally, simulation results with the SMC algorithm are presented and compared with the results from the previous chapter. General references for this chapter are found in [7, 19, 32].

5.1 Sliding Mode Control

SMC is an attractive feedback control technique that can guarantee the stability of nonlinear systems. The main idea of SMC is to employ a discontinuous control input to force the state trajectory of a nonlinear system to "slide" along a prespecified surface in the state space. This surface, called a *sliding manifold*, represents the properties of desired plant dynamics, such as stability to the origin and tracking.

The convergence of a state trajectory in SMC takes two main stages: the *reaching phase* and the *sliding phase*. An example of state trajectory in the three dimensional state space is shown in Figure 5.1. In the reaching phase, starting from an initial

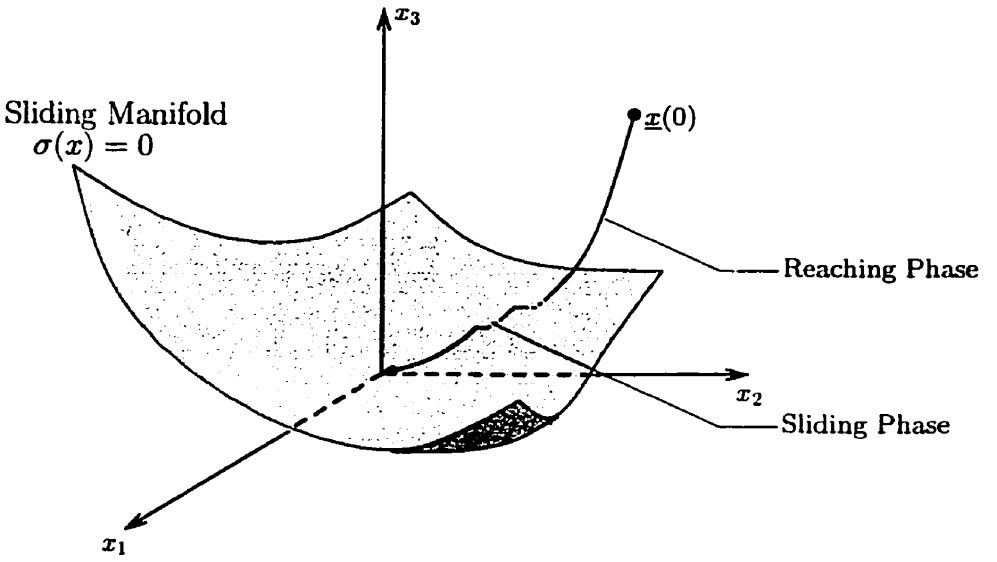

Figure 5.1: Two stages in the convergence of a state trajectory

condition $\underline{x}(0)$ away from the sliding manifold, the state is driven by feedback control towards the surface. The feedback control is designed such that the state trajectory is guaranteed to reach the sliding manifold in finite time. Once the trajectory reaches

the sliding manifold, the state is controlled to slide along the surface for all future time. Thus, the state trajectory is said to be in a sliding mode.

This behavior is achieved by utilizing a switched controller (hence, a discontinuous controller) whose switching is governed by the position of the state trajectory relative to the sliding manifold in such a way that the tangent (or the velocity vector) of the state trajectory always points towards the sliding manifold. For example, one can define a feedback control with one gain when the state trajectory is above the surface, and a different gain when the trajectory drops below the surface. By choosing proper gains under suitable conditions, the state trajectory reaches the sliding manifold in finite time and switches around the surface with infinite frequency as it slides along the surface for all future time. In practice, however, a switched controller has imperfections, such as delay and hysteresis, which limit switching to finite frequency. Thus, oscillation, called *chattering*, may occur in the state trajectory of a real system. In general, high frequency chattering may excite unmodeled dynamics in the system and even damage the actuators. When dealing with electrical machines, however, the actuator is a switching circuit and the effect of chattering is negligible.

The advantage of sliding mode control is its simplified design procedure. A full-order design problem is first decoupled into two lower-dimensional design problems. One subsystem is used in the design of a sliding manifold, and the other is used for designing a discontinuous control input. It is clear that designing two lower-dimensional controllers is easier than designing a higher-dimensional controller. Hence, each controller in SMC is designed relatively easily with useful nonlinear design tools, such as Lyapunov's method.

Moreover, SMC has an advantage in robust control. It is generally robust to external disturbances and changes in system parameters because the direction of a state trajectory depends only on the position of the state with respect to the sliding manifold. In particular, SMC theory shows that the robustness of a controller can be guaranteed if the *matching condition* is satisfied. The matching condition is a condition where bounded external disturbances enter into the system at the same point as the control input. By choosing control gains that reject such bounded disturbances, the state trajectory of a nonlinear system always reaches the sliding manifold in fi-

nite time and stays on the surface for all subsequent time. Thus, the desired plant dynamics can be achieved regardless of the external disturbances.

In the following, we describe the standard procedure of SMC design. We start by illustrating the decomposition of a system model. Then, the design of a sliding manifold and control inputs are explained.

5.1.1 Decomposition of System Model

Consider a system with a state model of the form

$$\dot{x} = f(x,t) + G(x,t)u, \tag{5.1}$$

where $x(t) \in \mathbb{R}^n$ is the state vector and $u(t) \in \mathbb{R}^m$ is the control vector; $f : \mathbb{R}^n \times \mathbb{R} \to \mathbb{R}^n$ and $G : \mathbb{R}^n \times \mathbb{R} \to \mathbb{R}^{n\times m}$ are assumed to be known and sufficiently smooth nonlinear functions defined for $(x,t) \in D_0 \times \mathbb{R}$, where D_0 is a domain that contains the origin. To be perfectly precise, (5.1) is shorthand for

$$\dot{x}(t) = f\big[x(t),t\big] + G\big[x(t),t\big]u(t).$$

Similar shortcuts will be made in the following.

In sliding mode control, the full-order system (5.1) is transformed into the cascade of two reduced-order subsystems, referred to as the *regular form*,

$$\dot{z}_1 = f_1(z_1, z_2, t), \tag{5.2}$$

$$\dot{z}_2 = f_2(z_1, z_2, t) + G_2(z_1, z_2, t)u, \tag{5.3}$$

where $z_1(t) \in \mathbb{R}^{n-m}$ and $z_2(t) \in \mathbb{R}^m$. This decomposition is done by applying a nonlinear transformation (see, e.g., [7, 19])

$$z = T(x,t) = \begin{bmatrix} T_1(x,t) \\ T_2(x,t) \end{bmatrix} = \begin{bmatrix} z_1 \\ z_2 \end{bmatrix}, \tag{5.4}$$

where

(i) For any $t \in \mathbb{R}^+$, $T(\cdot,t)$ is a *diffeomorphic* transformation on $\mathbb{R}^n$ (that is, an invertible transformation with a smooth inverse mapping, $T^{-1}(z,t) = x$), and

moreover $T(0,t) = 0$ for all t. In other words, $T(x,t)$ defines a family of diffeomorphisms parameterized by $t \in \mathbb{R}^+$.

(ii) $T_1 : \mathbb{R}^n \times \mathbb{R} \to \mathbb{R}^{n-m}$ and
$T_2 : \mathbb{R}^n \times \mathbb{R} \to \mathbb{R}^m$,

(iii) T has the property that

$$\left[\frac{\partial T}{\partial x}(T^{-1}(z,t))\right] G(T^{-1}(z,t)) = \begin{bmatrix} 0 \\ G_2(z,t) \end{bmatrix},$$

where $G_2(z,t)$ is a $m \times m$ matrix that is nonsingular for all $z \in TD_0$ and for all $t \in \mathbb{R}^+$.

Property (iii) is exactly what is required for (5.1) to be transformed to (5.2), (5.3) when $x(t)$ is transformed to $z(t)$ via $z = T(x,t)$. Notice that, in the regular form (5.2) and (5.3), the dynamics of the state vector of the lower subsystem, z_2, is directly controlled by the system input u, while the state vector of the upper subsystem, z_1, has no system input in its state equation. In the SMC design, (5.2) is used for designing a sliding manifold, and (5.3) is used for designing the system input.

5.1.2 Phase 1: Design of Sliding Manifold

In the first phase of the design of a sliding mode controller, we consider the upper subsystem,

$$\dot{z}_1 = f_1(z_1, z_2, t), \tag{5.5}$$

and view it as a system with state vector z_1 and control input z_2. With this in mind, we seek a smooth stabilizing state feedback control $z_2 = \phi(z_1, t)$ so that the origin of

$$\dot{z}_1 = f_1\left[z_1, \phi(z_1,t), t\right] \tag{5.6}$$

is asymptotically stable with a desired domain of attraction. Since this is a typical nonlinear stabilization problem, one can employ the Lyapunov approach and find $\phi(z_1,t)$ to achieve desired stability properties.

Once a stabilizing feedback law has been designed, the sliding manifold (the surface in $\mathbb{R}^n$) is defined by the equation

$$\sigma(z,t) = z_2 - \phi(z_1,t) = 0. \tag{5.7}$$

Here $\sigma : \mathbb{R}^n \to \mathbb{R}^m$, so $\sigma = [\sigma_1, \ldots, \sigma_m]^{\mathrm{T}}$; and the system, constrained on this sliding manifold, has the dimension $(n-m)$. It is clear that if one can guarantee that the state trajectory stays on the sliding manifold for all future time, then the condition $\sigma(z,t) = 0$, i.e., $z_2 = \phi(z_1,t)$, is maintained for all subsequent time. By construction, when $z_2 = \phi(z_1,t)$, the state vector of the upper subsystem, z_1, approaches the origin asymptotically. (Note that, when dealing with general nonautonomous system, $\phi(0,t)$ may not be equal to zero, and hence in steady-state $z_2(t)$ may be a time-varying function which does not approach the origin.)

5.1.3 Phase 2: Design of Control Input

In the previous subsection, we have seen that if $z_2(t) = \phi\big(z_1(t),t\big)$ for all $t \geq 0$, then z_1 approaches zero asymptotically. In the second phase of the sliding mode control design, the system input $u(t)$ is designed so that the state vector $z_2(t)$ of the lower subsystem

$$\dot{z}_2 = f_2(z,t) + G_2(z,t)u \tag{5.8}$$

reaches $\phi(z_1,t)$ in finite time, and the condition $\sigma(z,t) = 0$ is maintained for all subsequent time. In other words, starting from an initial condition away from the sliding manifold, the system input $u(t)$ drives the state trajectory onto the surface in finite time and keeps it there.

Such control input, $u = [u_1, \ldots, u_m]^{\mathrm{T}}$, is a switching control signal of the form

$$u_j(t) = \begin{cases} u_j^+(t), & \text{when } s_j(t) > 0 \\ u_j^-(t), & \text{when } s_j(t) < 0, \end{cases} \tag{5.9}$$

where s_j is the output signal of the function $\sigma_j(z,t)$, i.e., $s_j(t) = \sigma_j\big(z(t),t\big)$. Equation (5.9) indicates that the control input changes its value depending on the position of

the state with respect to the sliding manifold. The control is undefined on the surface, while the control values, $u_j^{\pm}$, are selected so that, off the surface, the tangent vector of the state trajectory always points towards the sliding manifold. Thus, the state is driven to and maintained on $\sigma(z,t) = 0$. Figure 5.2 shows the block diagram of the overall feedback control system with SMC.

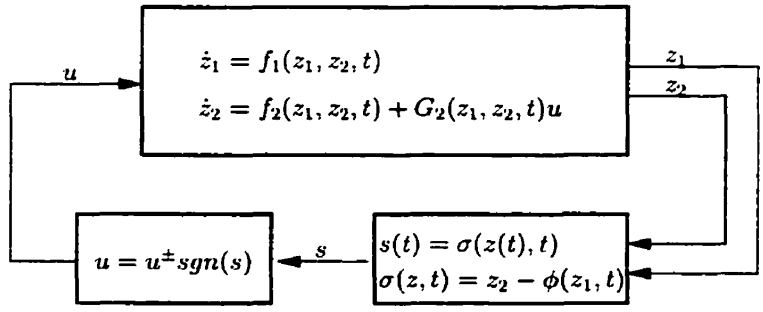

Figure 5.2: Block diagram of the overall sliding mode feedback control system

As mentioned earlier, controllers of the form (5.9) result in discontinuous closed-loop systems. Since SMC produces system dynamics with discontinuous right-hand sides due to the switching action of the controller, one must address existence and uniqueness of the solution of differential equations. A comprehensive theory of differential equations with discontinuous right-hand sides was developed by the Russian mathematician Filippov [11]. Utkin used this theory to develop the so-called equivalent control method which, for systems that are linear in the control inputs, provides a useful framework to study the motion of the system on the sliding manifold. The reader is referred to [32] for more details in this topic.

5.2 SMC Design for SR Machine

In this section, a speed tracking controller is designed with SMC for the regular 8/6 SR machine. First, the system model must be transformed into the regular form.

Recall, from Chapter 3, the system model of the SR machine,

$$\begin{aligned}
\dot{\theta} &= \omega, \\
\dot{\omega} &= \frac{1}{J}\left[\sum_{p=1}^{4} T_p(\theta_p, i_p) - B\omega - T_l\right], \\
\frac{\mathrm{d}i_p}{\mathrm{d}t} &= \left[\frac{\partial \Psi_p(\theta_p, i_p)}{\partial i_p}\right]^{-1}\left[v_p - Ri_p - \frac{\partial \Psi_p(\theta_p, i_p)}{\partial \theta_p}\omega\right], \quad p = 1, \ldots, 4,
\end{aligned} \tag{5.10}$$

where T_p, $\frac{\partial \Psi_p}{\partial i_p}$, and $\frac{\partial \Psi_p}{\partial \theta_p}$ are calculated from the flux-linkage Fourier series, $\Psi_p(\theta_p, i_p)$.

Since this research focuses on speed tracking control of the SR machine, we are interested in the dynamics of speed error e, defined as

$$e(t) = \omega(t) - \omega_{\mathrm{ref}}, \tag{5.11}$$

where ω_{ref} is the desired speed and is assumed to be a known constant. In speed tracking control, although the rotor position θ is an important factor in the determination of the phase angle θ_p, we are not interested in controlling it, and hence it is treated as a measured variable. Thus, $\theta_p(t)$ is a measured, hence known, function of t.

A new system model for speed tracking control of the SR machine is defined by substituting $\omega = e + \omega_{\mathrm{ref}}$ into (5.10),

$$\begin{aligned}
\dot{e} &= \frac{1}{J}\left[\sum_{p=1}^{4} T_p(\theta_p, i_p) - Be - B\omega_{\mathrm{ref}}\right], \\
\frac{\mathrm{d}i_p}{\mathrm{d}t} &= \left[\frac{\partial \Psi_p(\theta_p, i_p)}{\partial i_p}\right]^{-1}\left[v_p - Ri_p - \frac{\partial \Psi_p(\theta_p, i_p)}{\partial \theta_p}(e + \omega_{\mathrm{ref}})\right], \quad p = 1, \ldots, 4,
\end{aligned} \tag{5.12}$$

where the external disturbance T_l is neglected for designing the basis of SMC. The system input of the model is the switched phase voltage v_p, which varies among three values, $\pm V_{\mathrm{dc}}$ and 0. Rearranging (5.12) gives

$$\dot{e} = \frac{1}{J}\left[\sum_{p=1}^{4} T_p(\theta_p, i_p) - Be - B\omega_{\mathrm{ref}}\right], \tag{5.13}$$

$$\frac{\mathrm{d}i_p}{\mathrm{d}t} = \left[\frac{\partial \Psi_p(\theta_p, i_p)}{\partial i_p}\right]^{-1}\left[-Ri_p - \frac{\partial \Psi_p(\theta_p, i_p)}{\partial \theta_p}(e + \omega_{\mathrm{ref}})\right] + \left[\frac{\partial \Psi_p(\theta_p, i_p)}{\partial i_p}\right]^{-1} v_p, \quad p = 1, \ldots, 4. \tag{5.14}$$

Notice that the new system model is already in the regular form (5.2), (5.3) in which the dynamics of phase current i_p is directly controlled by the system input v_p, while the dynamics of speed error e is controlled by the state variable i_p. Hence, (5.13) is used in the design of a sliding manifold, and (5.14) is used for designing the discontinuous control input. The dependence of the right-hand sides of (5.13), (5.14) on t is through the function $\theta_p(t)$.

5.2.1 Phase 1: Design of Sliding Manifold

In order to design a sliding manifold for speed tracking control of the SR machine, the phase current i_p in (5.13) is viewed as the control input in the subsystem. The objective of this design phase is to find a stabilizing feedback control, $i_p = \phi(e,t)$, so that the origin of

$$\dot{e} = \frac{1}{J}\left\{\sum_{p=1}^{4} T_p[\theta_p, \phi(e,t)] - B\omega_{\text{ref}} - Be\right\} \tag{5.15}$$

is asymptotically stable. In the following, we first analyze the properties of the phase torque T_p with respect to the phase angle θ_p and the phase current i_p. Then, a simple feedback control $\phi(e,t)$ is derived without the full knowledge of the magnetic characteristics of the SR machine.

Intuitively, in order to reduce the speed error of the SR machine, phase current is applied to produce phase torque in such a direction that acceleration or braking reduces the magnitude of speed error. Figure 5.3 shows the plot of instantaneous phase torque over one rotor pole-pitch for various current levels. In the figure, θ_{on} and θ_{off} are the turn-on and turn-off angles in acceleration, respectively, and $\theta'_{\text{on}} = -\theta_{\text{off}}$ and $\theta'_{\text{off}} = -\theta_{\text{on}}$ are for braking. The commutation intervals are defined as $\mathcal{I} = [\theta_{\text{on}}, \theta_{\text{off}}]$ and $\mathcal{I}' = [\theta'_{\text{on}}, \theta'_{\text{off}}]$. As described in Chapter 3, the sign of the instantaneous phase torque depends only on the phase angle θ_p. Applying the phase current before the aligned position is acceleration, and after the aligned position is braking. The following analysis on the phase torque focuses only on the case of acceleration since braking is analogous.

First, we begin the analysis by introducing the class of K_∞ functions.

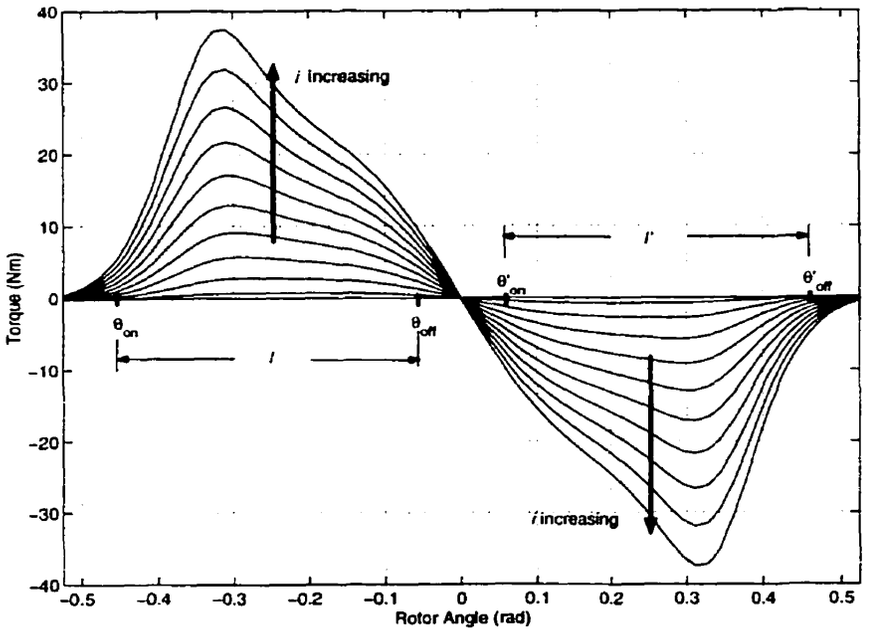

Figure 5.3: Instantaneous torque over one rotor pole-pitch for various current levels

Definition 1 (see [19]) *A continuous function* $\alpha : [0, \infty) \to [0, \infty)$ *is said to belong to class* K_∞ *if* $\alpha(0) = 0$, *it is strictly increasing, and* $\alpha(r) \to \infty$ *as* $r \to \infty$.

Notice in Figure 5.3 that, in the acceleration interval, the phase torque is a strictly increasing function of phase current i_p. In addition, phase torque is zero when i_p is zero. Since the torque plot in Figure 5.3 is a typical shape of phase torque in SR machines, we can make the following assumption about the phase torque:

Assumption 1 *For each* $\theta_p \in \mathcal{I}$, $p = 1, \ldots, 4$, $T_p(\theta_p, i_p)$ *is a class* K_∞ *function of* i_p.

Since this research focuses only on the current chopping mode of the SR machine, θ_{on} and θ_{off} are fixed as in the traditional control design. Notice that θ_{on} and θ_{off} are identical for all the phases and are periodic in the rotor position. Hence, the interval $\mathcal{I}$ is also identical for all the phases and periodic in the rotor position as shown in Figure 5.4.

Inside the interval $\mathcal{I}$, since the phase torque T_p is a smooth function of $\theta_p \in \mathcal{I}$ and

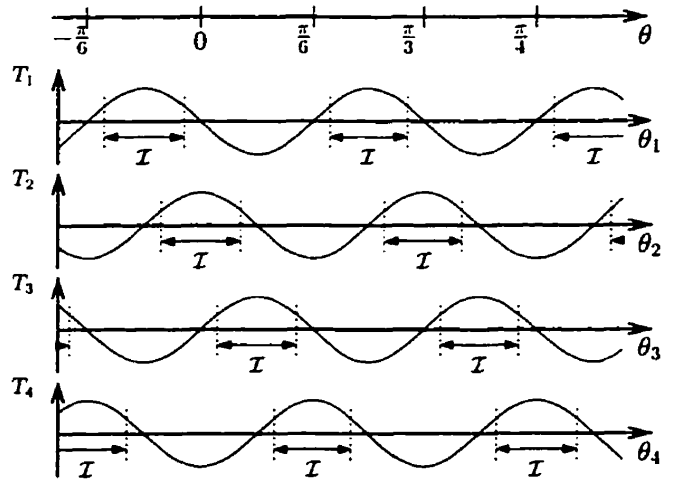

Figure 5.4: Periodical commutation intervals for four phases

always positive when $i_p \neq 0$, there exists a positive lower bound to the phase torque at each current level. Thus, the following assumption can be made:

Assumption 2 *There exists a class K_∞ function h such that*

$$T_p(\theta_p, i_p) \geq h(i_p), \qquad \forall \theta_p \in \mathcal{I}.$$

Notice that because the torque equation is identical for all the phases, the lower bound function h can be also found identical for all the phases. Figure 5.5 shows the lower bounds of the phase torque for various current levels in one rotor pole-pitch.

As explained in Chapters 3 and 4, θ_{on} and θ_{off} are chosen so that the torque productions of adjacent phases always overlap with each other. That is, at any rotor position $\theta \in \mathbb{R}$, at least one θ_p is in the interval $\mathcal{I}$ as shown in Figure 5.4. Therefore, by exciting only the phases whose phase angles $\theta_p \in \mathcal{I}$ and keeping the rest unenergized, there is always at least one energized phase p^* such that $i_{p^*} \neq 0$ and

$$\sum_{p=1}^{4} T_p(\theta_p, i_p) \geq T_{p^*}(\theta_{p^*}, i_{p^*}) \geq h(i_{p^*}). \tag{5.16}$$

Since the lower bound function $h(i_p)$ is a class K_∞ function, it is invertible. If we have the mathematical expression of $h(i_p)$, by setting it equal to a desired minimum torque,

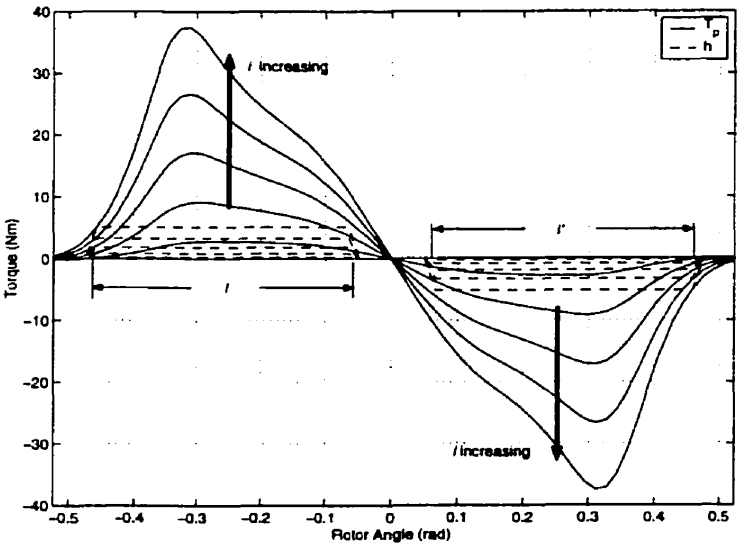

Figure 5.5: Instantaneous torque T_p and lower bound function h over one rotor pole-pitch for various current levels

we can solve the equation for the phase current i_p, which guarantees to produce at least this minimum torque at any rotor position.

Note that the above assumptions on T_p are not restrictive and are quite easy to verify in practice. In particular, it is easier to find $h(i_p)$ than to find an approximation of T_p. By examining the pattern of the torque plot in Figure 5.5, it is clear that $T_p(\theta_{\text{on}}, i_p)$ is the lowest before the peak, and $T_p(\theta_{\text{off}}, i_p)$ is the lowest after the peak at any current levels. These are reasonable candidates for the lower bound since the torque plot in Figure 5.5 is a typical shape in SR machines. Figure 5.6 shows the plots of $T_p(\theta_{\text{on}}, i_p)$ and $T_p(\theta_{\text{off}}, i_p)$ with respect to i_p. In this particular SR machine, $T_p(\theta_{\text{on}}, i_p)$ is always less than $T_p(\theta_{\text{off}}, i_p)$. Hence, the mathematical expression of $h(i_p)$ has been approximated to the Fourier series $T_p(\theta_{\text{on}}, i_p)$ by curve-fitting a second-order polynomial by the least square method in Matlab. The resulting equation is as follows:

$$h(i_p) = 0.0135 i_p^2 + 0.0437 i_p.$$

Figure 5.6 also shows the plot of $h(i_p)$ with respect to i_p. Note that although $h(i_p)$ in Figure 5.6 is not the exact match to $T_p(\theta_{\text{on}}, i_p)$, compared to the plots of $T_p(\theta_{\text{off}}, i_p)$ and $T_p(-0.3, i_p)$ (the peak of torque waveform), $h(i_p)$ is a very conservative choice for

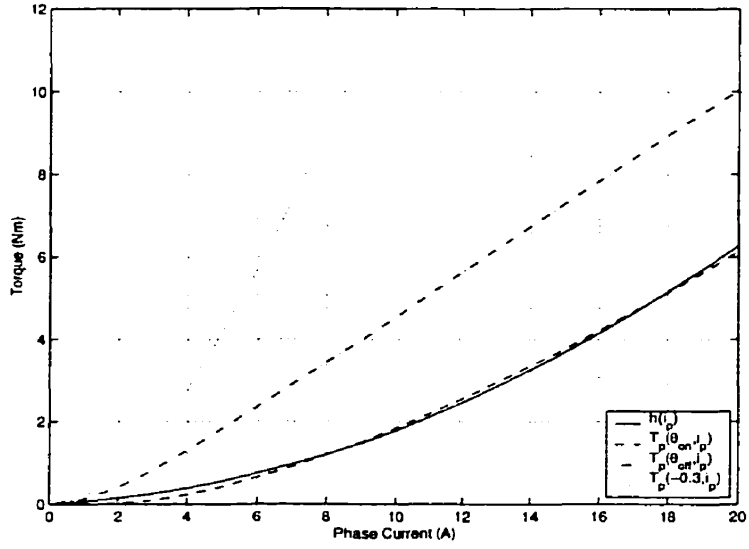

Figure 5.6: Torque T_p with respect to phase current i_p at $\theta_p = \theta_{\text{on}}$, θ_{off}, and $-0.3rad$ (peak) and the approximation of the lower bound h

the lower bound. Thus, the difference between $h(i_p)$ and $T_p(\theta_{\text{on}}, i_p)$ is negligible in practice. For theoretical study, we assume that $h(i_p) = T_p(\theta_{\text{on}}, i_p)$. With this $h(i_p)$, in the following, we define the feedback control ϕ and prove its stability properties.

Controller Definition 1 *The state feedback control laws for speed tracking in acceleration and braking (forward motoring operation) are defined as follows:*
***Acceleration**: For $\omega_{ref} > 0$ and $\omega_{ref} > \omega$, i.e., $e < 0$,*

$$i_p = \phi(\theta_p, e) = \begin{cases} h^{-1}(B\omega_{ref} - C_1 e), & \text{for } \theta_p \in \mathcal{I} \\ 0, & \text{otherwise,} \end{cases} \tag{5.17}$$

where C_1 is any constant such that $C_1 > -B$.
***Braking**: For $\omega > \omega_{ref} > 0$, i.e., $e > 0$,*

$$i_p = \phi(\theta_p, e) = \begin{cases} h^{-1}(C_2 e), & \text{for } \theta_p \in \mathcal{I}' \\ 0, & \text{otherwise.} \end{cases} \tag{5.18}$$

where C_2 is any positive constant.

The block diagram of the upper subsystem (5.15) with the state feedback control (5.17), (5.18) is shown in Figure 5.7. The plant block is described with the second-

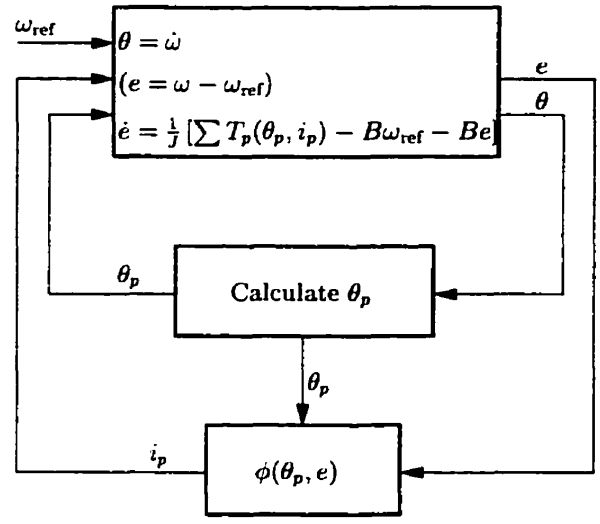

Figure 5.7: Block diagram of the upper subsystem with the state feedback control $i_p = \phi(\theta_p, e)$

order equation. The rotor position $\theta(t)$ is a measured variable as explained earlier. The control block takes the state e and the calculated phase angle θ_p for $p = 1, \ldots, 4$. The control lows (5.17), (5.18) determine the control signal i_p according to the sign of e and $\theta_p \in \mathcal{I}$. Then, i_p is applied to the plant.

Theorem 1 *Consider the nonlinear system in Figure 5.7. For every $\theta(0)$, the origin $e = 0$ is uniformly asymptotically stable.*

For the minimal system with only the rotational friction, the stability of the system with the proposed feedback control $\phi(\theta_p, e)$ can be proven by the following Lyapunov stability theorem for nonautonomous systems.

Lemma 1 (Theorem 3.8 [19]) *Let $z_1 = 0$ be an equilibrium point for (5.6) and $D_1 \subset \mathbb{R}^{n-m}$ be a domain containing $z_1 = 0$. Let $V : D_1 \times [0, \infty) \to \mathbb{R}$ be a continuously differentiable function such that*

$$W_1(z_1) \leq V(z_1, t) \leq W_2(z_1) \tag{5.19}$$

$$\frac{\partial V}{\partial t} + \frac{\partial V}{\partial z_1} f_1(z_1, t) \leq -W_3(z_1) \tag{5.20}$$

$\forall t \geq 0$, $\forall z_1 \in D_1$ where $W_1(x)$, $W_2(x)$, and $W_3(x)$ are continuous positive-definite functions on D_1. Then, $z_1 = 0$ is uniformly asymptotically stable.

Proof of Theorem 1: The Lyapunov function candidate is chosen as

$$V = \frac{1}{2}e^2. \tag{5.21}$$

Then, the time derivative of V is given by $\dot{V} = e\dot{e}$. From (5.13), we have the derivative of e with the control input ϕ as

$$\begin{aligned} \dot{e} &= \frac{1}{J}\left[\sum_{p=1}^{4} T_p(\theta_p, i_p) - B\omega_{\text{ref}} - Be\right] \\ i_p &= \phi(\theta_p, e), \quad p = 1, \ldots, 4. \end{aligned} \tag{5.22}$$

From (5.16), we know that, at any rotor position in acceleration, the total instantaneous torque is guaranteed to be greater than the function $h(i_{p^*})$, where p^* denotes an active phase ($\theta_{p^*} \in \mathcal{I}$). Hence, at any rotor position, we have inequality

$$\dot{e} \geq \frac{1}{J}\left[h(i_{p^*}) - B\omega_{\text{ref}} - Be\right]. \tag{5.23}$$

For $\theta_{p^*} \in \mathcal{I}$, by Controller Definition 1, $i_{p^*} = h^{-1}(B\omega_{\text{ref}} - C_1 e)$. Therefore, the inequality (5.23) becomes

$$\begin{aligned} \dot{e} &\geq \frac{1}{J}(B\omega_{\text{ref}} - C_1 e - B\omega_{\text{ref}} - Be) \\ &\geq -\frac{1}{J}(B + C_1)e. \end{aligned} \tag{5.24}$$

Since $B + C_1 > 0$ and $e < 0$ in acceleration,

$$\dot{e} \geq -\frac{1}{J}(B + C_1)e > 0. \tag{5.25}$$

Thus, we have

$$\begin{aligned} \dot{V} &= e\dot{e} \\ &\leq -\frac{1}{J}(B + C_1)e^2 \\ &< 0. \end{aligned} \tag{5.26}$$

The assumptions of Lemma 1 are satisfied with $W_1(e) = W_2(e) = V(e)$ and $W_3(e) = \frac{1}{J}(B + C_1)e$ in acceleration.

For braking, because its phase torque is a mirror image of the acceleration torque about the aligned position with only the opposite sign, we have a negative upper bound function, $h'(i_p) = -h(i_p)$, where $h'(i_p) = T_p(\theta'_{\text{off}}, i_p)$. For $e > 0$, at any rotor position, it is guaranteed that there is always an excited phase p^* ($\theta_{p^*} \in \mathcal{I}'$) such that $i_{p^*} \neq 0$ and

$$\sum_{p=1}^{4} T_p(\theta_p, i_p) \leq T_{p^*}(\theta_{p^*}, i_{p^*}) \leq h'(i_{p^*}). \tag{5.27}$$

Hence, we have

$$\sum_{p=1}^{4} T_p(\theta_p, i_p) \leq -h(i_{p^*}). \tag{5.28}$$

By substituting this inequality into (5.22),

$$\begin{aligned} \dot{e} &\leq \frac{1}{J}\big[-h(i_{p^*}) - B\omega_{\text{ref}} - Be\big] \\ &\leq \frac{1}{J}(-C_2 e - B\omega_{\text{ref}} - Be) \\ &\leq -\frac{1}{J}(B + C_2)e. \end{aligned} \tag{5.29}$$

Thus, we obtain

$$\begin{aligned} \dot{V} &= e\dot{e} \\ &\leq -\frac{1}{J}(B + C_2)e^2 \\ &< 0. \end{aligned} \tag{5.30}$$

The assumptions of Lemma 1 are also satisfied for braking with $W_1(e) = W_2(e) = V(e)$ and $W_3(e) = \frac{1}{J}(B + C_2)e$. □

The resulting sliding manifold is defined as

$$\sigma_p(\theta_p, e, i_p) = i_p - \phi(\theta_p, e) = 0, \quad p = 1, \ldots, 4. \tag{5.31}$$

Note, as a concluding remark, that $\phi(\theta_p, e)$ is a piecewise continuous function of θ_p (hence, not a continuous function).

5.2.2 Phase 2: Design of Control Input

In the previous subsection, we have seen that if $i_p(t) = \phi\big(\theta_p(t), e(t)\big)$ for all $t \geq 0$, then e approaches zero asymptotically. Here, the phase current i_p is a state variable. Recall the lower subsystem in the regular form,

$$\frac{\mathrm{d}i_p}{\mathrm{d}t} = \left[\frac{\partial \Psi_p(\theta_p, i_p)}{\partial i_p}\right]^{-1} \left[v_p - Ri_p - \frac{\partial \Psi_p(\theta_p, i_p)}{\partial \theta_p}(e + \omega_{\text{ref}})\right], \quad p = 1, \ldots, 4, \tag{5.32}$$

where v_p is the system input. The objective of this design phase is to find a control input v_p so that i_p follows the reference current signal

$$i_{\text{ref},p}(t) = \phi\big(\theta_p(t), e(t)\big). \tag{5.33}$$

Specifically, we want to guarantee that $\sigma_p(\theta_p, e, i_p)$ reaches zero in finite time, and the condition $\sigma_p(\theta_p, e, i_p) = 0$ is maintained for all subsequent time. However, because $\phi(\theta_p, e)$ is a piecewise continuous function of $\theta_p(t)$, $i_{\text{ref},p}(t)$ is not continuous in t. Hence, the condition $\sigma_p(\theta_p, e, i_p) = 0$ cannot be guaranteed to hold for all future time. Later in this chapter, we will show that the stability of the speed error can still be guaranteed as long as the phase current has fast dynamics and torque productions of adjacent phases still overlap with each other.

Stability of Sliding Manifold over One Commutation Interval

We will start our analysis by investigating the reaching condition for i_p during one commutation interval, where $\theta_p \in \mathcal{I}$ in acceleration and $\theta_p \in \mathcal{I}'$ in braking. Since there is no turn-off during this period, ϕ is a function only of the speed error, that is,

$$\phi_p(e) = \begin{cases} h^{-1}(B\omega_{\text{ref}} - C_1 e), & \text{for } e < 0 \text{ (Acceleration)}, \\ h^{-1}(C_2 e), & \text{for } e > 0 \text{ (Braking)}. \end{cases}$$

The subscript p in ϕ_p indicates that $\phi(e)$ is employed on each commutation phase p. Since the speed error is a smooth function of t and h^{-1} is continuous with respect to e, the reference current signal $i_{\text{ref},p}(t) = \phi_p\big(e(t)\big)$ is now a smooth function of t.

As described in the previous section, the control input of SMC is based on a switching control law. The structure of a switched control input in the SR machine is

defined by the electrical circuit described in Chapters 2 and 3, where the magnitude of voltage supply stays constant while its sign switches positive and negative. When the reference current is turned off, negative voltage is applied to the phase windings to force the phase current to zero, and then the phase voltage is turned off until the next commutation. The following discussion introduces the structure of a switched control input in the SR machine and describes the formulation of a control gain based on the Lyapunov approach.

Controller Definition 2 *The switching control law for current chopping is defined as*

$$v_p = -V_{dc} sgn(s_p), \tag{5.34}$$

where the magnitude of DC voltage supply, V_{dc}, is the control gain, $sgn(\cdot)$ is the signum function, and s_p is the output signal of the function $\sigma_p(e, i_p) = i_p - \phi_p(e)$, i.e., $s_p(t) = i_p(t) - i_{ref,p}(t)$.

The block diagram of the overall SMC system with function ϕ and the switched control (5.34) is shown in Figure 5.8. The plant block is described with the sixth-

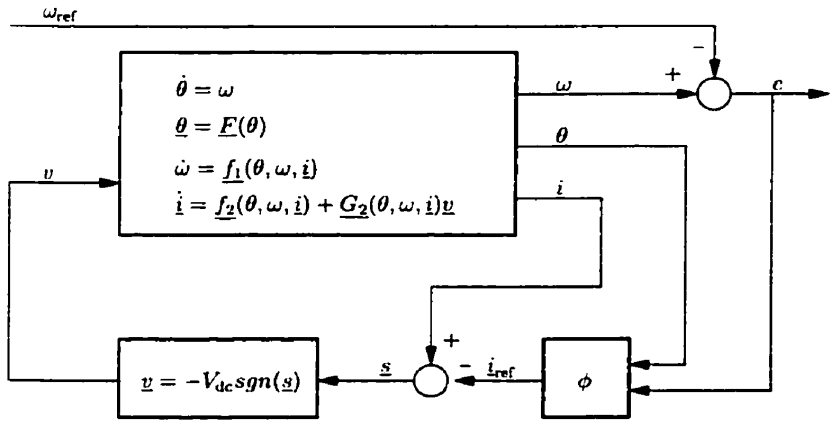

Figure 5.8: Block diagram of overall SMC system with the switched control low v_p

order equations, i.e., the states are $[\theta, \omega, i_1, \ldots, i_4]^T$. Again, θ is treated as a measured variable. The phase angles, $\underline{\theta} \triangleq [\theta_1, \ldots, \theta_4]^T$, are calculated from θ by function $\underline{F}$.

The speed error $e = \omega - \omega_{\text{ref}}$ and the phase angles $\underline{\theta}$ are fedback to the function ϕ. The reference current signal i_{ref} is found by the function ϕ and is subtracted from the actual phase currents, $\underline{i} \triangleq [i_1, \ldots, i_4]^T$ to obtain the signals $\underline{s}$. The signals $\underline{s}$ describe the position of (e, i_p) with respect to the sliding manifold $\sigma = 0$. The switched controller takes $\underline{s}$ as input and finds voltage signals $\underline{v} \triangleq [v_1, \ldots, v_4]^T$.

Since the dynamic equation of phase current i_p is identical for all phases and i_p is controlled independently by its corresponding phase voltage v_p, it is sufficient to design v_p to stabilize the associated sliding manifold $\sigma_p(e, i_p) = 0$. Hence, in order to study the stability of the sliding manifold in the reaching phase, we will need to consider the second-order subsystem with states (e, i_p), for $p = 1, \ldots, 4$.

Theorem 2 *Assume that $\forall V_{dc}$, there exist compact subsets $\Omega_c^0, \Omega_c \subset \mathbb{R}^5$ such that for any $\big(e(0), \underline{i}(0)\big) \in \Omega_c^0 \subset \Omega_c$, $\big(e(t), \underline{i}(t)\big) \in \Omega_c$, $\forall t \geq 0$. Then, for any $\Delta t > 0$, there exists a large enough V_{dc} such that $\big(e(t), i_p(t)\big)$ converges to the sliding manifold in a finite reaching time, $t_R < \Delta t$, for $p = 1, \ldots, 4$.*

Note that one of the objectives in this section should be to actually prove that $\big(e(t), \underline{i}(t)\big) \in \Omega_c$ $\forall t \geq 0$. However, due to the coupling of the dynamics associated to the tracking error e and the phase currents $\underline{i}$, a standard sliding mode analysis does not allow us to prove the existence of the set Ω_c and determine an estimate of its size. It is interesting to note that several authors in the literature seem to neglect (or not be aware of) this theoretical problem. We therefore proceed to the proof of Theorem 2 with the assumption which, in our opinion, is based on physical sense, that is, for any finite voltage V_{dc}, the rotor speed remains bounded. This is due to the fact that V_{dc} controls only the rate of change of phase currents. Since phase currents cannot exceed the reference current signals, the dynamics of the rotor speed is limited by the reference current signal. Hence, V_{dc} does not directly control the rotor speed, and $\big(e(t), \underline{i}(t)\big)$ stay bounded for all future time.

The proof of Theorem 2 also indirectly assumes that $\theta_p(t) \in \mathcal{I}$ for all $t \in (0, \Delta t]$. This can be shown to hold true by the use of the assumption $\big(e(t), \underline{i}(t)\big) \in \Omega_c$, $\forall t \geq 0$ and the existence of a lower bound to Δt as follows. First, let $\Delta\mathcal{I}$ to be the duration

of commutation interval $\mathcal{I}$. That is, at some rotor speed ω,

$$\Delta\mathcal{I} = \frac{\text{length}(\mathcal{I})}{\omega}. \tag{5.35}$$

From the assumption that e is in the compact set Ω_c, e is bounded. This implies that the rotor speed is bounded as $|\omega| \leq |\omega_{\text{ref}}| + |e| < \infty$. Hence, $\Delta\mathcal{I}$ is bounded as

$$\Delta\mathcal{I} \geq \frac{\text{length}(\mathcal{I})}{|\omega_{\text{ref}}| + |e|} > 0. \tag{5.36}$$

Since $\Delta\mathcal{I}$ has a lower bound, we can choose $\Delta t = \Delta\mathcal{I}$. Thus, $\theta_p(t) \in \mathcal{I}$ for $0 \geq t \geq \Delta t$. In the following, the reaching condition of the sliding manifold is examined in terms of the control gain V_{dc} in the Lyapunov approach. Then, the finite time convergence $\sigma_p \to 0$ is shown by the use of the comparison lemma in [19].

Proof of Theorem 2: As mentioned earlier, in order to study the stability of the sliding manifold $\sigma_p(e, i_p) = 0$, we start by considering the dynamics of the second-order subsystem,

$$\dot{e} = \frac{1}{J}\left[\sum_{p=1}^{4} T_p(\theta_p, i_p) - Be - B\omega_{\text{ref}}\right], \tag{5.37}$$

$$\frac{\mathrm{d}i_p}{\mathrm{d}t} = \left[\frac{\partial\Psi_p(\theta_p, i_p)}{\partial i_p}\right]^{-1}\left[v_p - Ri_p - \frac{\partial\Psi_p(\theta_p, i_p)}{\partial\theta_p}(e + \omega_{\text{ref}})\right]. \tag{5.38}$$

(Note that the dynamics of the above subsystem for (e, i_p) still depends on all phase currents $\underline{i}$.) The Lyapunov function candidate for this subsystem is chosen as

$$V_p = \frac{1}{2}\sigma_p^2. \tag{5.39}$$

The time derivative of V_p is given by $\dot{V}_p = \sigma_p\dot{\sigma}_p$. Taking the derivative of $\sigma_p = i_p - \phi_p(e)$, we have

$$\dot{\sigma}_p = \frac{\mathrm{d}i_p}{\mathrm{d}t} - \frac{\partial\phi_p}{\partial e}\dot{e}. \tag{5.40}$$

By substituting (5.38) into (5.40),

$$\dot{\sigma}_p = \left(\frac{\partial\Psi_p}{\partial i_p}\right)^{-1}\left[v_p - Ri_p - \frac{\partial\Psi_p}{\partial\theta_p}(e + \omega_{\text{ref}})\right] - \frac{\partial\phi_p}{\partial e}\dot{e}. \tag{5.41}$$

Thus, the derivative of V_p is

$$\begin{aligned}
\dot{V}_p &= \sigma_p \dot{\sigma}_p \\
&= \sigma_p \left\{ \left(\frac{\partial \Psi_p}{\partial i_p} \right)^{-1} \left[v_p - R i_p - \frac{\partial \Psi_p}{\partial \theta_p} (e + \omega_{\text{ref}}) \right] - \frac{\partial \phi_p}{\partial e} \dot{e} \right\} \\
&= \left(\frac{\partial \Psi_p}{\partial i_p} \right)^{-1} v_p \sigma_p + \left(\frac{\partial \Psi_p}{\partial i_p} \right)^{-1} \left[-R i_p - \frac{\partial \Psi_p}{\partial \theta_p} (e + \omega_{\text{ref}}) \right] \sigma_p - \frac{\partial \phi_p}{\partial e} \dot{e} \sigma_p \\
&= \left(\frac{\partial \Psi_p}{\partial i_p} \right)^{-1} v_p \sigma_p + \alpha(e, i_p) \sigma_p - \beta_p(e, \underline{i}) \sigma_p \\
&\leq -V_{\text{dc}} \left(\frac{\partial \Psi_p}{\partial i_p} \right)^{-1} |\sigma_p| + \left[|\alpha(e, i_p)| + |\beta_p(e, \underline{i})| \right] |\sigma_p| \qquad (5.42)
\end{aligned}$$

where $\alpha(e, i_p) = \left(\frac{\partial \Psi_p}{\partial i_p} \right)^{-1} \left[-R i_p - \frac{\partial \Psi_p}{\partial \theta_p} (e + \omega_{\text{ref}}) \right]$ and $\beta_p(e, \underline{i}) = \frac{\partial \phi_p}{\partial e} \dot{e}$. The following facts provide the inequality relationships for the functions $\alpha(e, i_p)$ and $\beta_p(e, \underline{i})$ and the incremental inductance $\frac{\partial \Psi_p}{\partial i_p}$ to formulate the control gain V_{dc}.

Fact 1 *If α and β_p are continuous functions of (e, i_p) and $(e, \underline{i})$, respectively, and Ω_c is a compact set, then $\exists K_1, K_2 > 0$ such that $\forall (e, \underline{i}) \in \Omega_c$,*

$$|\alpha(e, i_p)| \leq K_1, \quad |\beta_p(e, \underline{i})| \leq K_2. \qquad (5.43)$$

Fact 2 *The incremental inductance is always positive:*

$$\left[\frac{\partial \Psi_p(\theta_p, i_p)}{\partial i_p} \right]^{-1} \geq K_3 > 0, \quad \forall \theta_p, i_p. \qquad (5.44)$$

Since α and β_p are smooth function of their arguments when $\theta_p \in \mathcal{I}$, from Facts 1 and 2, the derivative of the Lyapunov function candidate is bounded as follows,

$$\begin{aligned}
\dot{V}_p &\leq -K_3 V_{\text{dc}} |\sigma_p| + (K_1 + K_2) |\sigma_p| \\
&\leq -K_3 \left(V_{\text{dc}} - \frac{K_1 + K_2}{K_3} \right) |\sigma_p|. \qquad (5.45)
\end{aligned}$$

By choosing

$$V_{\text{dc}} > \frac{K_1 + K_2}{K_3} \qquad (5.46)$$

and defining

$$b = K_3 \left(V_{\rm dc} - \frac{K_1 + K_2}{K_3} \right), \tag{5.47}$$

we have

$$\dot{V}_p \leq -b|\sigma_p|. \tag{5.48}$$

The above inequality ensures that if the trajectory happens to be on the manifold $\sigma_p = 0$ at some time, it will be confined to that manifold for all future time because leaving the manifold requires $\dot{V}_p$ to be positive.

Moreover, the inequality (5.48) ensures that trajectories starting off the manifold $\sigma_p = 0$ reach it in finite time. This can be shown by the use of the comparison lemma: Since $i_p(t)$ and $i_{{\rm ref},p}(t)$ are smooth function of t, when $s_p \neq 0$, the signal $|s_p(t)| = |\sigma_p(e(t), i_p(t))|$ is differentiable with respect to t. That is, for $s_p \neq 0$, $D^+|s_p| = \frac{d|s_p|}{dt}$ (D^+ denotes the upper right-hand derivative defined in [19]). Therefore, when $s_p \neq 0$, using the fact that $|s_p| = |\sigma_p| = \sqrt{2V_p}$ from (5.39), we have the upper right-hand derivative of $|s_p|$,

$$\begin{aligned} D^+|s_p| &= \frac{\sqrt{2}}{2} V_p^{-\frac{1}{2}} \dot{V}_p \\ &= \frac{\dot{V}_p}{\sqrt{2V_p}} \\ &\leq \frac{-b|s_p|}{|s_p|} \qquad \text{from (5.48)} \\ &\leq -b. \end{aligned} \tag{5.49}$$

Let $y(t)$ be the solution of the differential equation

$$\dot{y} = -b, \quad y(0) = |s_p(0)|.$$

Hence,

$$y(t) = |s_p(0)| - bt.$$

Then, by the comparison lemma, the solution $|s_p(t)|$ is defined for all $t \geq 0$ and satisfies

$$\begin{aligned} |s_p(t)| &\leq y_p(t) \\ &\leq |s_p(0)| - bt, \quad \forall t \geq 0. \end{aligned} \tag{5.50}$$

The above inequality (5.50) shows that $|s_p(t)|$ starting from $|s_p(0)| \neq 0$ is always below the curve $y(t) = |s_p(0)| - bt$. Therefore, because $y(t)$ reaches zero at $t = \frac{|s_p(0)|}{b}$, $|s_p(t)|$ also reaches zero in finite time, that is, trajectories starting from $s_p(0) \neq 0$ reach the sliding manifold in finite time.

Now, let $\big(e(0), \underline{i}(0)\big) \in \Omega_c$ and consider an upper bound on the initial condition $|s_p(0)|$:

$$S \triangleq \max_{\big(e(0),\underline{i}(0)\big)\in\Omega_c} \big(i_p(0) - \phi_p(e(0))\big) .$$

Notice that S is finite because $i_p - \phi_p(e)$ is a smooth function of its arguments. Using this bound and the assumption that $\big(e(t), \underline{i}(t)\big) \in \Omega_c$ for $t \geq 0$, we can find a uniform upper bound to the reaching time as $t_R = \frac{S}{b}$. In other words, for all $\big(e(t), \underline{i}(t)\big) \in \Omega_c$, $s_p(t) = 0$ for all $t \geq t_R$. The proof of Theorem 2 is concluded by choosing $V_{\rm dc}$ so that $b \geq \frac{S}{\Delta t}$ (thus showing that $t_R \leq \Delta t$). □

Stability of Tracking Error

The proof for Theorem 2 has shown that, if the assumption on Ω_c holds, then for any $\Delta t > 0$, there exists $V_{\rm dc} > 0$ such that $s_p(t) \to 0$ in time less than Δt. Also, because the reference current signal is smooth for $\theta_p \in \mathcal{I}$, the condition $s_p = 0$ is maintained for subsequent time during the commutation interval. However, because $i_{\rm ref,p} = \phi(\theta_p, e)$ is a piecewise continuous function of $\theta_p(t)$, the condition $s_p = 0$ cannot be maintained for more than one commutation interval. Here, we will extend our stability result of sliding manifold for one commutation phase to all phases and explain why the stability of speed error e can be still guaranteed under certain conditions.

In the design of a sliding manifold, we have selected discontinuous feedback control (5.17) in acceleration and (5.18) in braking. The control laws are discontinuous in order to prevent from producing opposing torques. Since the commutation intervals of adjacent phases always overlap, by exciting the phases whose phase angles are within commutation intervals, we can guarantee a continuous production of the required minimum torque. Thus, if $i_p = \phi(\theta_p, e)$, the stability of $e = 0$ is guaranteed.

Now, we need to control the actual current i_p close enough to the waveform of

$i_{\text{ref,p}} = \phi(\theta_p, e)$ so that a continuous production of the required minimum torque is still guaranteed. That is, at least one phase p^* ($\theta_{p^*} \in \mathcal{I}$) maintains $i_{p^*} = i_{\text{ref},p^*}$ at any time. More precisely, every i_p starting from zero reaches $i_{\text{ref},p}$ before the previous phase ends its phase excitation. Figure 5.9 shows i_p and $i_{\text{ref},p}$ in two adjacent phases. As seen in the proof of Theorem 2, the control gain V_{dc} can be chosen so that the

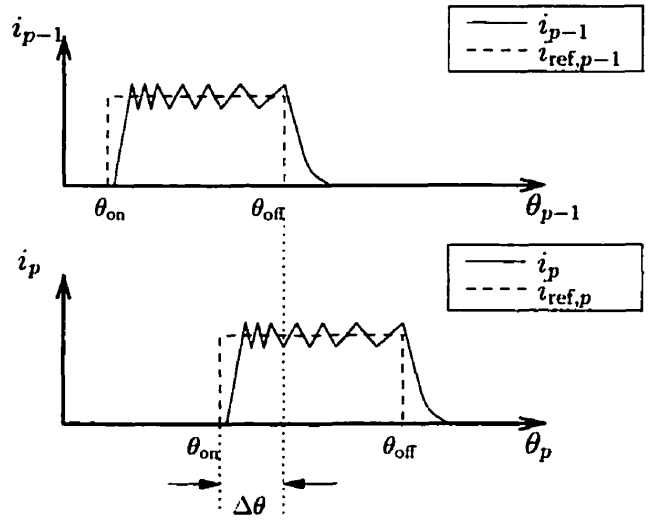

Figure 5.9: Phase current and reference current signal in adjacent phases (Overlapping of adjacent commutation phases)

reaching time t_R is less than Δt. In order to guarantee the convergence of i_p to $i_{\text{ref},p}$ within the overlapping period of the adjacent phases, it is sufficient to choose Δt to be the duration of overlapping between adjacent commutation phases. That is, at some rotor speed ω,

$$\Delta t = \frac{\Delta\theta}{\omega}, \tag{5.51}$$

where $\Delta\theta$ is the overlapping commutation intervals of adjacent phases as shown in Figure 5.9. As shown earlier, there exists a lower bound of Δt given as

$$\Delta t \geq \frac{\Delta\theta}{|\omega_{\text{ref}}| + |e|}. \tag{5.52}$$

Since the overlapping time Δt has a lower bound, choose $t_R = \Delta t$. By Theorem 2, we conclude that, if the assumption on Ω_c holds, then with a sufficiently large V_{dc}, every

phase current reaches its corresponding reference current signal before the previous phase ends its phase excitation. Hence, a continuous production of the required minimum torque is guaranteed, and $e = 0$ is asymptotically stable. We stress once again that the assumption that $(e(t), \underline{i}(t)) \in \Omega_c$ for $t \geq 0$ is essential to guarantee the validity of the results of this section. The stability of speed error is demonstrated in the simulations.

Note, as a concluding remarks, that V_{dc} guaranteeing that $e \to 0$ may be too large to be implemented. Underline that, in practice, a much smaller V_{dc} is needed. Our analysis is conservative and is used only to show that there exists V_{dc}, not to give indications on how large V_{dc} should be.

5.2.3 Overall Controller

The overall speed tracking controller designed with SMC is as follows:

1) The reference current controller:

Case I : $(e < 0, \omega_{ref} > 0)$

$$i_{ref,p} = \phi(\theta_p, e) = \begin{cases} h^{-1}(B\omega_{ref} - C_1 e), & \text{for } \theta_p \in \mathcal{I} \\ 0, & \text{otherwise,} \end{cases} \tag{5.53}$$

Case II : $(e > 0, \omega_{ref} > 0)$

$$i_{ref,p} = \phi(\theta_p, e) = \begin{cases} h^{-1}(C_2 e), & \text{for } \theta_p \in \mathcal{I}' \\ 0, & \text{otherwise,} \end{cases} \tag{5.54}$$

where $h^{-1}(\cdot) = 11.4416\left[-0.0135 + \sqrt{0.00018225 + 0.1748(\cdot)}\right]$; $C_1 > -B$ and $C_2 > 0$.

2) The position of state i_p with respect to the sliding manifold:

$$s_p = i_p - i_{ref,p}, \quad p = 1, \ldots, 4, \tag{5.55}$$

3) The current chopping controller:

$$v_p = -V_{dc}\text{sgn}(s_p), \quad p = 1, \ldots, 4, \tag{5.56}$$

where $V_{dc} = 400$ Volts.

5.3 Simulation Results

In this section, the simulation results for the sliding mode control algorithm are presented and compared with the simulation results from the previous chapter. The SMC algorithm was simulated in Matlab/Simulink with the same state model used in the simulations for the traditional control algorithm. Figure 5.10 shows the Simulink block diagram with SMC for the low speed operation. The plant blocks are identical

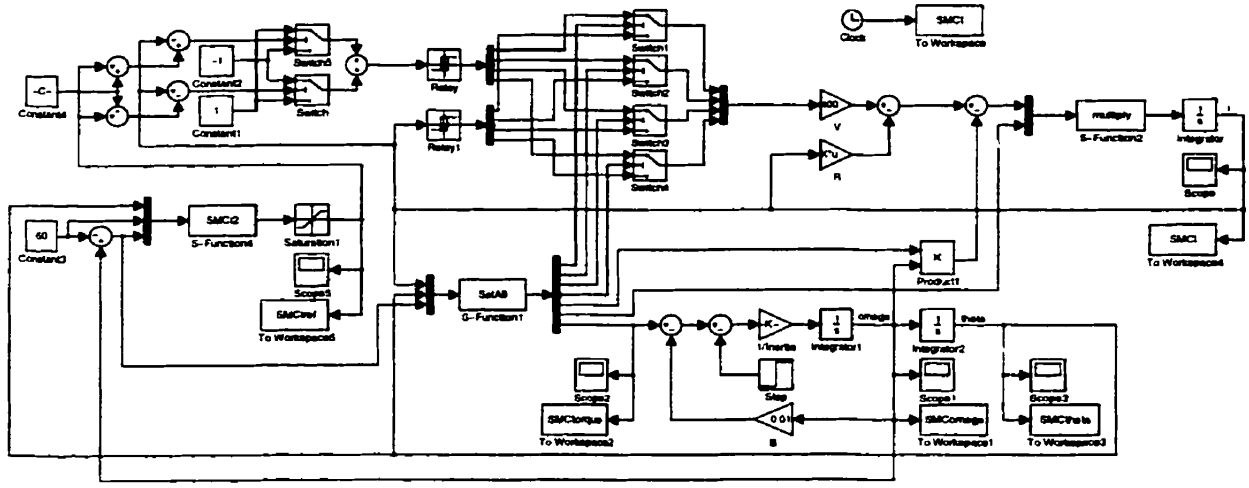

Figure 5.10: Simulink block diagram for the SMC algorithm

to that in Figure 4.9. As shown in Figure 5.8, the measured variable θ and the states ω and $\underline{i}$ are fed back to the controllers. The overall control structure of SMC algorithm is similar to that of the traditional controller because SMC utilizes the same switching circuit typical of electrical hardware for SR machines. The control blocks consist of three parts, i.e., a control block for the function ϕ, a hysteresis controller, and a commutation controller. The S-function block 'SMCi2' takes θ, ω_{ref}, and the speed error $e = \omega - \omega_{\text{ref}}$ as inputs and calculates the phase angles θ_p and the reference current signal $i_{\text{ref},p} = \phi(\theta_p, e)$. The current chopping controller (5.56) is approximated by using a hysteresis controller to limit the switching frequency of current chopping. The hysteresis bandwidth is fixed to ± 2 Amps as in the traditional control simulations. The commutation angles are chosen to be the same as used in the traditional control simulations, and commutation signals are produced by the S-function block 'SatAll'.

The S-function block also calculates the incremental inductance, back emf coefficient, and instantaneous torque for each phase. The parameters for simulations are the same as used in the traditional control simulations and are given in Table 4.3.

5.3.1 Resulting Waveforms

The designed SMC algorithm was tested with different values of C_1 and C_2. We first present the resulting waveforms of incremental inductance, voltage signal, flux-linkage, and phase current as shown for the traditional control simulations. Figure 5.11 shows the waveforms obtained from one of the simulations under a load disturbance torque in acceleration. As one can see, the waveforms are similar to those in Figure 4.10. The same explanation can be said for the waveforms obtained from the SMC simulation since the relationships among the waveforms are the same in the two control methods.

The difference between the two control algorithms is the calculation of the reference current. The function ϕ was designed to guarantee that the speed error approaches zero asymptotically when the state trajectory is confined to the sliding manifold. Since ϕ is discontinuous, it is impossible to maintain the state trajectory on the manifold. In the discussion on this issue, we stated that the speed error can be still stabilized as long as the current dynamics are fast and the overlapping of adjacent phase torques is guaranteed. Here, we illustrate that the phase current stays close to the reference current, and therefore a continuous production of required minimum torque is guaranteed. Figure 5.12 shows the convergence of phase current to reference current before the turn-off of the previous phase current. As one can see, the current dynamics are very fast at the beginning of each commutation period, and each phase current reaches its reference current in finite time well prior to the turn-off of the previous phase commutation. Thus, a continuous torque production is guaranteed. (Note that there exists a large chattering in the phase current around the reference current signal. This is due to the use of a hysteresis controller with bandwidth of ± 2 Amps in the chopping circuit. The smaller the hysteresis band, the smaller the chattering is. With an infinitesimally small hysteresis bandwidth, the phase current

(a) Inductance

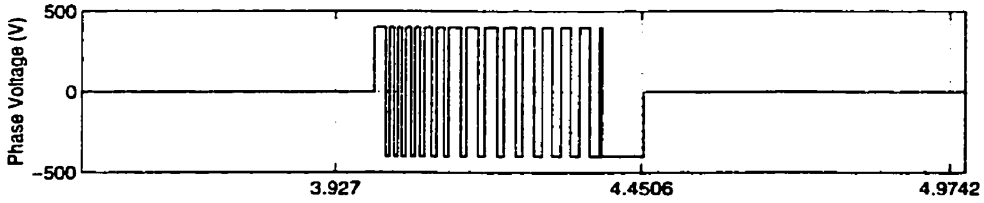

(b) Phase Voltage

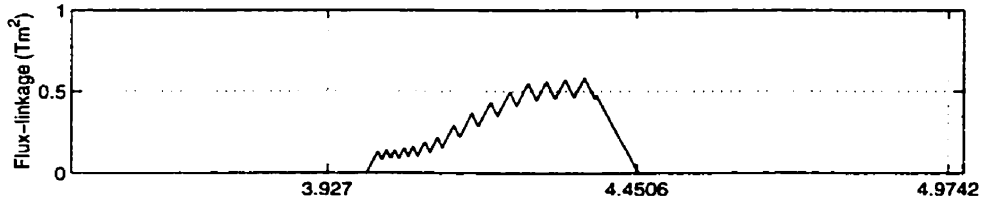

(c) Flux-linkage

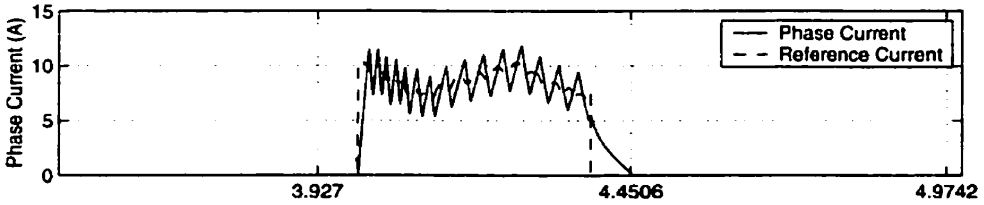

(d) Phase Current

Figure 5.11: Waveforms with respect to rotor angle θ for SMC current chopping mode in acceleration. A: aligned position, U: unaligned position.

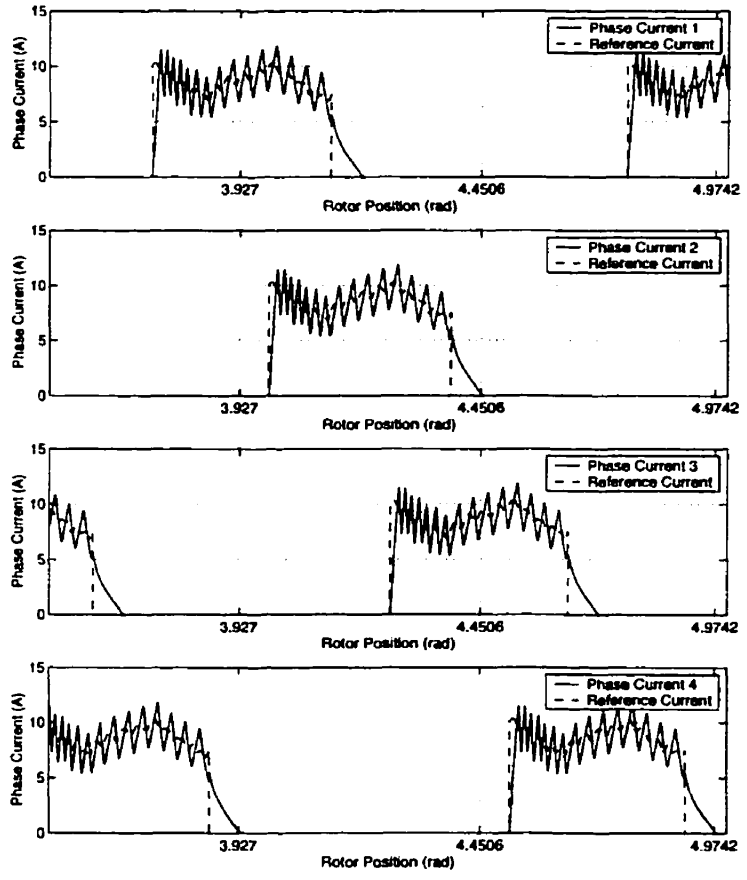

Figure 5.12: Phase current waveforms in four phases

coincides with the reference current signal.) The speed response and the continuous torque production in SMC during the acceleration period are shown in Figure 5.13. Notice that the speed response in SMC also oscillates due to the torque ripples. The oscillation of the speed response reflects in the reference current signal produced by the feedback of the rotor speed.

5.3.2 Tuning Function ϕ

The constants C_1 and C_2 in the function ϕ are the control gains that determine the rate of convergence of speed error to the origin when the state trajectory is confined to the sliding manifold. The SMC algorithm with various choices of C_1

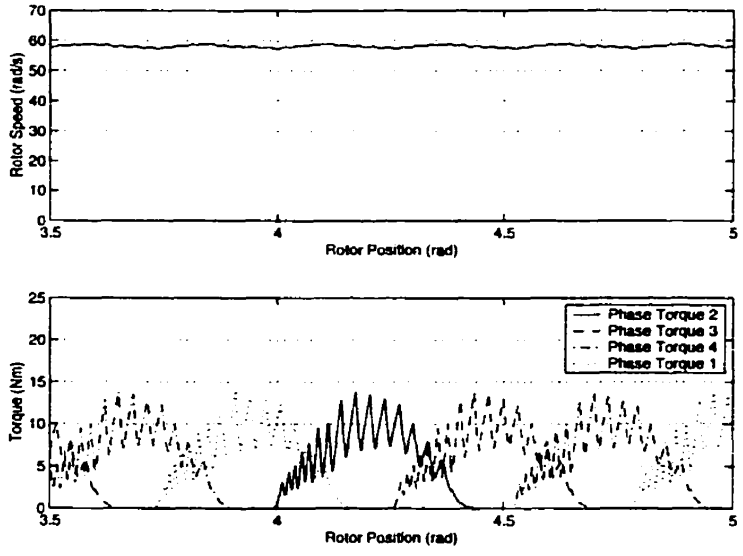

Figure 5.13: Speed response and continuous torque production during acceleration

and C_2 was tested with the nominal plant with no load disturbance. The machine inertia is set to $J = 0.001 kgm^2$. The initial conditions for the state variables are $\theta(0) = \theta_1(0) = 0$, $\omega(0) = 0$, and $i_p(0) = 0$ $(p = 1, \ldots, 4)$. Since C_1 and C_2 could be chosen independently for acceleration and braking, they were selected to be equal for simplicity. We name the constants as $Kc = C_1 = C_2$. From the proof of Theorem 2, $e = 0$ is asymptotically stable on the sliding manifold as long as $C_1 > -B$ in acceleration and $C_2 > 0$ in braking. First, small K_c was tested. Figure 5.14 shows the step response of the SR machine for the reference speed $\omega_{\text{ref}} = 60 rad/s$. Here, K_c was varied from 0.5 to 0. As one can see, the rotor speed approaches the reference speed even when K_c is very small. In low speed operation, phase current dynamics are fast so that the excitations of adjacent phase windings always overlap. Figure 5.15 shows the speed response for $K_c = 0$ and the overlapping of phase commutation during the transient period.

Next, we show the performance of SMC algorithm with larger K_c. Figure 5.16 shows the step response with K_c larger than 0.5. Here, K_c was varied from 0.5 to 6.0. As seen in the previous chapter, a larger gain causes overshoots in speed response for the price of reducing the rise time. Figure 5.17 shows the reference current signal and

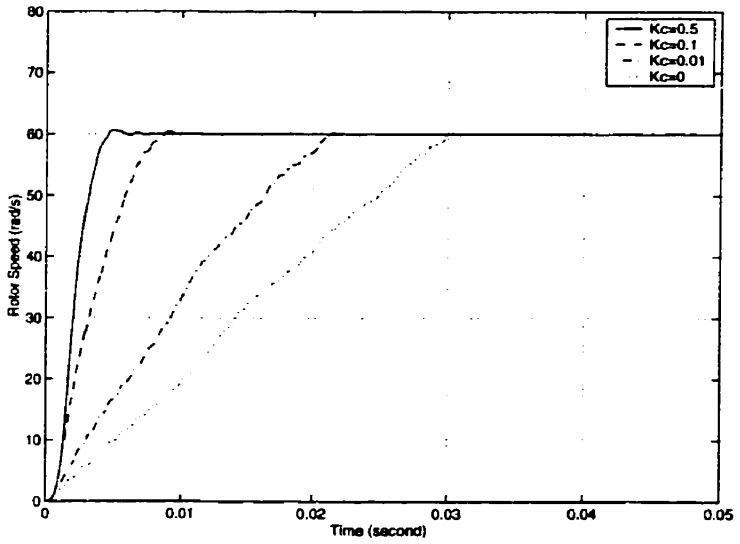

Figure 5.14: Speed response for SMC with small K_c

the actual current in Phase 2 for $K_c = 5$. The figure shows that the phase current increases while the speed error is negative and decreases while positive. It is due to the switching action of the function ϕ with respect to the sign of speed error. As explained in the previous chapter, the overshoots are caused by the existence of nonzero phase current when the rotor speed first reaches the reference speed of $\omega_{\text{ref}} = 60 rad/s$. The stored energy in the circuit further increases the rotor speed until other phases brake the rotation.

A gain K_c was selected for the optimal performance of SMC where the speed response has fast dynamics with the least overshoot. Figure 5.18 shows the speed response along with the phase current and the reference current for $K_c = 1.5$. Unlike the reference current signal produced for $K_c = 5$, the reference current signal produced for $K_c = 1.5$ is reduced as the phase current comes down. Because the dynamics of the reference current signal and the actual phase current synchronize, there is no extra current causing overshoots in the speed response. Once the speed error e reaches the vicinity of zero, the reference current signal remains low as it depends on e.

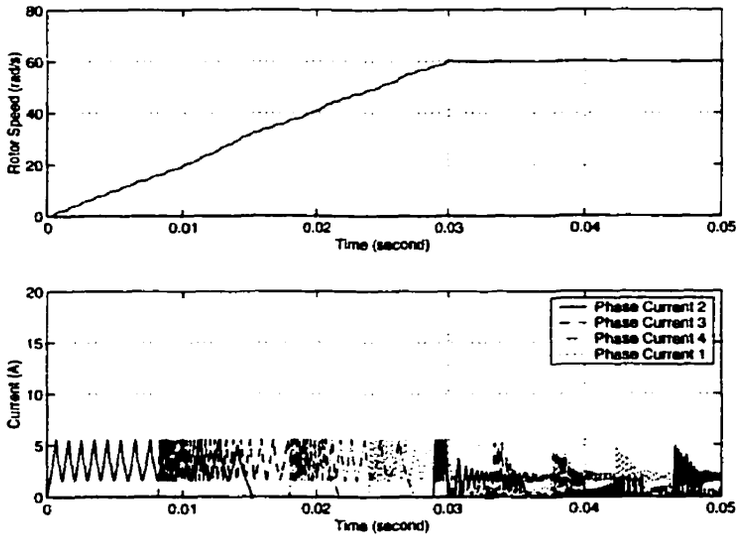

Figure 5.15: Speed response, phase current, and reference current signal for SMC with $K_c = 0$

5.3.3 Performance under Various Operating Conditions

The SMC algorithm was tested under different operating conditions. We will make comparisons against the simulation results from the traditional control algorithm. Figure 5.19 shows the speed responses of the traditional control and SMC algorithms for the reference speeds $\omega_{\text{ref}} = 30$, 60, and $90 rad/s$. The settling times of two controllers at each operating speed are similar to each other. However, the speed response of SMC for a smaller ω_{ref} has slight overshoots. The slight difference shown for the lower ω_{ref} is due to the fact that the reference current signal of the traditional controller is partially based on the integrator which builds up the control output signal over time while the reference current signal of in SMC has an immediate influence from the speed error. Both control algorithms slightly change their performance at different operating speeds.

Next, the SMC algorithm was tested with the moment of inertia $J = 0.01 kgm^2$. Figure 5.20 shows the speed response for two control algorithms and the current plot for the SMC. Like the results for the traditional control, the speed response of the SMC is also slowed down by the larger inertia. The figure shows the responses of two control algorithms with similar settling time. The current plot shows that Phase 2 is

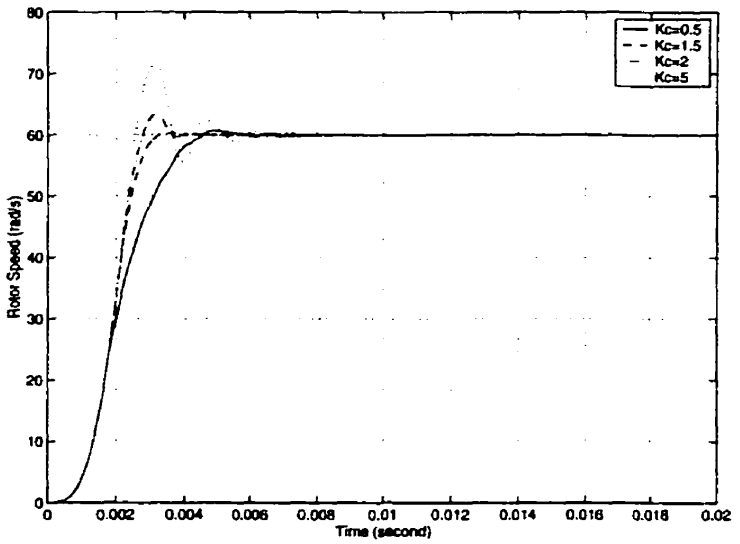

Figure 5.16: Speed response for SMC with various K_c. Solid: $Kc = 0.5$, Dashed: $Kc = 1.5$, Dot-dashed: $Kc = 2.0$, and Dotted: $Kc = 5.0$

energized for the entire commutation period because the speed error has not reached zero unlike the simulation result with a smaller moment of inertia.

Finally, the SMC was tested under load disturbance torque. Figure 5.21 shows the speed responses for two control algorithms with the addition of load torque $T_l = 10Nm$ at $t = 0.02s$ for the three different operating speeds. The figure shows that the SMC algorithm recovers quickly from the addition of load disturbance. However, it does not completely reject the disturbance. As one can see, there is constant oscillation of steady-state error in the speed response for SMC while the speed error for the traditional control gradually recovers from the addition of load disturbance. The reason for the existence of steady-state error in SMC is because the matching condition is not satisfied in the system. The disturbance enters the mechanical subsystem while the actual system input is the voltage signal which enters the system in the electrical subsystem. Nevertheless, the system is stabilized with a bounded steady-state error because the total instantaneous torque produced by the feedback control matches with the load disturbance torque. Figure 5.22 shows the speed response under disturbance for SMC and its current plot for $\omega_{\text{ref}} = 60rad/s$. The speed error increases from the zero steady-state error when the disturbance is added. The reference current signal

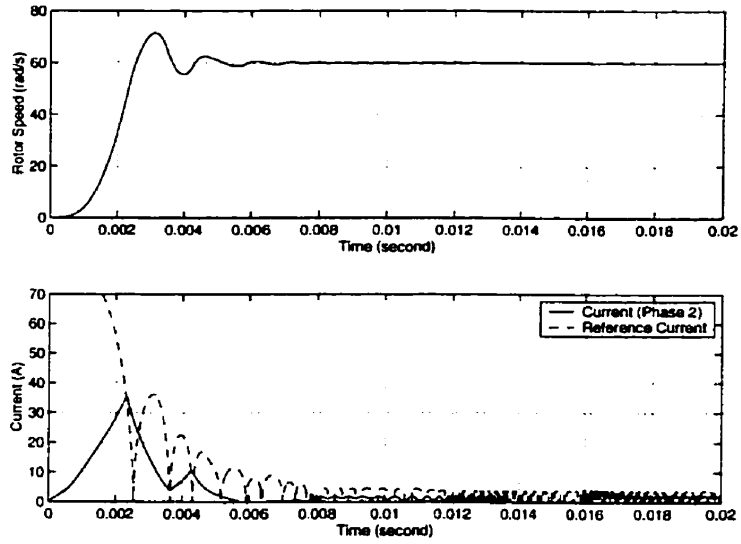

Figure 5.17: Speed response, phase current (Phase 2), and reference current signal with $K_c = 5.0$

as well as the phase current increase by the feedback control and stay at the level where the total torque matches with the disturbance torque.

In order to reject the disturbance completely, an additional term needs to be introduced in the design of the function ϕ. Here, we provide a brief explanation of how a robust performance can be achieved with SMC. From the proof of Theorem 1, recall the inequality (5.23),

$$\dot{e} \geq \frac{1}{J}\big[h(i_{p^*}) - B\omega_{\text{ref}} - Be\big].$$

When the load disturbance torque T_l is added to the system, the inequality becomes

$$\dot{e} \geq \frac{1}{J}\big[h(i_{p^*}) - B\omega_{\text{ref}} - Be - T_l\big]. \tag{5.57}$$

Let us introduce an additional term $q(e)$ in the lower bound function $h(i_{p^*})$ such that for some $t_1 \geq 0$,

$$q\big(e(t)\big) \geq T_l, \quad \forall t \geq t_1.$$

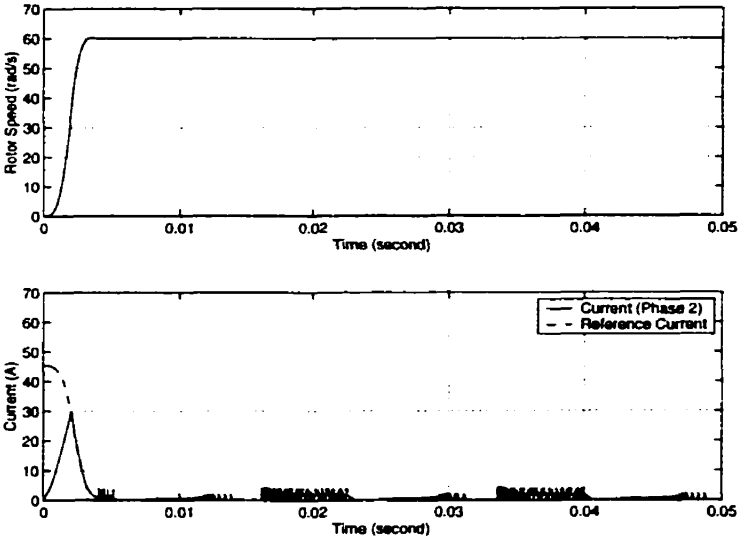

Figure 5.18: Speed response, phase current (Phase 2), and reference current for SMC with $K_c = 1.5$ (the optimal performance)

Then, substituting $i_{p^*} = h^{-1}\big(B\omega_{\text{ref}} - C_1 e + q(e)\big)$ into (5.57), we have

$$\begin{aligned} \dot{e} &\geq \frac{1}{J}\big[B\omega_{\text{ref}} - C_1 e + q(e) - B\omega_{\text{ref}} - Be - T_l\big] \\ &\geq \frac{1}{J}\big[-C_1 e + q(e) - Be - T_l\big] \\ &\geq -\frac{1}{J}(C_1 + B)e \\ &> 0. \end{aligned} \tag{5.58}$$

This robust control design may be suggested for a part of the future work on this research.

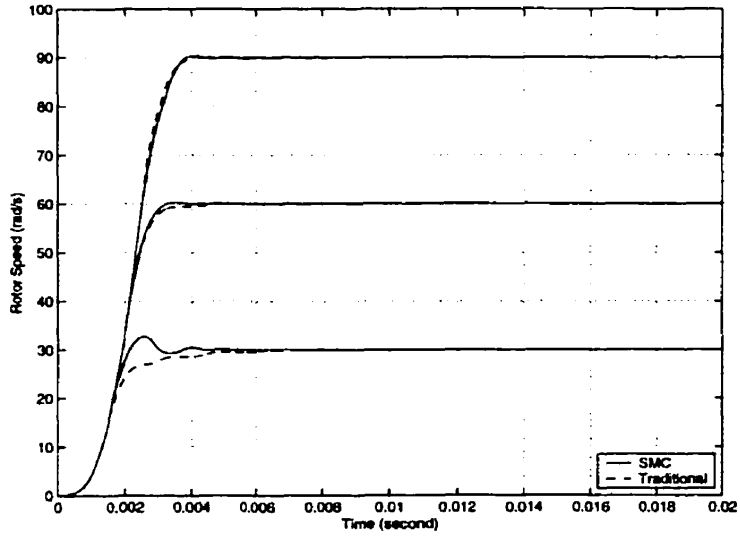

Figure 5.19: Comparison of SMC with the traditional controller: speed responses for various reference speeds $\omega_{\text{ref}} = 30$, 60, and $90 rad/s$. Solid: SMC, Dashed: traditional

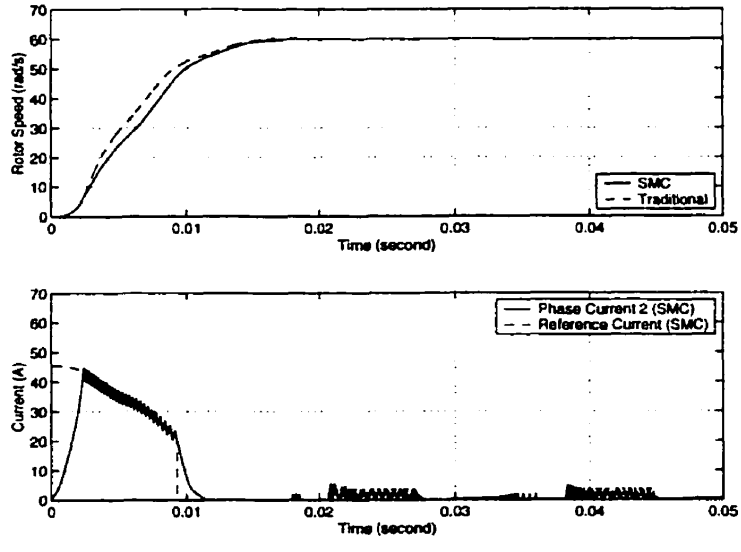

Figure 5.20: Comparison of SMC with the traditional controller: speed response and current signals for larger moment of inertia $J = 0.01 kgm^2$ (Current signals are shown only for SMC.)

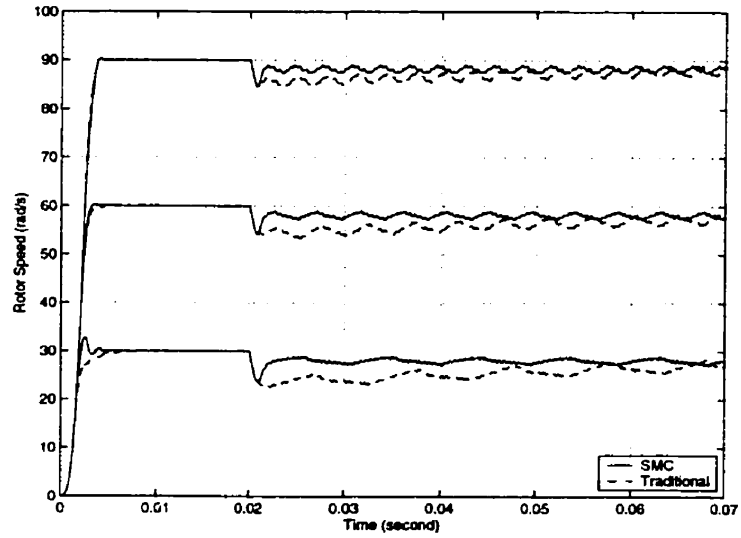

Figure 5.21: Comparison of SMC with the traditional controller: speed responses with load disturbance $T_l = 10Nm$ for various reference speeds

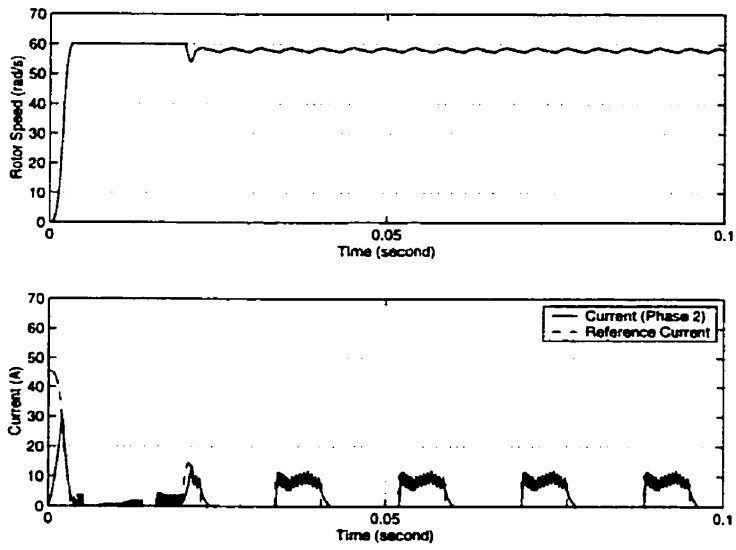

Figure 5.22: Speed response, phase current (Phase 2), and reference current signal for SMC with load disturbance $T_l = 10Nm$

Chapter 6

Conclusion

This thesis studied the application of a nonlinear control design method to an 8/6 regular switched reluctance machine. The mechanical and electrical subsystems were first modeled, and the principle of torque production in SR machines was illustrated in detail. The model of the magnetization characteristics for a 4kW SR machine including saturation was taken from [4], and a set of self-contained state equations was developed. Next the conventional control scheme for two operating speeds was described, and a commutation strategy using a fixed set of turn-on and turn-off angles for different operating speeds was explained. The traditional controller using PI control for the determination of reference current signals was designed for low speed operation by trial and error in computer simulations.

Sliding mode control was employed for guaranteeing the stability in tracking control of SR machines. Among other possible nonlinear control approaches, SMC was chosen for the ease of implementation in SR machines, which relies on a switching control circuit. A sliding mode controller was designed using nonlinear control theoretic design tools with the use of minimum information on saturation characteristics of the machine. The designed controller was tested in simulations, and the results were compared to the traditional controller.

6.1 Contributions and Limitations

In this section, we summarize the contributions of this thesis focusing on the benefits and the limitations of our study.

Our literature overview in Chapter 1 highlighted the need to explore design methods leading to a simpler controller guaranteeing the stability of SR machines. Using the nonlinear sliding mode control design method and exploiting the characteristics of torque production in SR machines, we have come up with a simple nonlinear controller that guarantees the stability of speed tracking control in SR machines. In this thesis, we have made the following contributions:

1. The stability of speed tracking error is guaranteed by the theoretical approach using sliding mode control.

2. The proposed design scheme requires minimal information on saturation characteristics of the machine.

3. The designed controller requires simple computations in real time, and hence the implementation in practice does not require expensive computation processors.

The theoretical results concerning the stability of the speed tracking error have been confirmed by the simulation results.

During the course of our study, we have faced some limitations. As mentioned earlier, the proof of Theorem 2 heavily relies on a strong assumption which is difficult to verify *a priori*. Although the simulation results demonstrate that the assumption is indeed intuitively acceptable, this is a gap in our theoretical proof.

From the observation of the simulation results and the comparison against the traditional controller, we concluded that the sliding mode controller we designed has similar characteristics to the conventional controller in dynamic response. This is due to the fact that the control structure of the sliding mode controller is identical to that of the traditional controller. The suitability of SMC design method to the structure of the traditional controller limits some of the capabilities of SMC, particularly robustness to the load disturbances. In the presence of load torque, the simulation re-

sults show a faster recovery of SMC in transient, but the controller cannot completely reject the disturbance, in that there exists a steady-state error.

6.2 Future Directions

Among many research topics in the study of SR machines, there are a few closely related research directions in which the work of this thesis can be extended. Since the validity of simulation results is based on the accuracy of the system model, the performance of the controllers may differ in a real system. Hence, the first possible study is to implement the controller in a real SR machine and investigate the limitations of the controller in a real system.

One of the disadvantages of the sliding mode controller designed in this research is the limitation in robustness to load disturbances. In speed tracking control, there exists a steady-state error in the presence of load torque. It is desirable to improve the robustness of the controller to surpass the performance of the traditional controller. As explained at the end of Chapter 5, it is possible to reject the load disturbances by adding another term in the inverse of the lower bound function h. Intuitively, it is reasonable to use an integrator to increase the reference current signal so that higher torque is produced to reduce the steady-state error in the presence of a load disturbance.

As seen in the simulation results, the speed response in the presence of load torque yields torque-ripple coming from the overlapping of the phase torques. It will be challenging but also beneficial to study whether the torque-ripple can be reduced with a minimum cost of utilizing the information on saturation characteristics of the SR machine. The possible study on torque-ripple minimization may include the employment of other control techniques which do not require full knowledge of a system model, e.g., self-tuning control, fuzzy logic control, and neural networks.

Bibliography

[1] R. C. Becerra, M. Ehsani, and T. J. E. Miller. Commutation of SR motors. *IEEE Trans. Power Electronics*, 8(3):257–263, 1993.

[2] G. S. Buja, R. Menis, and M. I. Valla. Variable structure control of an SRM drive. *IEEE Trans. Industrial Electronics*, 40(1):56–63, 1993.

[3] G. S. Buja and M. I. Valla. Control characteristics of the SRM drives. Part II: Operation in the saturated region. *IEEE Trans. Industrial Electronics*, 41(3):316–325, 1994.

[4] W. M. Chan and W. F. Weldon. Development of a simple nonlinear switched reluctance motor model using measured flux linkage data and curve fit. In *IEEE Industry Applications Conf.*, volume 1, pages 318–325, 1997.

[5] C. P. Cho and D. R. Crecelius. Vehicle alternator/generator trends toward next millennium. In *IEEE Proc. Vehicle Electronics Conf.*, volume 1, pages 433–438, 1999.

[6] C. M. Close and D. K. Frederick. *Modeling and Analysis of Dynamic Systems, 2nd Ed.* Wiley, New York, 1995.

[7] R. A. DeCarlo, S. H. Zak, and S. V. Drakunov. Variable structure, sliding-mode controller design. In W. S. Levine, editor, *The Control Handbook*, pages 941–951. CRC Press, Boca Raton, FL, 1996.

[8] M. T. DiRenzo, M. K. Masten, and C. P. Cole. Switched reluctance motor control techniques. In *Proc. American Control Conf.*, volume 1, pages 272–277, 1997.

[9] M. Ehsani. Switched reluctance motor drives – recent advances. *Sadhana-Academy Proc. Engineering Sciences*, 22(6):821–836, 1997.

[10] F. Filicori, C. G. LoBianco, and A. Tonielli. Modeling and control strategies for a variable reluctance direct-drive motor. *IEEE Trans. Industrial Electronics*, 40(1):105–115, 1993.

[11] A. F. Filippov. *Differential Equations with Discontinuous Righthand Sides.* Kluwer Academic, Dordrecht, The Netherlands, 1988.

[12] G. F. Franklin, J. D. Powell, and A. Emami-Naeini. *Feedback Control of Dynamic Systems, 3rd Ed.* Addison-Wesley, Reading, MA, 1995.

[13] J. J. Gribble, P. C. Kjaer, C. Cossar, and T. J. E. Miller. Optimal commutation angles for current controlled switched reluctance motors. In *Int. Conf. on Power Electronics and Variable Speed Drives*, pages 87–92, 1996.

[14] J. J. Gribble, P. C. Kjaer, and T. J. E. Miller. Optimal commutation in average torque control of switched reluctance motors. *IEE Proc. Electric Power Applications*, 146(1):2–10, 1999.

[15] W. K. Ho, S. K. Panda, K. W. Lim, and F. S. Huang. Gain-scheduling control of the switched reluctance motor. *Control Engineering Practice*, 6(2):181–189, 1998.

[16] I. Husain and M. Ehsani. Torque ripple minimization in switched reluctance motor drives by PWM current control. *IEEE Trans. Power Electronics*, 11(1):83–88, 1996.

[17] M. Ilic'-Spong, R. Marino, S. M. Peresada, and D. G. Taylor. Feedback linearizing control of switched reluctance motors. *IEEE Trans. Automatic Control*, 32(5):371–379, 1987.

[18] G. John and A. R. Eastham. Speed control of switched reluctance motor using sliding mode control strategy. In *Industrial Applications Conf.*, volume 1, pages 263–270, 1995.

[19] H. K. Khalil. *Nonlinear Systems, 2nd Ed.* Prentice-Hall, Upper Saddle River, NJ, 1996.

[20] J. A. Kline. Opportunities for switched reluctance motor-drives. In *Industrial Technical Conf. on Pulp and Paper*, pages 42–47, 1999.

[21] C. G. LoBianco, F. Filicori, and A. Tonielli. A prototype controller for variable reluctance motors. *IEEE Trans. Industrial Electronics*, 43(1):207–216, 1996.

[22] T. J. E. Miller. *Switched Reluctance Motors and their Control.* Magna Physics Publishing and Oxford University Press, Hillsboro, OH and New York, 1993.

[23] N. J. Nagel and R. D. Lorenz. Modeling of a saturated switched reluctance motor using an operating point analysis and the unsaturated torque equation. *IEEE Trans. Industry Applications*, 36(3):714–722, 2000.

[24] K. S. Narendra and K. Parthasarathy. Identification and control of dynamical systems using neural networks. *IEEE Trans. Neural Networks*, 1(1):4–27, 1990.

[25] S. K. Panda and P. K. Dash. Application of nonlinear control to switched reluctance motors: A feedback linearisation approach. *IEE Proc. Electric Power Applications*, 143(5):371–379, 1996.

[26] W. F. Ray. Switched reluctance drives. In *IEE Colloq. on Energy Efficient Environmentally Friendly Drive Systems Principle*, pages 3/1–3/9, 1996.

[27] C. Rossi and A. Tonielli. Feedback linearizing and sliding mode control of a variable-reluctance motor. *Int. J. Control*, 60(4):543–568, 1994.

[28] K. Russa, I. Husain, and M. E. Elbuluk. Torque-ripple minimization in switched reluctance machines over a wide speed range. *IEEE Trans. Industry Applications*, 34(5):1105–1112, 1998.

[29] K. Russa, I. Husain, and M. E. Elbuluk. A self-tuning controller for switched reluctance motors. *IEEE Trans. Power Electronics*, 15(3):545–552, 2000.

[30] V. K. Sharma, S. S. Murthy, and B. Singh. An improved method for the determination of saturation characteristics of switched reluctance motors. *IEEE Trans. Instrumentation and Measurement*, 48(5):995–1000, 1999.

[31] P. Tandon, V. Rajarathnam, and M. Ehsani. Self-tuning control of a switched-reluctance motor drive with shaft position sensor. *IEEE Trans. Industry Applications*, 33(4):1002–1010, 1997.

[32] V. I. Utkin. *Sliding Modes in Control Optimization.* Springer-Verlag, New York, 1992.

[33] K. Venkataratnam, T. K. Bhattacharya, and M. Sengupta. Theory, performance prediction, and indirect sensing of rotor position of a switched reluctance motor under saturation. *IEE Proc. Electric Power Applications*, 146(6):667–677, 1999.

[34] V. Vujicic and N. Vukosavic. A simple nonlinear model of the switched reluctance motor. *IEEE Trans. Energy Conversion*, 15(4):395–400, 2000.

[35] H. Yang, S. K. Panda, and Y. C. Liang. Performance comparison of sliding mode control with PI control for four-quadrant operation of switched reluctance motors. In *Proc. Power Electronics, Drives, and Energy Sytems for Industrial Growth Conf.*, volume 1, pages 381–387, 1995.

[36] H. Yang, S. K. Panda, and Y. C. Liang. Performance comparison of feedback linearization control with PI control for four-quadrant operation of switched reluctance motors. In *Proc. Applied Power Electronics Conf. and Expo.*, volume 2, pages 956–962, 1996.